A Novel Processing Route for the Manufacture of Mg with Controlled Cellular Structure

By

Ingólfur Kolbeinsson

A thesis submitted in partial fulfilment of the requirements for the

Degree of Master of Engineering

University of Canterbury
March 2009

Contents

List of figures

List of Tables

Abstract

Cellular metals are a relatively new class of engineering materials that can be fabricated with either a random or controlled cellular structure. A controlled cellular structure allows the precise control of the pore geometry and hence subsequent material properties that can be important for some applications such as orthopathic implants. Recently the interest in using magnesium (Mg) as a biodegradable implant in the body has been growing rapidly. However, current methods for fabricating cellular magnesium typically results in a random arrangement of the cellular structure.

A novel processing method is developed for the preparation of cellular metals with controlled open-cellular architectures. In particular, this process has been developed for magnesium due to the difficulties associated with powder processing. The fabrication routine utilises a multistage inverse templating technique implemented with assistance of a rapid prototyping (RP) technique. Rapid prototyped polymer performs of desired architectures were infiltrated using a specially designed slurry of NaCl. Removal of the polymer resulted in an accurate negative NaCl template that could be infiltrated with liquid metal using low pressure die casting. Subsequently, the template material is removed, resulting in a controlled cellular structure within Mg.

Prior to metal infiltration, the compressive modulus, strength, grain growth and microstructure of the NaCl structure with and without sintering was examined using compression testing and electron backscattered diffraction (EBSD). For the EBSD analyses a new sample preparation technique for the micro porous samples had to be developed for use in the scanning electron microscopy (SEM). The NaCl and the cellular metal were evaluated using SEM and micro-computed tomography (μ-CT). Furthermore, the relationship between the original CAD model and the final NaCl pore morphology was investigated were the surfaces of the RP scaffold and the NaCl template were analysed and compared to the as-cast Mg.

1. Introduction

The advantages of cellular metal in various lightweight structures, acoustic and mechanical damping, electrical screening, filtration and biomaterials has provided a stimulus for the rapid development of fabrication routes for commercial production of closed- and open-cell porous metals. However, the majority of these fabrication routes generate a random cell structure, yielding broad distributions in cell size and shape with the result that material properties are unpredictable over the range of a few hundred microns to a few millimeters. This is especially true for cellular metals, where high temperatures required to form structures limit the techniques available for their fabrication. These cellular metals have a wide range of uses, from lightweight structures, acoustic and mechanical damping, to electrical screening, filtration and biomaterials for orthopedic implants. However, by accurately controlling the pore design during fabrication, the overall properties of the cell structure can be altered to meet a variety of needs.

Manufacturing routes for cellular metals with controlled, opposed to random, pore architectures are not that well developed and are typically more difficult and costly to produce. Currently, the main route for the fabrication of controlled cellular structures is by using rapid prototyping (RP) techniques. Cellular metals can be directly fabricated by incorporating selective laser melting (SLM) or selective electron beam melting (SEBM) into the RP process. Ordered cellular titanium and stainless steel structures have been fabricated using these methods. Ceramic scaffolds have also been used to cast CoCr and titanium alloys for orthopedic applications, where the ceramic moulds are either directly fabricated or cast into polymeric RP scaffolds. Another alternative to fabricate titanium implants is to infiltrate polymer RP scaffolds with titanium powder slurry. This is followed by heat treatment to allow wax removal and sintering of the Ti particles. NaCl has also been established as a possible spacer material for random foams, and plaster has been recently used to cast controlled cellular Mg. It has been reported that plaster deposits are on many strut surfaces on porous metal after the removal process.

The present work demonstrates the application of a multistep process for the fabrication of porous magnesium (Mg) that can be used to control the cellular architecture at different topology scales. The high flammability of Mg in the powdered form means that powder processing routes such as selective laser sintering are a formidable and dangerous task, and current processing techniques all results in a foam structure. This has prompted the development of a new liquid metal casting route for cellular Mg that involves the infiltration of a sodium chloride (NaCl) template having the desired ordered architecture. It is demonstrated that NaCl is an ideal template material for casting Mg due to (i) high thermal stability and strength, (ii) non-reactive nature with Mg, (iii) ability to be formed into complex, ordered structures and (iv) ease with which NaCl is removed.

In this thesis, several methods of analysis such as compression testing, scanning electron microscopy (SEM) and electron backscattered diffraction (EBSD) were employed to analyze range of sintered and non-sintered bulk NaCl samples to optimize the sintering condition. Fractography of the NaCl was analyzed using the SEM while the grains of the structure were mapped using the EBSD. There a new approach in polishing the micro porous NaCl samples had to be developed for the use of the EBSD detector in the SEM. For the fabrication of the porous structures utilizing the RP process, the SEM is used for surface analyzes, and micro-computed tomography (μ-CT) is used for volumetric analyzes were the relationship between the CAD model and the final NaCl pore morphology is investigated.

2. Literature review

2.1. Introduction to cellular metals

Cellular metals have been studied since the 1960's. However, it has not been until recent times that they have found commercial applications, mainly due to difficulties with manufacturing reproducibility and their relatively high cost. Porous metals are a very useful class of lightweight but strong engineering materials that are fabricated with either open or closed pores, normally in a random arrangement. The majority of current methods for fabricating polymeric, ceramic or metal cellular materials typically result in random pore architecture, which by its nature leads to inhomogeneous properties at the microstructural level. The high temperatures required to form cellular metal structures increases the complexity and cost of fabrication thus limiting the processing routes available.

Cellular metals have a wide range of potential uses including applications in lightweight structures, acoustic and mechanical damping, electrical screening, filtration and biomedical implants. By accurately controlling the pore design during fabrication, the overall properties of the cell structure can be altered to meet the requirements of these applications. Manufacturing routes for cellular metals with controlled, as opposed to random, pore architectures are less well developed and are typically more difficult and costly. Currently, the main route for direct fabrication of controlled cellular structures is by using rapid prototyping (RP) techniques where the structures are created with metal powders. Alternatively, a mould is created with RP and used to cast the metal with the desired architecture. Section 2.2 will begin by giving a more detailed overview of the various processes for making random structured cellular metal. Sections 2.3 will further expand on this topic by covering the less well-developed area of ordered cellular metal fabrication.

2.2. Production methods of random structured cellular metals

2.2.1. Powder metallurgy

Foaming of slurries

The process compromises mixing metal powder and a blowing agent powder and compacting the mix. The mix can be compacted either by hot pressing, extrusion or powder rolling. The semi-finished product is then heated up to start the gas reaction. This fabrication process is commercially known as FORMGRIP, but that name seems though to have disappeared over the years. Aluminium (Al) foams made by this process are known by the trade as Alulight, Foaminal or ALPORAS.

Creating metal foam by mixing a foaming agent with metal powder by this way is the most controllable method to fabricate metal foams where the pores are shaped by evolving gas during solidification. A foaming agent such as titanium hydride (TiH_2) will begins to decompose at ~465°C, which is well below the melting point of Al and magnesium (Mg), making it the ideal foaming agent for low melting point metals. Zinc hydrate (ZnH_2) and magnesium hydrate (MgH_2) can also be used as foaming agents but are less effective foaming agents compared to TiH_2 [1]. ZnH_2 is an ideal foaming agent for Zn alloys while lead (Pb) can be foamed with basic lead(II) carbonate ($(PbCO_3)_2$; $Pb(OH)_2$) [2].

This fabrication process starts with the mixing of the metal alloy and foaming agent powders (Figure 1). After the ingredients have been mixed thoroughly together, they are cold compacted and extruded to achieve near full density. The extruded material is then placed in a mould that is heat to just above the solidus temperature of the alloy, upon which the TiH_2 decomposes creating closed cell foam within the confines of the mould.

Most of the attention on improving this process has been focused on processing of Al alloy foams [1, 3-6].

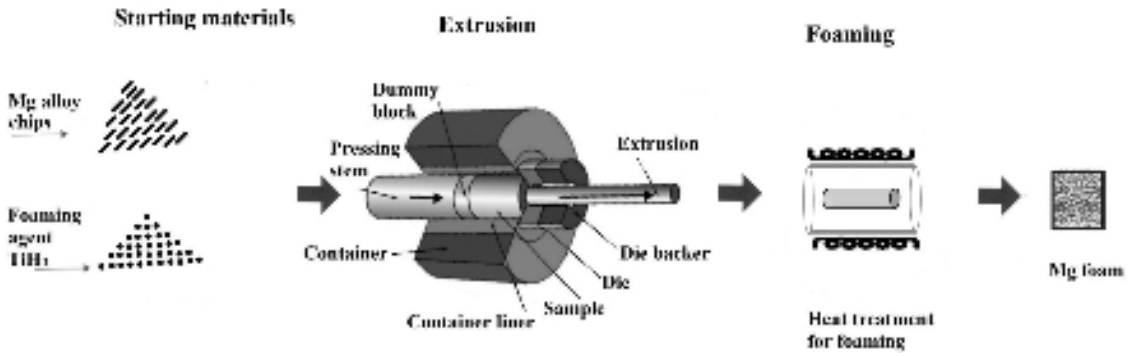

Figure 1: Schematic of the fabrication of a random Mg foam *via* the gas-release decomposition of TiH_2 [7]. The process has 3 main steps: (i) mixing of raw powdered materials, (ii) extrusion to make a dense "green" body and (iii) heat treatment above the solidus temperature.

Entrapped gas expansion

A variant on gas-releasing particle decomposition is to use a gas such as argon (Ar) by entrapping the gas inside the structure under pressure. As the structure undergoes densification during hot pressing or extrusion the Ar forms uniformly dispersed pores under high internal pressure, occupying less than 2% by volume. Subsequently, the alloy is heated which causes the gas pressure within the pores to increase and expand the metal. The expansions takes place at solid state *via* a creep mechanism and is therefore not actually a foaming process but rather a solid state creep process [8].

This process has been developed for titanium (Ti) [8] Al [9] and Mg [10] alloys. Boeing has developed Ti foam with improved properties by using this method in combination with rolling, heat treatment and annealing (Figure 2) [11].

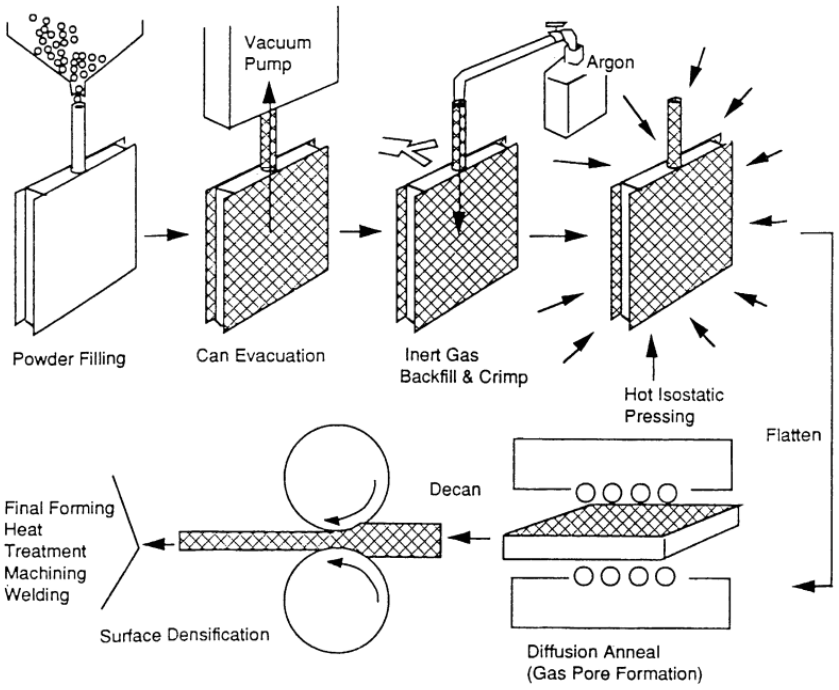

Figure 2: Schematic of gas entrapment technique [12].

A variant on this technique was used to produce a Mg (AZ91 and AZ181) foam where gas is entrapped under atmospheric pressure and the pores are expanded by applying a vacuum [10]. Temperatures just below the melting point of the alloys were found to give the best results or when ~1% amount of fraction slurry was in the melt. The porosity of the foam made by this method is typically 20-40% with the pore diameter ranging from 10 to 100 μm.

Reaction sintering

Reaction sintering involves blending and mixing metal powders (*e.g.* Ti + Al, Fe + Al, Ti + Si, Al + Ni, Ti + C, Ti + B_4C, *etc.*) that are then compacted to make a green powder compact. The precursor is then placed into chamber (Figure 3) and heated under argon to trigger a combustion reaction (Figure 3). That happens because of the different diffusion coefficients of the components in the system [12, 13]. A example of a

intermetallic foam (nickel aluminide) and porous titanium matrix composites (TiB_2, TiC/Ti) combustion reactions are show below [14].

- $3Al + Ni \rightarrow Al_3Ni + 151$ kJ,
- $3Ti + B_4C \rightarrow 2TiB_2 + TiC + 761$ kJ,
- $Ti + C \rightarrow TiC + 185$ kJ.

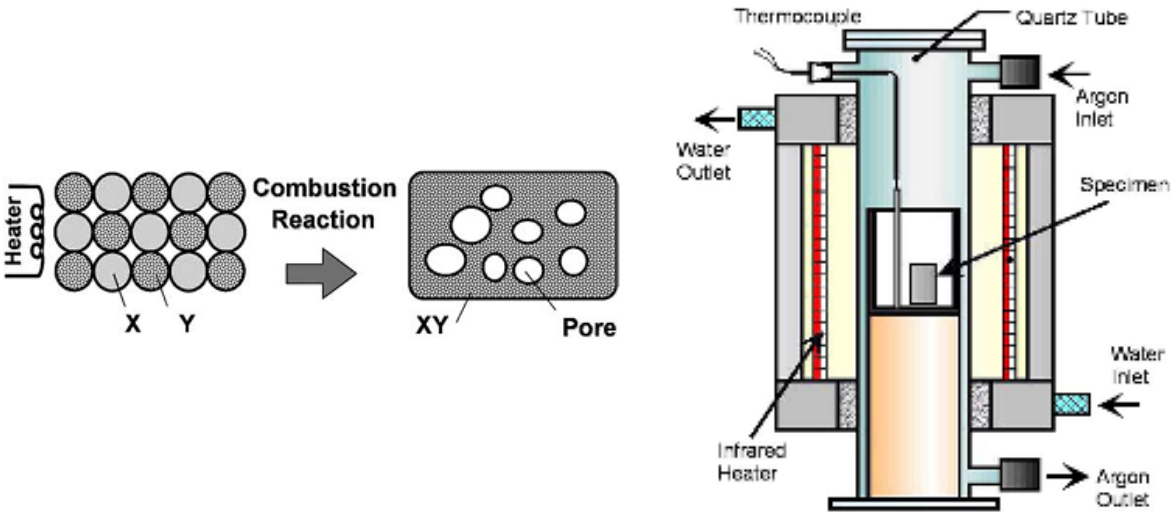

Figure 3: Schematic of (i) the combustion reaction and (ii) an example of an experimental apparatus [13].

Hollow sphere structures

Hollow sphere cellular structures are a class of open and closed cell cellular metal that can be based on nickel (Ni), Ti or steels (stainless and carbon steels). The process begins with fabrication of the hollow spheres which are then usually sintered together to form the cellular metal. The consolidation of hollow spheres results in a mixture of open and closed cells. The relative density of the porous structure can be tailored by adjusting the size and wall thickness of the hollow spheres. There overall density can go

as low as 0.05 and pore sizes in the range of 0.1 mm up to several millimetres. There are various methods that have been developed for the fabrication of hollow spheres including: *[12, 15]*

1. Georgia Tech has developed a blowing method that makes micro-spheres by blowing metal powder, metal oxide powder or metal hydrate powder combined with organic binder and solvents (Figure 4A). After the spheres have been blown they are dried by evaporation in a drop tube followed by final heat treatment to deoxidise or sinter those spheres. This method can use hydrates such as TiH_2 as decomposable precursor or the slurry can also be altered to use oxide powder mixtures such as Fe_2O_3 + Cr_2O_3 to create stainless steel.
2. Polymer spheres (*e.g.* Styrofoam) are immersion-coated with a binder/powder suspension normally polymeric organic binder is used and mixed in a fluidized bed with metallic powder selected from the group of *e.g.* Fe, Co, Ni, Cu, Ti, *etc.* The spheres are then sintered, allowing the polymer to be removed (Figure 4B). This method produces spheres with high uniformity but they are also slightly anisotropic[16].
3. Metallic melts can be atomized and spheres with relative low density are formed. The resulting hollow spheres are then consolidated into a cellular structure *via* normal sintering.
4. A similar process as method 2 above is when polymer spheres are coated with combination of chemical and electrical deposition instead of being immersion-coated.

A

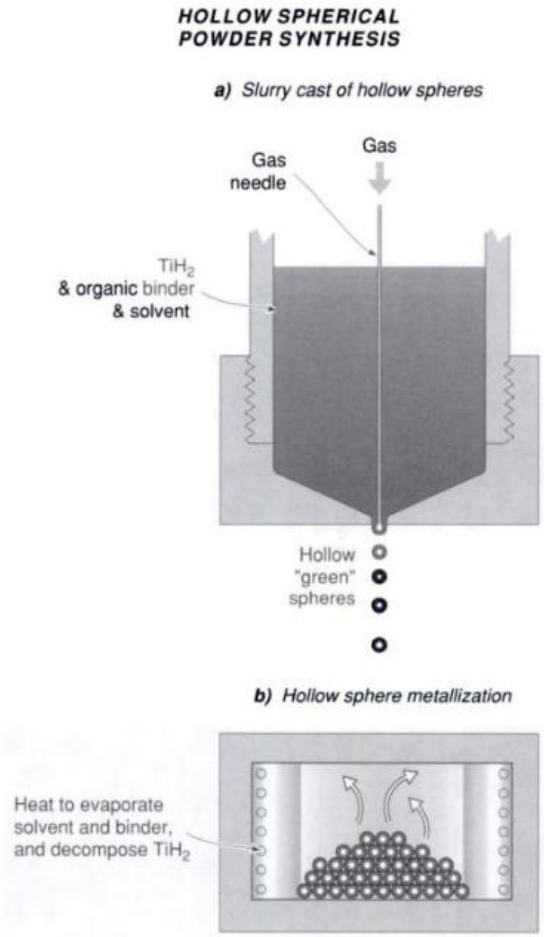

B

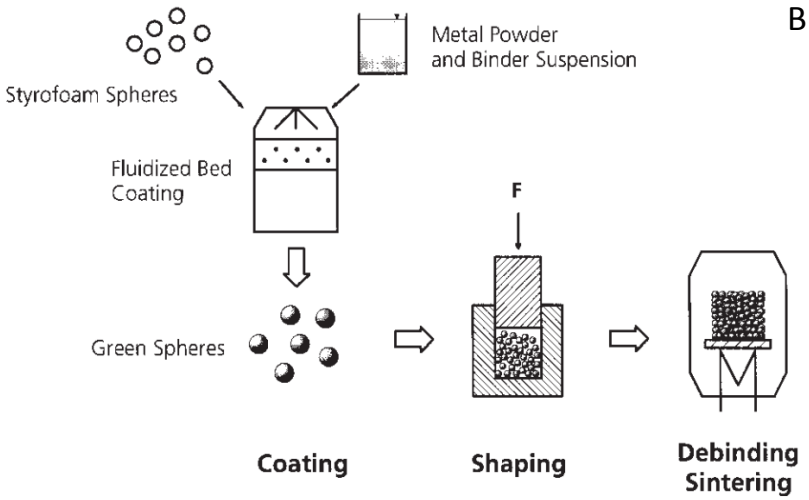

Figure 4: Schematics of (A) Georgia Tech [15] and (B) Styrofoam [17] routes to manufacture hollow sphere structures.

Space-holding fillers

Starting material, metal powder and spacer material is mixed together and compacted into preform. The preform is heat treaded in furnace to sinter the metal powders and remove the spacer material. The metal powder can be mixed with the space holders either dry or mixed with solvent or an organic binder. Many options are for space holder materials, such as polymer grains and spheres, ceramic grain and spheres, salts [18, 19], metal grains [20] and hollow metal spheres [21], method accounted here above. After the metal powder and spacer material have been mixed they are pressed, often under elevated temperature if the spacer material is heat resistant for better compaction. The precursor is then heat treated to remove the spacer material if needed followed up with sintering of the metal powder. Schematic of an example of the process is shown in Figure 5. This method has been used for the fabrication of Ti-based [18, 20], Mg-based [18, 19] and Fe-based [21] alloys such as stainless steel.

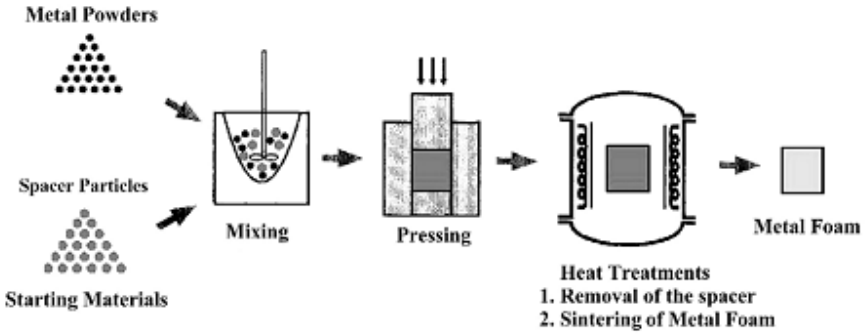

Figure 5: Processing method using the space-holding fillers method [18].

Electrical assisted powder consolidation

Passing an electrical current through a bed of metal powder is an alternative method of sintering that has been used to also produce a cellular metal structure. In this family of processes, consolidation usually requires the simultaneous application of an electrical current and pressure to the powder. One limitation of the process for

fabricating cellular metals is that pore sizes and shapes are uniform throughout the structure. The question arises whether this process should be classified as a fabrication process for cellular metals with ordered structure, but since there is very limited control over the pores it is not. However, in another sense these materials can be designed with an ordered structure since it is possible to produce a functionally graded pore distribution in the final cellular metal.

The process is also known as field-assisted consolidation technique (FAST) [22], electrical discharge compaction (EDC) [23, 24], and spark plasma sintering (SPS) or pulsed electric current sintering (PECS) [25, 26]. In general, each of these methods involves sintering of metal powders using rapid heating *via* an electrical current and pressure-assisted sintering. In general, the advantages of electrically-consolidated metals are shorter holding times, lower temperatures and improved properties. A schematic of the FAST process is shown in Figure 6, where graphite pistons in a die are commonly used to uniaxially compress the powder.

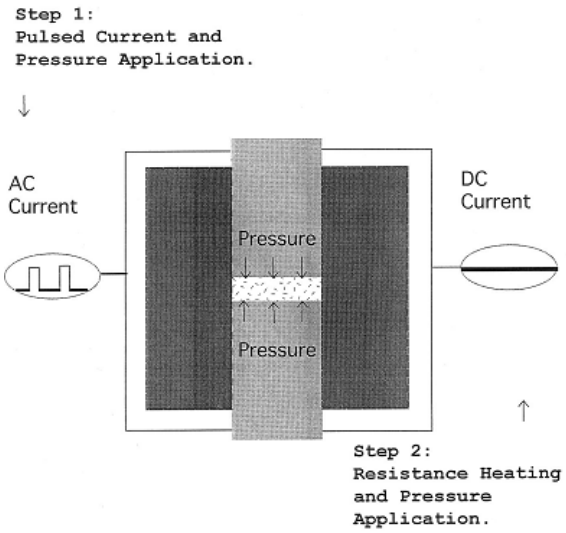

Figure 6: Schematic of the process known as field-assisted consolidation technique (FAST) [22].

The FAST sintering process consists of two stages: (i) initial activation with a pulsed voltage (AC) and then (ii) densification by direct current (DC). The pulse discharge involves low voltage (~10 V) and high current (~1000 A). The main difference between EDC and FAST is that EDC uses one discharge while multiple discharges are used in FAST.

Conventional methods of sintering Ti powders require high temperature (1200–1400°C) and vacuum for long periods of time. EDC and FAST can easily sinter Ti powder due to the plasma created by the high current discharge. The plasma is able to melt the oxide films on the particles, allowing the particles to contact each other and bond. Hence, EDC has been used to fabricate porous Ti materials using powders as the starting material [24, 27].

Open cellular Mg has been fabricated by pulse electric current sintering (PECS) of Mg chips. Open cellular Mg-Al alloy foams with porosities of 50-78% have also been fabricated from chips produced with a lathe by compressing the chips to required density before using PECS under Ar [28].

2.2.2. Accumulative roll-bonding

By accumulative roll-bonding (ARB) process, blowing agent is incorporated into bulk material by rolling it in between bulk Al sheets. Porous cellular Al is generated by heating when the blowing agent releases gas into the metal (Figure 7). Blowing agent (TiH_2) is placed between the two Al sheets that are rolled two times at room temperature, with draft percentage of 50%. The sheet was heat treaded at 200°C and cut between the rolling. The final 3 mm sheet is then heat treated to activate the blowing agent. The process generate cellular Al with ~40% porosity [29]. As being very similar to the gas-releasing particle deposition process for powders, the main advantages with this process is to be able to use conventional sheets instead of expensive powders [30]. The process has also been adopted to fabricate Mg with 77% maximum porosity [31].

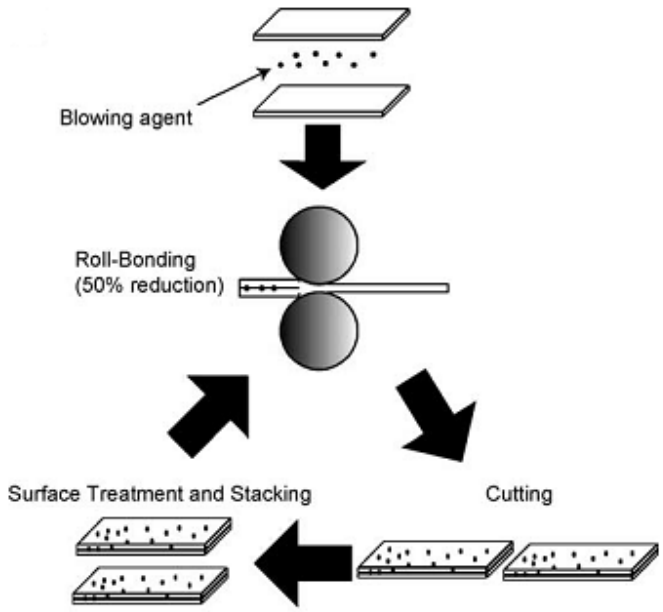

Figure 7: Schematic of accumulative roll-bonding (ARB) fabrication process [29].

2.2.3. Liquid metal routes

There are two main methods for fabricating metal foams from the liquid phase: (i) direct injection of gas bubbles into the melt or (ii) addition of secondary metal particles to the melt that act as blowing agents. Studies of the foaming metals using this technique were numerous in the 1960s and 1970s although the processes were not commercialised. In the last 15 years, the liquid metal routes have gained more attention again with some improvements in the production process for Al, Mg and zinc (Zn) alloys [12].

Melt gas injection

Gas-injection was developed by Alcan International is the least costly method to produce metal foam. The introduction of very fine gas bubbles to the melt is achieved by injecting gases (air, nitrogen or argon) into the melt through rotating impellers or vibrating nozzles. The gas bubbles rise to the surface of the melt, dragging liquid metal to the surface. The liquid foam is stabilised through the addition of fine ceramic

particles, collected at the surface of the melt and subsequently allowed to solidified, resulting in a rigid metal foam [32].

Al alloys are the most successful to foam using this process due to their low density and low oxidation potential. This method has been exploited by Hydro Aluminium (Norway), Cymat Aluminium (Canada) and ALCAN International (Canada). Pure metals cannot be foamed easily by bubbling unless an addition of 10-20 vol.% of fine ceramic particles (*e.g.* aluminium oxide, silicon carbide and magnesium oxide with particle sizes of 5-20 μm) is made to the melt. The ceramic particles are selected to be thermally stable in the melt and hence used to raise the viscosity of the melt so that the collapse of liquid bubbles at the surface is reduced or avoided. Slabs of foam are produced with closed cells with relatively large diameters of 3 to 25 mm [12, 15]. Both hydrophobic and hydrophilic particles can act to stabilize the aqueous foam for the particle size range [33].

There are two common variations on this method depending on how the foam is collected from the crucible containing the melt (Figure 8). The process can use a horizontal conveyor belt to pull the foam from the melt such that cells are sheared in the longitudinal direction by the conveyor motion. A vertical conveyor belt can also be used although the weight of the foam can cause flattening of the cells near the bottom of the foam [32]. Using these collection methods, the slab of foam can be as long as desired, as wide as the crucible and usually has a thickness of ~10 cm. Al foams produced using this method have high porosity, ranging from 80–98%.

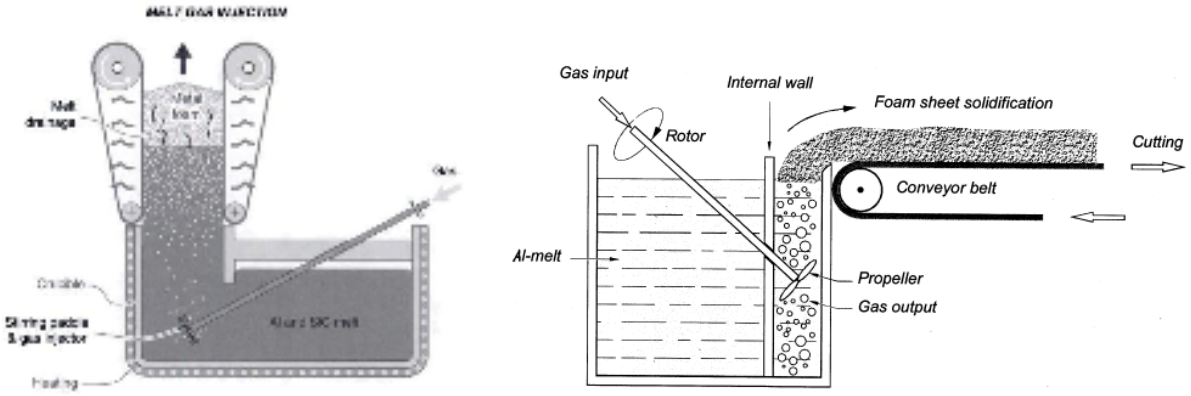

Figure 8: Injection gas manufacturing for producing Al foam using (i) vertical [15] and (ii) horizontal [12] conveyor belts.

Particle decomposition

Closed cell metal foams can also be produced from the liquid phase by using additions of blowing agent particles that release hydrogen gas in the melt. Typically, 1.6 wt% of TiH_2 particles are added to the melt, along with calcium additions that act to increase the viscosity of the melt, increasing its foamability [34]. Both, higher calcium content and increased stirring of the melt increase the viscosity of the melt which, along with the cooling rate, determines the final cell size in the range of 0.5-5 mm (Figure 9). Another study has shown that adding alumina particles into Al-Si-Mg alloy is necessary to promote nucleation and increased viscosity for increased foamability [35]. In general, this process is limited to Al foams since TiH_2 decomposition is too rapid in higher melting point liquids; additionally, other metals are embrittled by hydrogen. The other limitation of the process is that it is a batch process in contrast to continuous gas injection process *[32, 36-38]*.

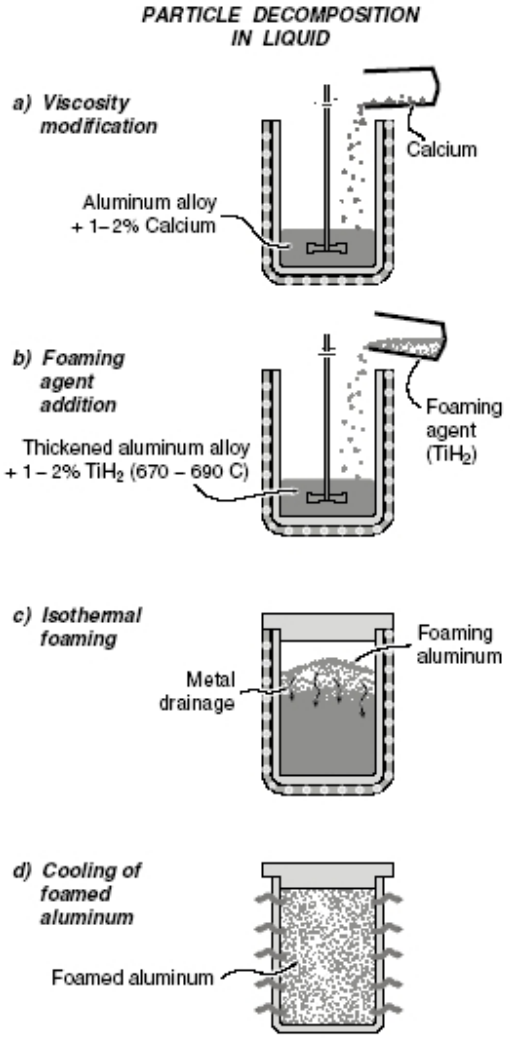

Figure 9: The process steps to manufacture Al foam by particle decomposition in the melt [15].

2.2.4. Metal deposition processes

Metal deposition processes involve coating open cellular polymer structure with metal and then removing the polymer to leave behind open cellular metal structure. The two main methods used for depositing metal onto cellular polymer are (i) electro-deposition and (ii) chemical vapour deposition (CVD). Since the open cellular polymer structure acts as a template for the final porous metal structure, control over cell size is

governed by the starting cellular polymer used. Another feature of these cellular metals is that the struts of the open cell structure will be hollow ligaments due to the removal of the polymer template. These hollow ligaments can be densified by further sintering after the polymer template has been removed.

In the electro-deposition process a conductive polymer template is required. The required conductivity is achieved by (i) dipping the polymer template into electrically conductive slurry that is based on graphite or carbon, or (ii) cathode sputtering. After electroplating with metal, the polymer is removed by heat treatment (Figure 10). This process is limited to only a few metals including nickel, nickel-chromium and copper.

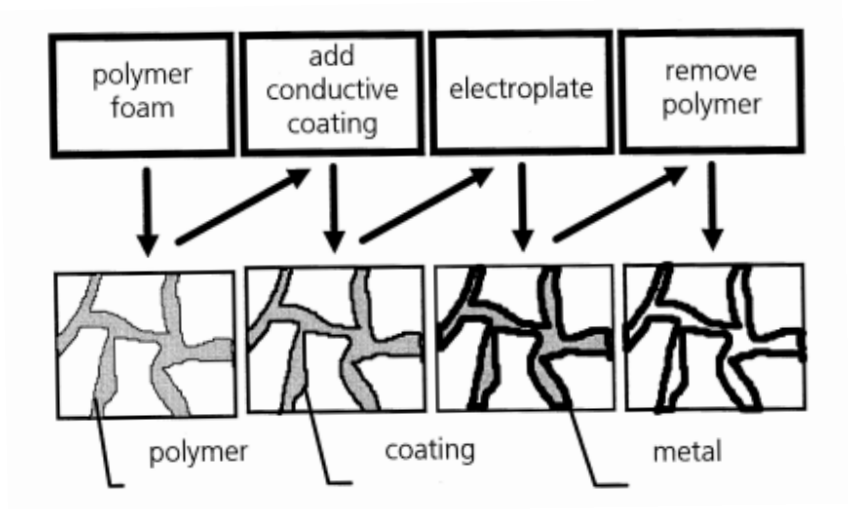

Figure 10: Schematic of the electro-deposition technique for fabricating open cellular Ni or Cu structures [12].

Chemical vapour deposition is a very similar to the electro-deposition process, except that a conductive coating on the polymer is not required. The polymer is first coated by using metal vapour which is allowed to condense onto a cold polymer surface (Figure 11). The metal layer thickness is controlled by the vapour density and exposure time. Nickel carbonyl is then produced by heating nickel and carbon monoxide above 120°C as shown by the reaction below.

$$Ni + 4CO \xrightarrow{>120^{\circ}C} Ni(CO)_4$$

A stream of nickel carbonyl gas is permeated through the polymer template, resulting in nickel accumulating on the surface of the polymer template to form a Ni coating. During this process the polymer is held at the required temperature for the nickel to decompose *via* infrared heating. After cooling down the metal-coated polymer, the polymer is then removed by heat treatment. Finally, sintering is used to increase the density of the hollow ligaments in the structure [39].

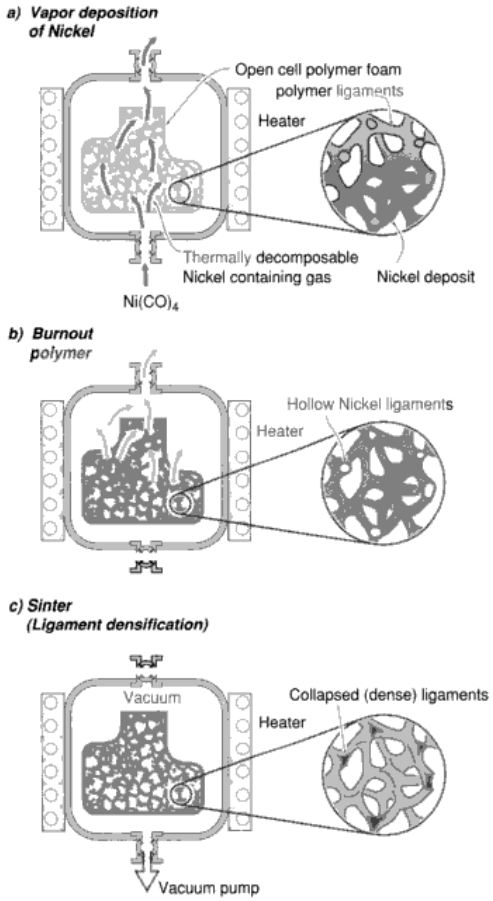

Figure 11: Schematic of chemical vapour deposition process for producing open cellular nickel structure (INCO process) [15].

2.2.5. Casting methods

Casting using a polymer template

Open cellular metal can be fabricated using a polymer template (*e.g.* open cell polyurethane foam) that is a replica of the final desired metal foam structure. The polymer template is first fully infiltrated with either casting sand or Plaster of Paris in the form of slurry (Figure 12). After slurry infiltration, the polymer template is removed by careful heat treatment so as to not crack the plaster. Once the polymer is removed, the resulting negative replica is used as a mould for the metal casting. Application of pressure or heating of the mould is usually necessary when casting to allow full infiltration of the melt into all cavities. After solidification and cooling the sand or plaster is removed by vibration or water spray, respectively [40, 41].

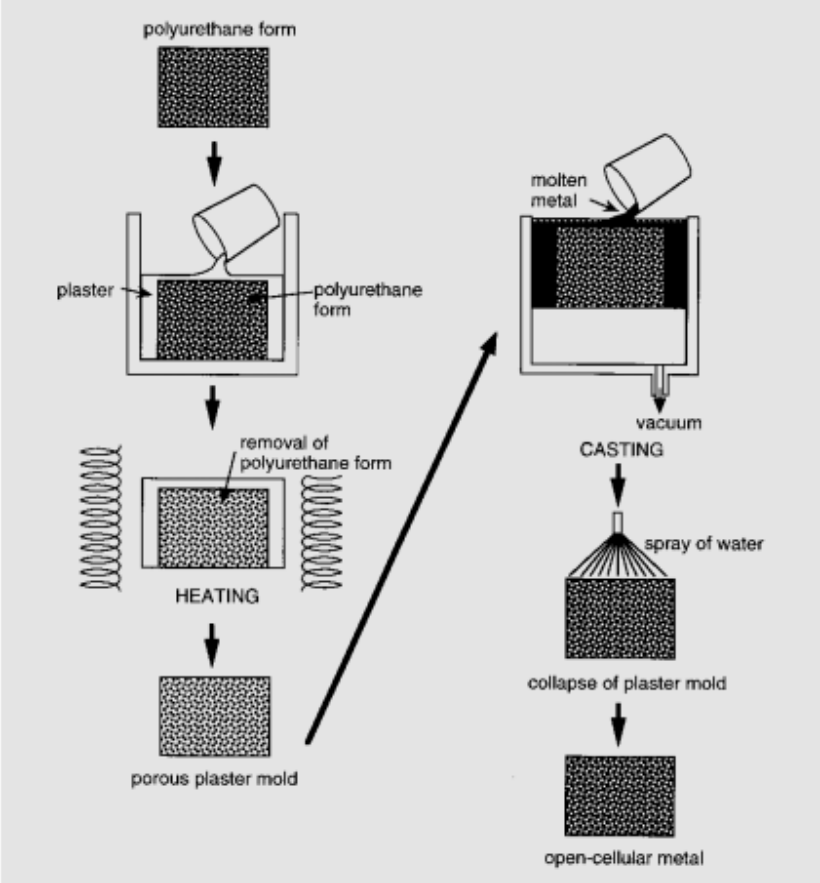

Figure 12: Schematic of the casting process for producing open cellular metal *via* a polymer template and plaster mould [42].

Casting using space holder materials

One of the simplest ways to fabricate cellular metals is via a replication process using space holder materials. It is produced by (i) casting liquid metal into a randomly arranged bed of space-holding particles (Figure 13) or (ii) introducing the spacer particles into the melt. The space holder material is then removed once the metal solidifies by leaching or heat treatment, leaving a porous metal structure. In practice it is almost inevitable that a certain amount of space holder materials are trapped inside the final metal structure due to not having a 100% fully interconnected pathway between all spacer particles. Spacer particles that are isolated from any other particles will likely become trapped. There are two main requirements that the spacer material needs to

fulfil: (i) chemically stable while in contact with the liquid metal phase and (ii) ease of removal after solidification

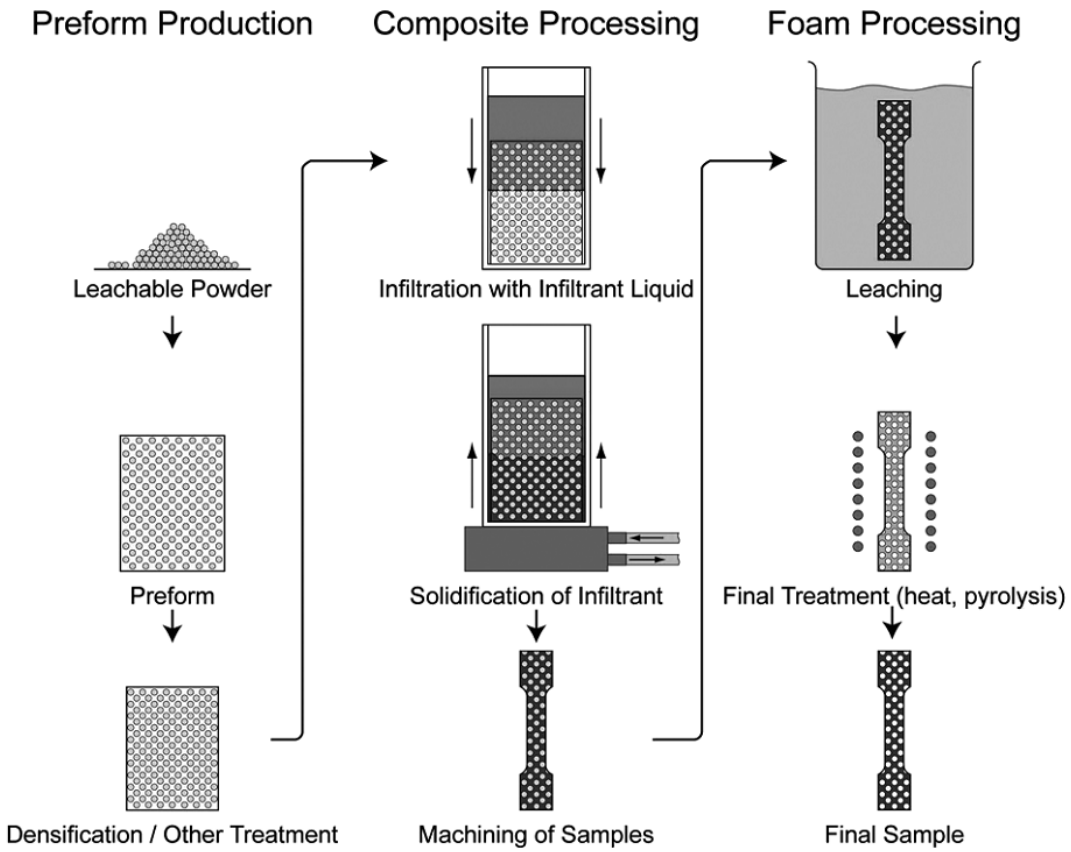

.

Figure 13: The replication process step-by-step using leachable space holders.

A range of different space holder materials have been used to cast different alloys. Al has been fabricated using resin coated polyurethane spacers where the polymers are removed by heat treatment after casting the Al *via* high pressure infiltration process [43]. Mineral space holder materials, *e.g.* vermiculite (Zonolite), perlite, ground refractories, fired clay pallets *etc.* have and been used for low melting points alloy and are easily removed by heat to decompose the binder [44]. Sodium chloride (NaCl) has a melting point of 801°C and is therefore a good candidate for fabrication of metals such as Al and Mg that have a lower melting point. NaCl is also easily removed by dissolution in

water. One well known major disadvantage using removable space holder grains is that some of the grains get entrapped by metal so they can not be removed. Therefore it is very hard to make sure that all the spacer material has been removed. NaCl particles can be fused together by sintering before casting for improved interconnectivity, leading to a reduction in entrapped spacer particles [45-48]. Example of the cellular Al structure fabricated by this method is shown in Figure 19.

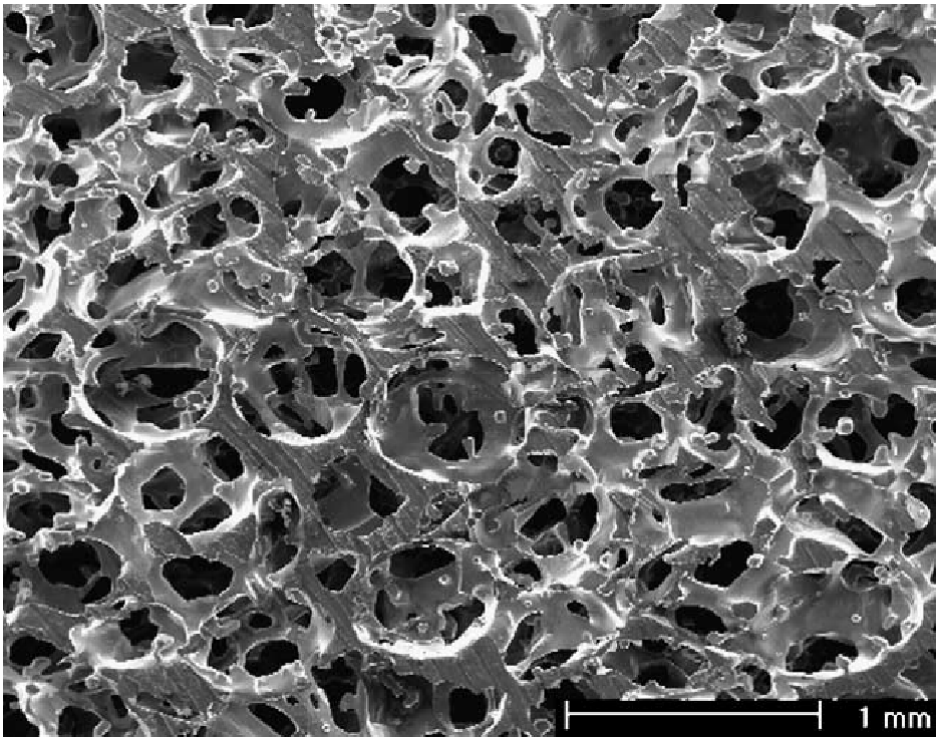

Figure 14: Structure of cellular Al fabricated using uniform NaCl spacer grains [49].

Heating the space holders is normally necessary to prevent solidification of the melt during infiltration, especially if the heat capacity of the spacer material is high. High surface tension and insufficient wetting of the spacer materials may mean gravity casting is not sufficient for infiltration of the spacer material. Additional applied pressure on the melt may be required to achieve full infiltration between all spacer particles.

2.3. Ordered structure cellular metals

2.3.1. Three-dimensional printing

In recent years, solid freeform fabrication processes such as three-dimensional printing (3DP) have been used to fabricate cellular metals. 3DP creates a part directly from a 3-D computer model. 3DP is able to create porous materials with undercuts, overhangs, and pores of controlled size, shape and distribution. The parts are created inside a cavity that contains a powder bed that is supported by a piston. The shape of the part is formed by selectively bonding desired regions of the powder layer by ink-jet printing a binder material. Another layer is added by dropping the piston down and spreading a new layer of powder – this is repeated until the part is completed. The "green" part is then heat-treated to consolidate the bonded material (Figure 15). 3DP can be used for a wide range of materials including metals, ceramics, metal-ceramic composites and polymeric materials.

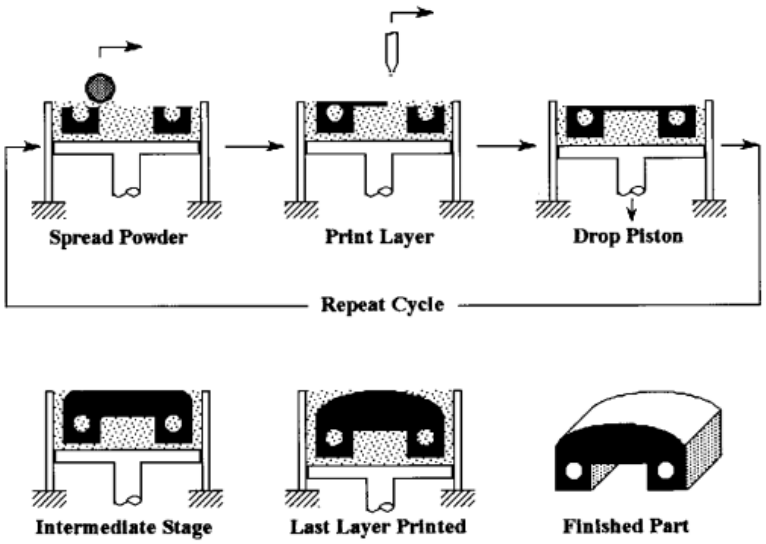

Figure 15: Three-dimensional printing process [50].

There are two different routes to fabricate 3DP cellular metals: (i) direct metal printing and (ii) indirect methods that involve fabrication of a mould in which to cast the

metal. Ceramic scaffolds are used to cast CoCr [50, 51] and Ti [52] alloys for orthopaedic applications where the ceramic mould is either directly fabricated or cast using first a polymeric scaffold made with 3DP. Sodium chloride and flour powder mixtures have also been used as mould materials to cast ceramic moulds for subsequent metal casting [53]. Another alternative to fabrication of porous Ti is to use polymer scaffolds fabricated using 3DP. The polymer scaffold is infiltrated with Ti slurry, followed by drying and scaffold removal in furnace. The Ti composite structure is then washed in xylene solution for total removal of the polymer 3DP scaffold. The cleaned structure is heat treated under high vacuum when sintering the Ti particles to form solid structure [54, 55]. Examples of the ordered cellular Ti fabricated by this method are shown in Figure 16.

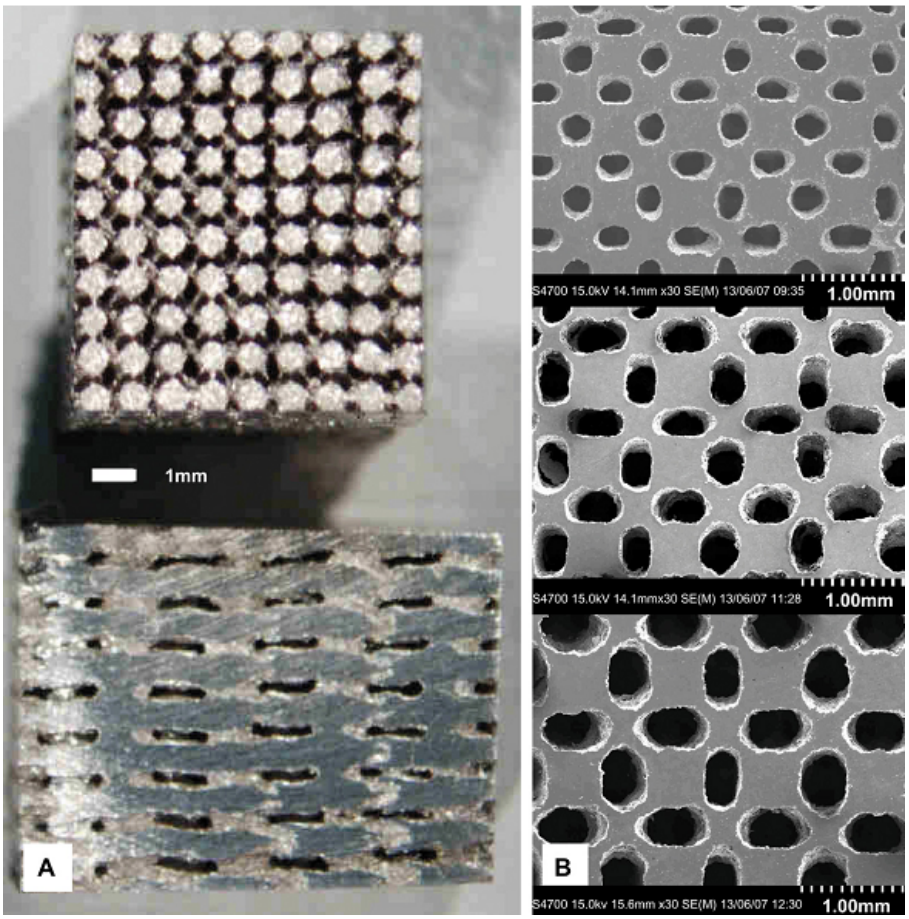

Figure 16: Porous Ti scaffolds fabricated via three-dimensional printing [55].

Cellular metals can be directly fabricated by integrating selective laser melting (SLM) or selective electron beam melting (SEBM) with the 3DP process. The process cycle is similar to the conventional 3DP process except the metal particles are fused together immediately by laser or electron beam (Figure 17). Ordered cellular Ti [56, 57] and stainless steel [58] have been fabricated using this process.

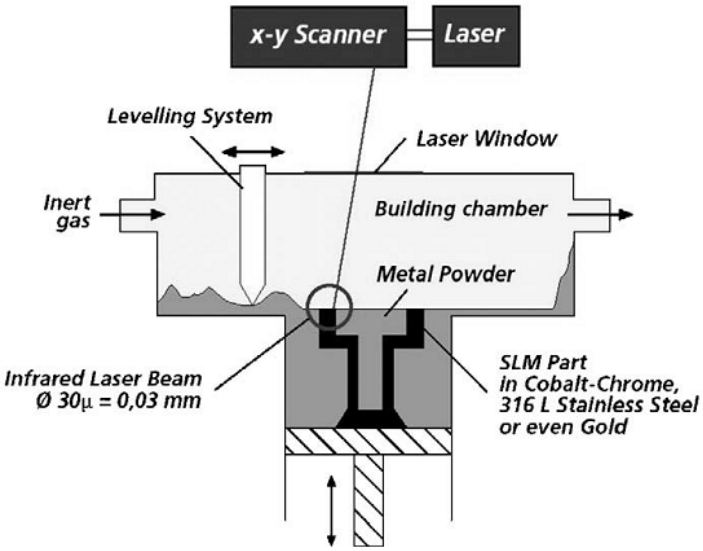

Figure 17: Direct three-dimensional metal printing process [56].

2.4. Properties and applications of cellular metals

Although cellular metals have favourable characteristics such as low density, good insulative properties and high specific mechanical properties, the main hurdle they must overcome to more widespread use are the high production costs and manufacturing complexity, especially for ordered cellular metals. Hence, cellular metals hold most promise for industrial applications where strength and lightness are of high importance, particularly transportation industries. Other industrial applications where they have found usage are in filtration, heat exchangers, storage of liquids, fluid flow control, silencer, battery electrodes, flame arresters, water purifying, acoustic control and orthopaedic implants. Banhart notes four important characteristics that cellular metals must fulfil in order to be suited to an application [12]:

- Morphology: What type of porosity required such as open or closed cells, density, size of pores, shape and volume fraction?
- Metallurgy: Is metal casting or powder metallurgy required?
- Processing: Is there a process to manufacture the cellular metal required?

- Economy: Is it cost effective for high volume production?

Banhart has attempted to group applications of cellular metals according to the cell "openness" required and type of application (functional or structural) (Figure 18). There is a need for greater closed cell porosity as the demands of an application are more dominated by structural rather than functional requirements, and vice versa.

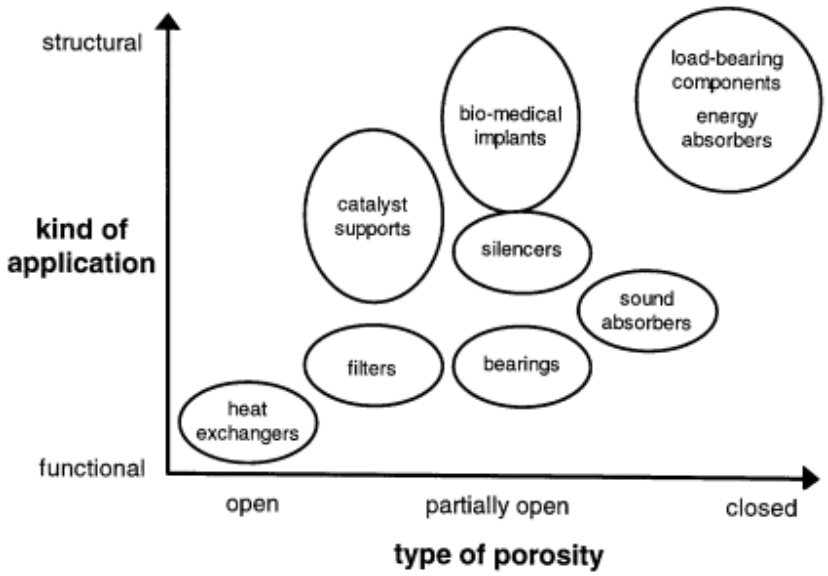

Figure 18: Applications of cellular metals chart [12].

2.4.1. Biomedical applications

Porous metals have gained attention recently as potential implant materials for fixation in orthopaedic applications. Screws, bone cements and roughened surfaces on implants have been mainly used to assist with bone fixation. More recently, open cellular metals such as Ti have been investigated for their potential to assist with fixation of new bone to an implant device.

Cellular metal implant devices have the potential to match the natural modulus of bone which helps to reduce problems with stress shielding. Furthermore, open, interconnected porosity allows bodily fluids to flow into the device which assists with bone in-growth. Cellular Ti has been the main candidate material in these orthopaedic applications due to its widespread use as a monolithic implant material. Stainless steel and Co-Cr alloys have also been widely used, although due to lower corrosion resistance and mechanical properties are not as popular as Ti [59]. The modulus of Ti is around 110 GPa. By having so stiff material inside the bone causes problems, such as high stress concentrations and abnormal overall stress patterns are common in current Ti spine implant devices [60].

Mg offers advantages over other orthopedic implant materials such as bioceramics, stainless steel and Ti including lower stiffness and biodegradability [61]. Recently Mg alloys has gained more attention as a promising biomaterial for bone substitutes because of its excellent mechanical properties, biodegradability and biocompatibility. Mg is the lightest of all structural metals, weighting only 1738 kg/m^3, compare to bone it has very similar density, but a bit higher though. The static elastic modulus for Mg (99.98% purity) is 40 GPa and 44 GPa in dynamic, making it around half times stiffer than cortical bone. The strength of unalloyed Mg is not so good compared to bone. The strength of a cortical bone is about 200 MPa and the 0.2% tensile and compressive yield strength is 21 Mpa (Table 1). Biodegradable implants have been around for decades; however degradable metal implants for bones are one of the recent new areas of interest for scientist. There has porous Mg good potential to be a good biodegradable implant for bones.

Table 1: Magnesium properties

Property	**Value**	**Comment**	**Reference**
Density, ρ	1738 kg/m^3	25°C	[62]
Density, ρ_m	1650 kg/m^3	650°C, solid state	[62]
Density, ρ_l	1580 kg/m^3	650°C, liquid state	[62]
Melting point, t_m	650°C	-	[62]
Viscosity, μ	1230-1250 Pa·s	650°C	[62]
Elastic modulus, E	40 GPa	20°C	[63]
0.2% tensile strength, σ_o	21 Mpa	20°C	[63]
0.2% compression strength	21 Mpa	20°C	[63]
Surface tension, γ	0.545-0.563 N/m	660-852°C	[63]

Mg (AZ91D) implant with random architecture (Figure 19), fabricated using NaCl space holder casting technique has been tested in *vivo*, using rabbit model and has showed good biocompatibility. Major scaffold degradation was completed within 3 months leading to a complete replacement of the Mg implant by bone tissue. Those results are very promising and show that Mg based implants are very promising approach in the development of mechanically suitable porous scaffolds for replacing subchondral bone [64, 65].

Figure 19: Random structured cellular Mg scaffold [64].

2.5. Gaps in the literature

Manufacturing routes for cellular metals with controlled, as opposed to random, pore architectures are less well developed and are typically more difficult and costly to produce. Currently, the main route for the fabrication of controlled cellular structures is by using rapid prototyping (RP) techniques. Cellular metals can be directly fabricated by incorporating selective laser melting (SLM) or selective electron beam melting (SEBM) into the RP process. Ordered cellular titanium [56, 57] and stainless steel [58] structures have been fabricated using these methods. Ceramic scaffolds have also been used to cast CoCr [50, 51] and titanium [52] alloys for orthopaedic applications, where the ceramic moulds are either directly fabricated or cast into polymeric RP scaffolds. Another alternative to fabricate titanium implants is to infiltrate polymer RP scaffolds with titanium powder slurry [54, 55]. This is followed by heat treatment to allow for wax removal and sintering of the Ti particles. Some porous materials, such as Mg, are not able to be constructed using commercial rapid prototyping processes because of physical difficulties with its powder processing as well it is highly flammable nature. These thus require an alternate path for accurate and safe production [40]. NaCl is an ideal template material for casting various porous materials with lower melting point (801°C), due to its biocompatibility and ease of removal via dissolution [64, 65]. Plaster

has been recently used to cast controlled cellular Mg [40, 41]. However, it has been reported that plaster deposits remain on many strut surfaces on porous metal after the removal process [66].

The aim of this study is to develop a robust fabrication method for producing ordered porous Mg structures via a rapid prototyping and NaCl casting process. NaCl is selected as the template material due to its compatibility in the biological environment. When the template material is not compatible in biological environment every remains of the material has to be removed, processes that can damage excitable material like magnesium.

3. Experimental methods

3.1. Manufacturing of porous magnesium with controlled architectures

3.1.1. Introduction

In this work a fabrication route was developed for producing open cellular Mg with controlled architecture. Fabrication relies on a multistage inverse templating technique (Figure 20). The Mg part is first designed in Solid Works 3-D CAD software and a polymer replica of the part is made by a rapid prototyping (RP). RP produces a positive replica of the Mg part that is then infiltrated with sodium chloride (NaCl). This is then followed by burning off of the polymer, giving a NaCl negative replica. The resulting negative template is then subjected to low pressure die casting with Mg. Subsequently, the NaCl template is removed with sodium hydroxide solution, resulting in porous Mg with a controlled structure.

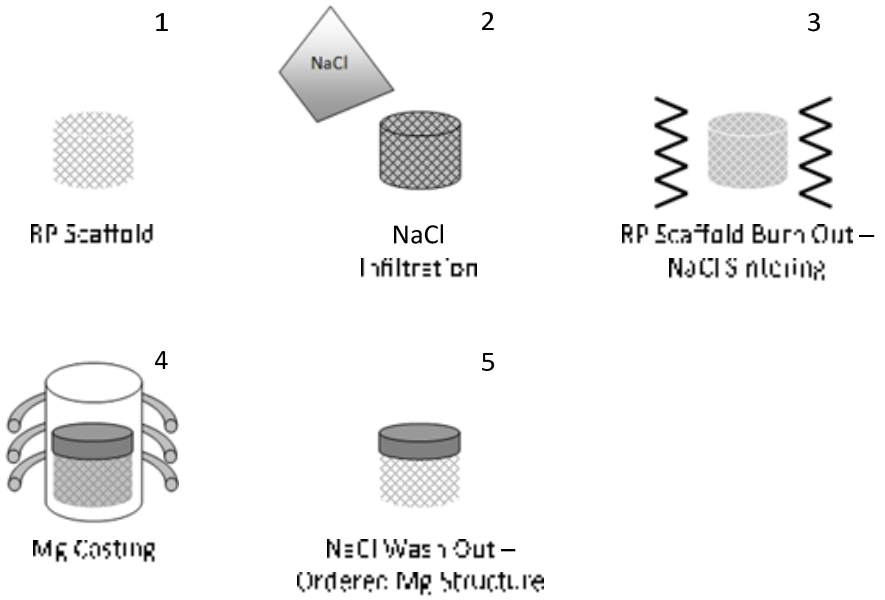

Figure 20: Schematic of the multistage inverse templating technique for porous Mg.

Also a monolithic NaCl samples were fabricated using the same processing method to analyse sintering. Surface and grain analysing were performed using SEM

and EBSD techniques. Strength and modulus were measured by strain using compression testing. X-ray microtomography was used to analyse the effect of the processing parameters on the internal microstructure and architecture of the ordered NaCl cellular structure. The objective of that work was to determine the dimensional differences between the original 3-D CAD model and fabricated NaCl template.

3.1.2. Fabrication route

Production of polymer replica

In order to fabricate the sodium chloride template a polymer scaffold mould was first made with RP. A replica of the Mg part is designed in 3-D CAD software and then transferred to the RP modeller as an STL file (Figure 21). Four rapid prototyping methods where investigated for the creation of the polymer scaffold: (i) Solidscape® T612 Benchtop, (ii) EnvisionTEC Perfactory® R05, (iii) EnvisionTEC Perfactory® PIC 100G, and (iv) InVision® VisiJet® HR 200.

While the Solidscape system proved to have the best accuracy, the build material rapidly dissolved when infiltrated with NaCl. envisionTEC R05 did not fully burn off, leaving a char over the sodium chloride structure. PIC 100G by envisionTEC did not cure fully such that it remained in a rubbery state, resulting in poor dimensional stability. This problem was due in part to the fact that the manufacturer did not have any experience using the PIC 100G material and was not equipped with the required UV source for optimal curing. The VisiJet HR 200 from 3D Systems was found to have the best properties for this application (also see Appendix for technical data). VisiJet HR 200 was completely removed by burn-out with no residual. VisiJet HR 200 exhibited adequate strength and stiffness, resulting in minimal deformation of the scaffold during infiltration. The InVision HR system uses a wax support material during the building of the part. The wax is then drained from the structure post-processing by melting. After building the samples, if any of the parts had residual wax this was removed by wrapping the sample in paper towelling and placing in an oven at 50-60°C. The towelling was

used to help wick away the residual wax. Several heat treatments were necessary to remove the wax completely, leaving a completely open polymer scaffold.

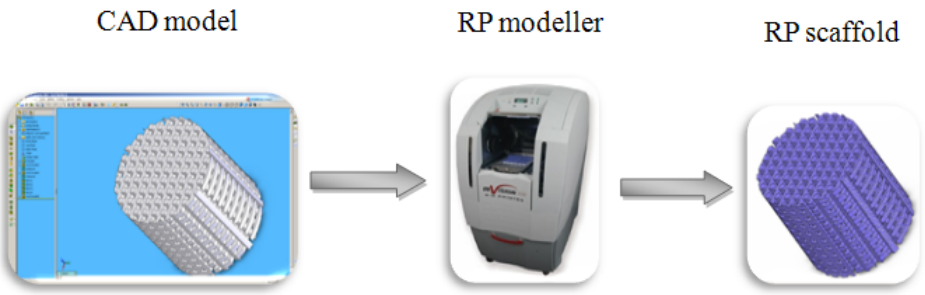

Figure 21: The RP process from CAD model to final part using the InVision HR system.

NaCl paste preparation

High purity (99.5%) NaCl (AnalaR®) was ground and sieved to produce particles of < 63 μm using a centrifugal Retsch ZM100 milling machine and Fritch ®analysette sieve shaker. During this process, NaCl was handled at less than 75% relative humidity to avoid moisture absorption. The grinding mill uses pin rotors that move at 18,000 RPM. NaCl was passed through the mill 4 times to achieve a large proportion of particles in the < 63 μm range. A NaCl paste was specially formulated for infiltration of the polymer RP scaffold. The NaCl paste was composed of 7.9 wt. % gelatine powder (LabChem), 19.3 wt. % supersaturated NaCl solution and the remainder was < 63 μm NaCl particles. The function of the supersaturated NaCl solution was to lubricate the added NaCl particles without drastically changing their shape or size. Gelatine is a widely used component in many products and has also been proposed as carrier material for NaCl in cosmetic hair treatments [67]. The paste ingredients were mixed by hand stirring for ~30 min before usage.

Laser Particle Analysing

Milled a sieved NaCl grains size were measured using laser particle analyser. X100 Microtrac particle size analyser was utilised, using ethanol fluid as carrier. With measuring range from 0.021 to 704 microns the Tri-Laser uses precise angular measurement of scattered light through a full 180 degree angular range with three lasers and two detector arrays to measure the particles. Microcomputer calculates size distribution of particles in the sample stream and provides a printout of the particle distribution.

Infiltration of RP polymer scaffold

The NaCl paste was infiltrated into the RP scaffold by using a specially designed infiltration device based on compressive and vacuum infiltration (Figure 22). An Ø20 mm cylindrical polymer scaffold was produced by RP. The RP scaffold is placed into the infiltration device on top the filter unit before the NaCl is placed on top. NaCl paste was fed in from the top of the device using a 10 ml syringe (with the end removed). NaCl paste was fed into the syringe tube while simultaneously sliding the syringe piston slowly downward to avoid air entering the NaCl paste. The paste was then fed into the infiltration device and placed on top of the RP scaffold. After the NaCl paste has been placed the filter and the piston and there components are placed on top. The sandwich mould was constructed from Perspex and all metal components were stainless steel for corrosion resistance (also see Appendix for drawings).

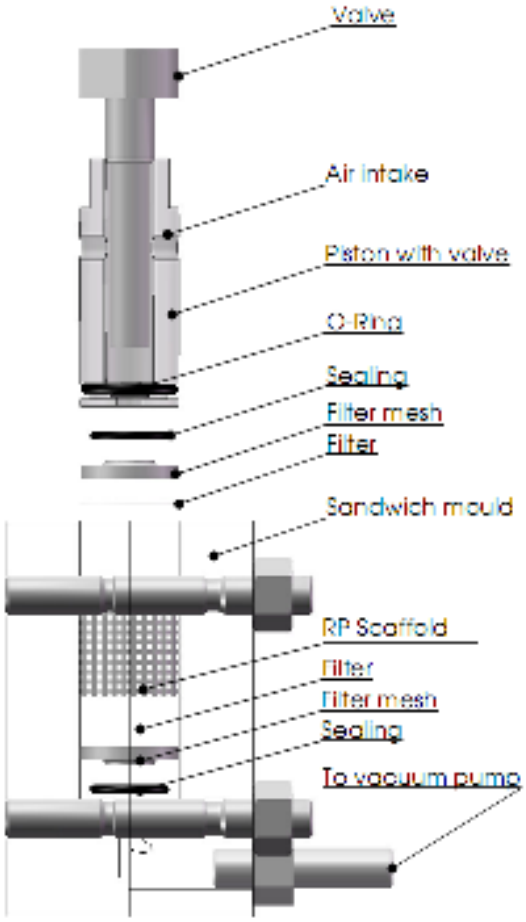

Figure 22: Sodium chloride infiltration device.

The infiltration device is then placed in the press (Figure 23), and the NaCl paste is squeezed into the scaffold by slowly increasing the pneumatic air pressure up to 2 MPa. The infiltrated polymer scaffold is kept under 2.0 MPa pressure for 1 hr in an oven at 50°C, allowing the paste to flow more easily as the viscosity of the gelatine is decreased. Once the gelatine has heated up the valve in the piston is opened, the pressure is decreased to 0.5 MPa and a vacuum is applied (Hitachi 3VP-C 50 L/min). The vacuum draws out most of the gelatine from the scaffold structure through a filter placed beneath the scaffold while a filter at the top of the scaffold allows air in. No. 40 filter paper is used in combination with a filter mesh made from an inline filter unit

(MILLEX® 0.22 µm). The vacuum is applied for ~22 hrs to dry the infiltrated scaffold, allowing the production of one NaCl-polymer composite scaffold per day per mould.

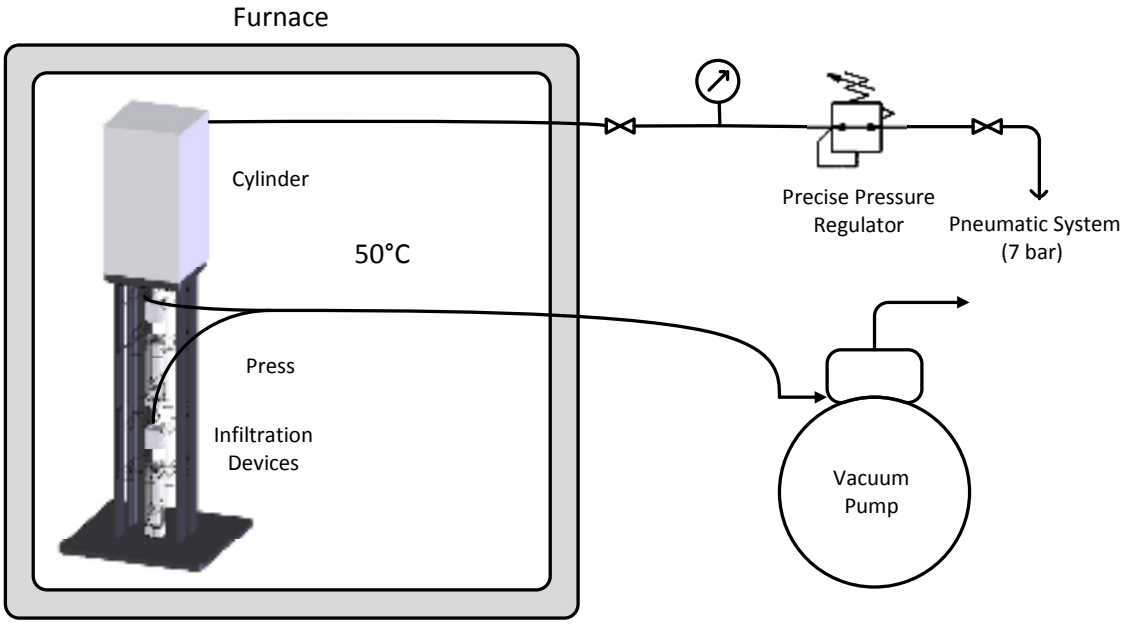

Figure 23: System setup for NaCl infiltration and pressure holding step.

Both monolithic and porous samples of NaCl were studied. Monolithic samples of NaCl were fabricated using the same methods as for the porous Mg except that an RP scaffold was not required. As no scaffold was used in the monolithic process, there was no need to close the valve in the piston.

Burn-out and sintering procedure

After the infiltrated replica has been removed from the sandwich mould the polymer is removed by heat treatment. A tube furnace was used for the burn-out cycle as it allowed good control of the airflow needed to remove the carbonaceous char formed after degrading the polymer. An air flow rate of 1 L / min was used throughout the burn-out cycle. The burn-out procedure consisted of 5 hrs of temperature ramping and burnout of the polymer, followed by a further sintering of the NaCl (Figure 24). The

burn-out cycle utilised was suggested by the RP material manufacturer 3D Systems [68]. On to of the burn-out profile different sintering profiles were added for a continuous burn-out and sintering cycle.

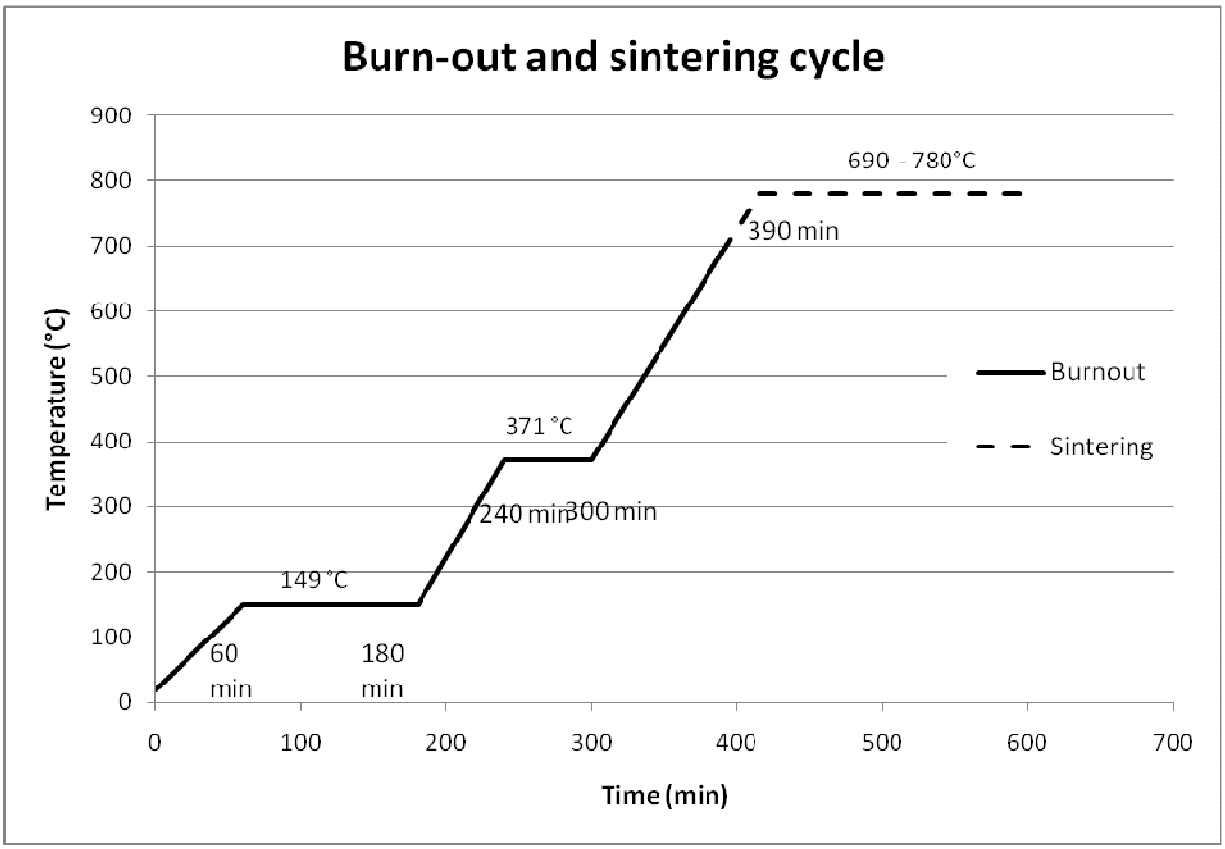

Figure 24: The burn-out and sintering temperature cycle.

Thermal Gravimetric Analysis (TGA)

The thermal decomposition characteristics of the polymer used in the RP scaffold, gelatine and non-sintered bulk NaCl were analysed using a TGA analyser. TGA is commonly used to determine the thermal and compositional characteristics of polymeric materials. For example, TGA allows the determination of the degradation temperature and moisture content. TGA consists of a high precision balance and electric heater to measure changes in the weight of a sample over a large temperature range. A Q600

TGA machine (TA instruments) was used to analyse the samples under a nitrogen or air atmosphere (Figure 25).

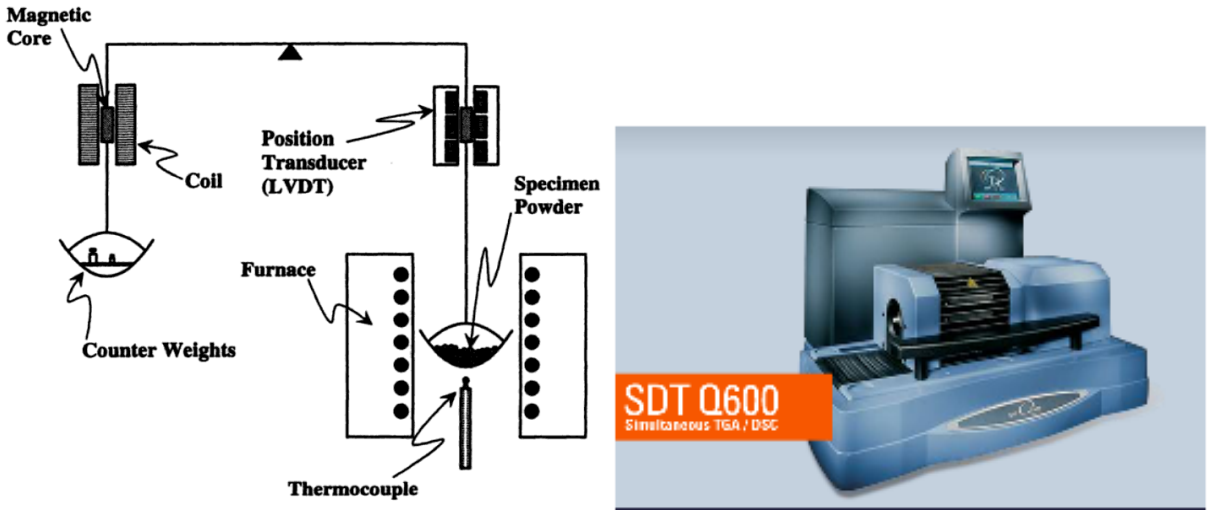

Figure 25: Example of TGA design were mass loss is measured using counter weight setup [69] as used in the TA Q600 thermal gravimetric analyser [70].

Casting of Mg foams

A low pressure die casting method was used to cast Mg into the NaCl template using a 10 kW vacuum induction furnace (Figure 26). The low pressure method is necessary to infuse the magnesium into the pores of the NaCl template due to the high surface tension of molten Mg. Trials with gravity casting were not successful for the above reason. NaCl templates were infiltrated with high purity (99.98%) liquid Mg under a high purity Argon (Ar) atmosphere (Grade 0) at 700°C. The infiltration pressure (P_i) was accurate to within ± 5 mbar. By applying vacuum to the furnace chamber after the metal is molten and then re-pressurizing the chamber, a pressure differential is generated that forces the Mg melt into the NaCl template. The Pourpaix diagram reveals that corrosion of magnesium ceases when the pH level is greater than 11.8. Thus, a NaOH solution with a slightly higher pH level than 11.8 was used to remove the NaCl from the Mg structure [71]. The crucible used in the casting was tapered so the metal could be removed without destroying the crucible, allowing it to be reused. A rod

in the middle of the crucible was used to prevent the sodium chloride template from floating to the surface of the melt.

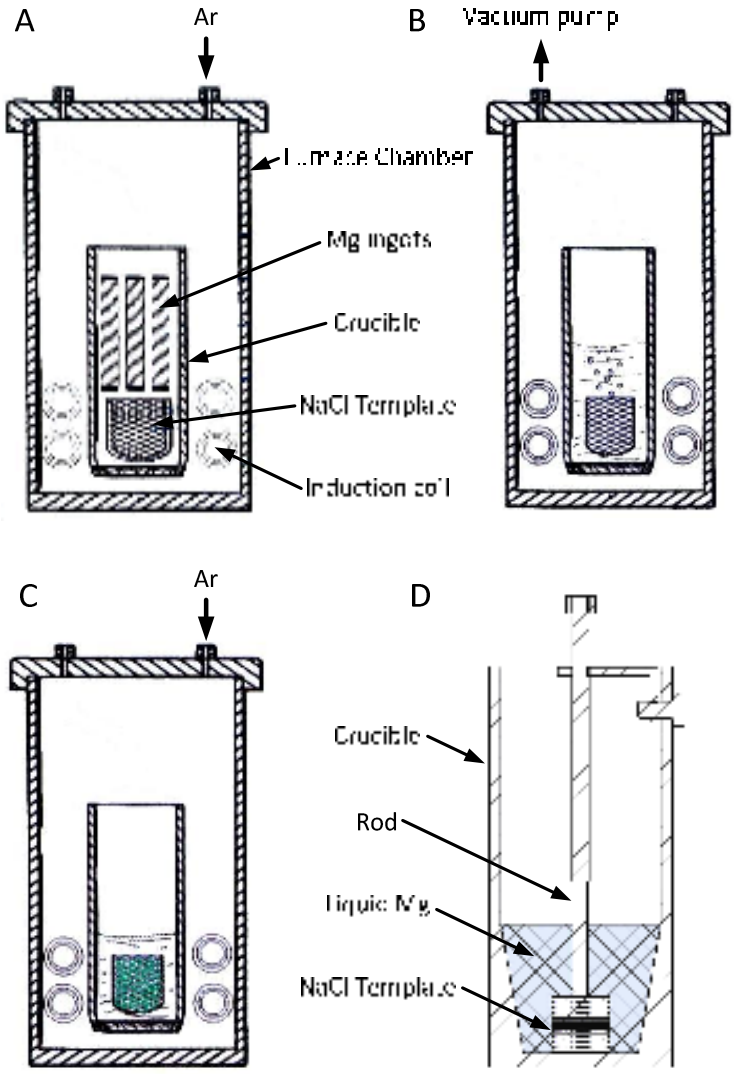

Figure 26: Schematic diagram of infiltration process using vacuum induction furnace: A) setting up for casting, B) evacuation step and C) Ar-pressurised infiltration. Also the D) crucible design setup.

3.2. Materials characterisation

The monolithic NaCl samples fabricated were sintered at temperatures of 650, 690, 715, 750 and 780°C. Non-sintered samples were fabricated and used as control samples for comparison. In general, a sintering time of 3 hrs was used except for samples sintered at 780°C that were sintered for 3 and 24 hrs for comparison.

3.2.1. Mechanical testing

The compressive properties of the bulk NaCl structure were tested in static mode using an MTS 810 Material Test System at a constant cross-head speed of 1 mm/min. The compressive strength, modulus and fracture energy of the material was determined. Samples were tested between flat platens and loads were measured with a 10 kN load cell (Figure 27). Aluminium foil was put under the samples to avoid NaCl fragments falling into the machine.

Compression samples were prepared by first dry grinding to remove the filter paper. Samples were then dry-polished on emery paper with a final polish using P400 paper. Samples were carefully polished to obtain smooth and parallel top and bottom surfaces. The dimensions of each sample were measured using a digital sliding calliper and weight was measured to allow calculation of the density, stress and strain.

Figure 27: Compression testing of a bulk NaCl sample.

The materials properties were calculated using the following equations:

Density (ρ) $$\rho = \frac{m4}{d^2\pi}$$ (3.1)

Compression stress (σ) $$\sigma = \frac{F4}{d^2\pi}$$ (3.2)

Compression strain (ε) $$\varepsilon = \frac{\Delta L}{L}$$ (3.3)

Fracture energy (U) $$U = \int_0^x F\ dx$$ (3.4)

$$U = \int_0^x C1 * x^6 + C2 * x^5 + C3 * x^4 + C4 * x^3 + C5 * x^2 + C6 * x + b \; dx$$

$$U = \frac{C1 * x^7}{7} + \frac{C2 * x^6}{6} + \frac{C3 * x^5}{5} + \frac{C4 * x^4}{4} + \frac{C5 * x^3}{3} + \frac{C6 * x^2}{2} + b * x$$

where, ρ = density of the sodium chloride particles (g/cm^3)
σ = stress in the structure (MPa)
ε = strain in the structure
U = energy at the yield point (J)
m = weight of the sample (g)
d = diameter of the sample, mm (~20 mm)
F = load at a given point on the load-deformation curve (N)
ΔL = change in height of the sample on the load-deformation curve (mm)
L = total length of sample (mm)
x = fracture deforming length (mm)

The measured compression stress-strain curves were fitted to 6th order polynomial function for easier data processing. The elastic modulus was measured at the start of the stress-strain curve it has its highest value. All the samples had there maximum modulus at the start of the curve. An example of a typical stress-strain curve is shown in Figure 28, along with determination of the 1% proof or yield stress.

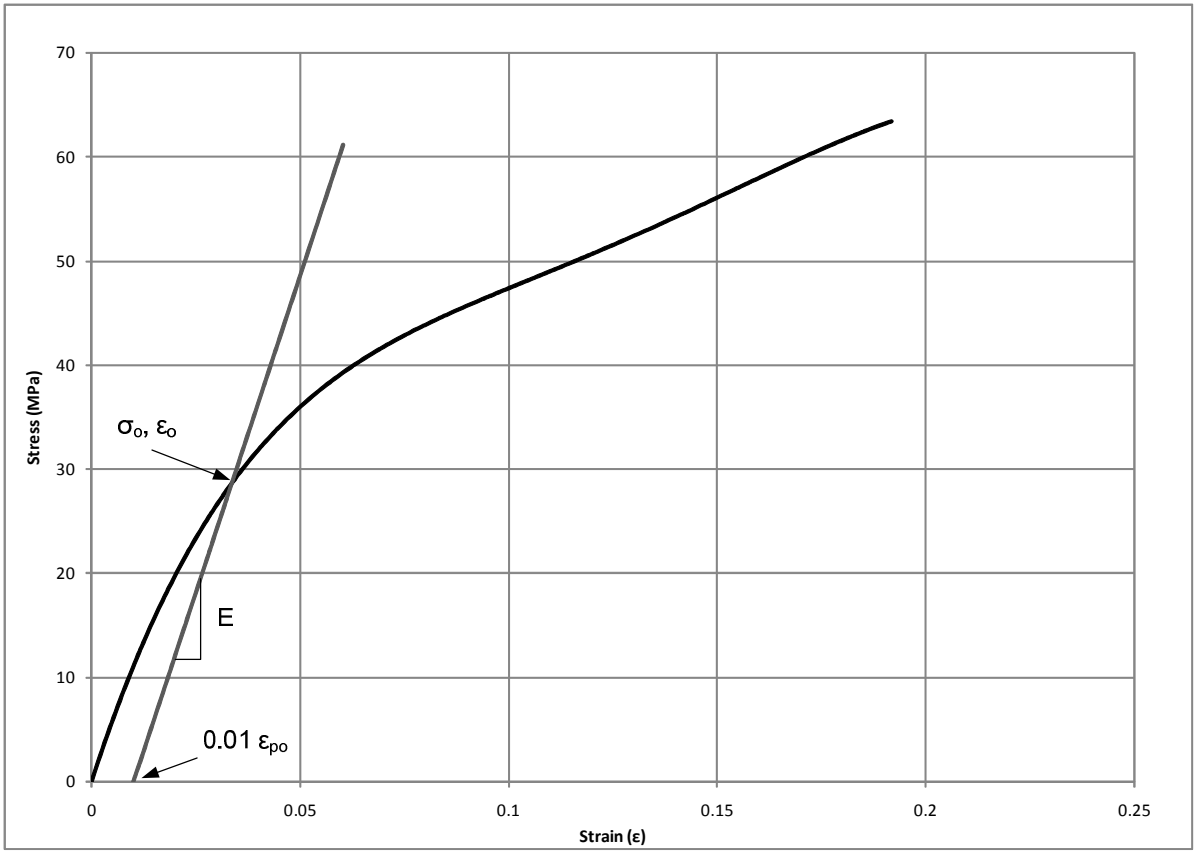

Figure 28: Typical compressive stress-strain behaviour of a bulk NaCl sample.

Compressive tests of selected Mg samples were carried out at an initial strain rate of 10^{-3} s^{-1} (MTS® 810, 100 kN load cell) on miniature samples with a depth × width × height of 5 × 5 × 7 mm based on sample preparation guidelines in ASTM E9-89a [72]. Following the methods of Ashby [73], the maximum stress value for the cellular Mg was taken from the first stress peak that appeared. The compressive strength of selected cellular Mg samples were compared to bulk Mg by testing samples of equivalent cross sectional areas, which, in the case of the foams, was simply determined as the area of the vertical columns.

3.2.2. X-ray microtomography (μ-CT)

A SkyScan 1172 X-ray microtomography (μ-CT) unit (Centre of Microscopy, Otago University) was used for visually examining the internal microstructure of the NaCl templates (Figure 29). μ-CT is based on determination of density differences that allows visualisation of multiphase microstructures through differences in contrast. μ-CT involves taking a number of X-ray scans through the sample to produce a series of 2-D images that represent the cross section of the sample. Using the images obtained by μ-CT, NRecon (SkyScan software) produces computer-generated parallel slices of the sample cross-section using a constant step size between slices throughout the height of the sample. The images generated by μ-CT are taken from the side of the sample whilst the sample is rotated; therefore, images are not parallel to each other but rather consecutive images are related to each other through a fixed angle of rotation. The picture format was converted from Tagged Image File (TIF) to Bitmap (BMP) format. The greyscale of the X-ray images was adjusted to enhance the contrast between the NaCl and polymer. The 2-D images are then reconstructed into a 3-D computer-generated model.

Materialise Mimics software was used for the 3-D reconstruction. The cross-sectional images of the part were manually imported into the software where CT compression was chosen. A 3-D computer-generated model was constructed by manually thresholding the images and designating the 3 orthogonal planes or directions of the part. Image analysis was used to examine volume fractions in the 2-D slices and 3-D reconstructions. ImageJ software was used to visually examine the structure for manufacturing defects using the 2-D figures. ImageJ was also used to measure the pore fraction of each cross-sectional slice to give plots of the porosity as a function of the sample height. This was performed by using an import image sequence function in the software in which all of the cross-sectional slices were batch processed. Batch processing involved first thresholding and cropping of images and then a plug-in was used to analyse the image stack [74].

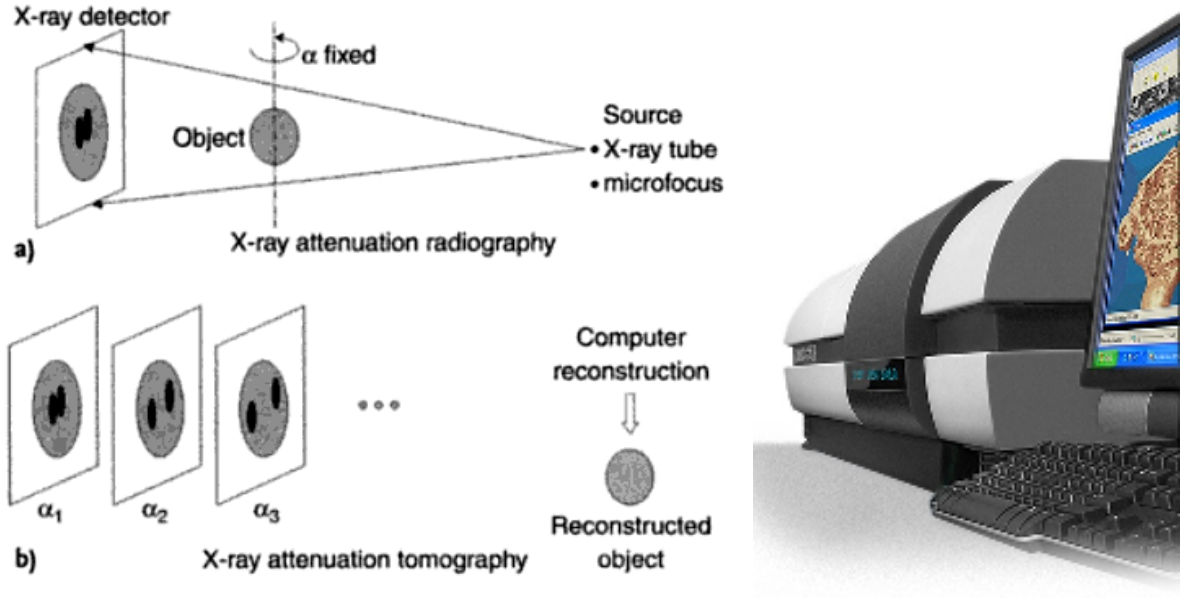

Figure 29: Schematic of the X-ray tomography principles, a) X-ray radiography, b) X-ray tomography processing [75] and SkyScan 1172, high-resolution µCT unit utilised.

3.2.3. Scanning electron microscopy (SEM)

The microstructure of the sodium chloride samples was analysed by field emission scanning electron microscopy (FE-SEM) (JOEL JSM-6100) using 3 kV accelerating voltage. The NaCl samples were prepared for FE-SEM by adhering to a standard holder using carbon tape under and along the side of the sample before gold coating. Sample surfaces were gold coated using a Polaron Specimen Coating Unit (E5100 Series II Cool Sputter) at 1.2 kV. Samples were coated twice for 3 min. Samples were placed under the coater head at a 45° angle and rotated by 180° for the second coating to get sufficient coverage between grains. The sputter current was set to 3.5 mA at a distance of 30 mm. The pressure inside the chamber was set to 0.2 Bar using Ar as a shield gas. All NaCl samples were stored in an oven at 50°C prior to FE-SEM preparation and then stored in a desiccator after FE-SEM preparation to prevent moisture absorption.

3.2.4. Electron backscattered diffraction (EBSD)

EBSD is a useful technique that is used in conjunction with SEM to provide crystallographic information. EBSD is useful for determination of phases, grain size and grain morphology. Samples prepared for EBSD require highly polished and parallel, flat surfaces. Parallel surfaces are important to allow accurate tilting of the sample surface in the SEM. Sample is placed under a 70° angle in the SEM (20° angle to the incident electron beam). When the electron beam hits the surface and interacts with the crystal lattice, low energy loss backscattered electrons that reverberate are collected and patterns can be seen (Figure 30). By moving the sample (in steps) while scanning, EBSD maps can be created for an area of the sample surface for crystallographic analysing.

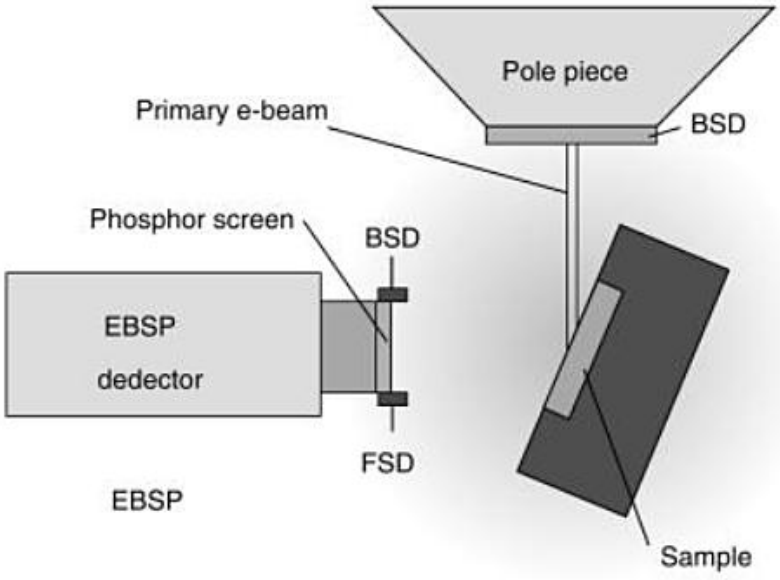

Figure 30: Schematic of the sample arrangement in the SEM and the back-scatter pattern (EBSP) detector [76].

Initially, it was hypothesised that porosity in the NaCl samples could be eliminated by using a conductive resin to prevent charging during EBSD and also allow the use of $FeCl_3$ for removal of scratches. However, conductive resins typically have high

viscosities that make infiltration into fine surface pores difficult. Non-conductive resins have low viscosity but require a conductive coating of Au, Pt or C that then interferes with the acquisition of EBSD patterns. The as-received porous NaCl was polished using a new approach developed that produced high quality surfaces for EBSD without the need for etching.

NaCl were first mounted in cold-curing polyester resin. Vacuum impregnation was not used, to avoid infiltration of surface pores. This approach minimised charging. The mounted samples were ground in white spirits on 400 and 600 grit carborundum papers The first stage of polishing involved a non-aqueous 1 μm diamond paste (Buehler) on Mettex cloth (Mark V) for 3.5 min. The final polish was carried out with a thick paste mixture of 0.05 μm alumina powder (Beuhler Micropolish II) and high purity white spirits. The samples were hand-polished for 6-8 min on a velvet cloth (Selvyt; Mark V) carefully maintaining a thick layer of paste between the cloth and sample at all times. After the final polish, the surface was washed with white spirits and tissues, and then wiped on a velvet cloth soaked in high purity white spirits. Finally the dried pellets were wiped gently on a dry velvet cloth to remove surface residues. Samples were cleaned for 30 min in analytical grade petroleum spirit (LabServ^{TM}) using an ultrasonic cleaner; this was repeated 5 times each time the cleaner was replaced with fresh petroleum. The surface was then checked for any residue (*e.g.* polishing particles, *etc.*) using optical microscopy. Any observed residue was removed by wiping with a wet velvet cloth using high purity petroleum. Samples were then stored in a desiccator before EBSD analysis.

OIM was carried out using an HKL Electron Backscattered Detector (EBSD) system fitted on JEOL JSM6100 Scanning Electron Microscope (SEM). Uncoated NaCl samples were analysed with 12 kV accelerating voltage. OIM was carried out with a step size of 1 μm, 4 × 4 binning, #2 frames and exposure time of ~150 ms. Mean angular deviation (MAD) between the detected kikuchi bands and the simulation was set to $\leq$ 1.3°. Samples were left for ~1 hr to allow stabilisation of the beam before taking any measurements. A minimum grain misorientation of 15° was used to define primary GBs [77]. To eliminate small errors that were found on the maps grains less than 5.7 μm

were ignored when measuring the grain dimensions. The 5.7 μm equals to 4 x 4 pixels square when using the 1 μm step size.

4. Processing and properties of bulk polycrystalline NaCl

4.1. Introduction

A significant challenge is in fully infiltrating the RP polymer scaffold with NaCl to produce a strong structure that retains mechanically stability once the polymer is burnt off. Firstly different experiments that were carried out using an aqueous paste solution are described in this chapter. The NaCl is transferred into the RP scaffolds in paste form, resulting in fully infiltrated and dry template structure. Bulk polycrystalline NaCl samples are prepared to analyse sintering effects in the range of 650-780°C on the NaCl properties compared to the non-sintered. In the second part of the chapter a novel preparation technique, that makes possible grain size analysis of polycrystalline NaCl using orientation imaging microscopy *via* electron backscatter diffraction (EBSD), is developed. The grain size and crystallographic texture of polycrystalline NaCl were able to be measured successfully with EBSD. The limitations of the preparation technique for EBSD analysis of NaCl are also discussed. Thirdly compression testing of the sintered as well as the non-sintered bulk NaCl is used to measure its mechanical properties, *i.e.* strength and modulus. Next the fracture behaviour of the bulk NaCl samples are analysed in the SEM. Finally the results of the previous are discussed in the last part of chapter 4.

4.2. Formulation of NaCl infiltration paste

Initially, different experiments were carried out using an aqueous paste solution whereby the sodium chloride is transferred to the scaffold in the form of small grains. The effect of various additions to the NaCl paste on infiltration of a scaffold was investigated through trial and error (Table 2). Initially, a simple piston and cylinder in a small hydraulic press was used to infiltrate a 1 x 1 mm lattice scaffold with the paste. By adjusting the quantity of gelatin and supersaturated NaCl solution mixed with the NaCl powder, the extent of infiltration was evaluated visually. In the second stage of the development a clamp that was fitted with load cell was used to measure the applied infiltration force. Many modifications of the equipment and materials were implemented

throughout this process and some of these are summarised in Table 2. The final stage of the development of the process involved designing a fully functional infiltration device and a press unit fitted with a pneumatic cylinder. A precise pressure regulator was used to be able control the infiltration pressure with high accuracy.

Table 2 List of experiments carried out to evaluate the most effective way to fabricate the sodium chloride template.

Legend:

- Pressed with clamp with load cell
- Pressed with pneumatic cylinder
- Pressed in hydraulic press
- R5 material
- PIC 100 material
- Solidscape material
- InVision material
- NaCl dry after drying process
- NaCl moisturized after drying process
- NaCl wet after drying process
- Able to fill scaffold with paste
- Not able to fill scaffold with paste

Nr.	Scaffold dry weight (g)	Scaffold Height (mm)	Paste (ml)	Scaffold weight (g)	NaCl porosity (%)	Infiltration pressure (N)	Drying time (Hours)
1	3.897						
2	NA						
3	3.960			7.336	50%		
4	3.934						
5	3.939						
6	3.464						
7	NA						
8	3.960			7.033	46%		
9	3.480						
10	3.903		7			500-2000	
11	NA		7			500-2000	
12	3.966		7			500-2000	
13	3.482		7			30	
14	NA		7				
15	NA		7				
16	3.939		7	7.016	46%	No cell	23
17	3.940		7			No cell	23
18	3.848		7	6.848	45%	No cell	23
19	3.953		7	7.190	48%	No cell	23
20	3.490		8	6.540	45%	No cell	19
21	3.478		8			No cell	48
22	3.295		8			No cell	48
23	3.885	18.45	8	7.011	57%	160	24
24	3.793	18.82	8	6.982	54%	160	24
25	3.897		8.2			310	22
26	3.956	18.70	8.2	6.911	53%	310	22
27	3.881	17.70	8.2	6.765	58%	470	22
28	3.791		8.2			470	22
29	3.872		8.2			620	22
30	3.861		8.2			620	22
31	3.793	18.92	8.5	7.062	55%	0	20
32	3.787	18.50	8.5	7.158	59%	0	20
33	3.856	18.35	8.5	7.368	64%	310	18
34	3.783		8.5			3.5 Mpa	18
35	4.310		8.5			3.5 Mpa	22
36	3.739					3.5 Mpa	22
37	3.576					3.5 Mpa	22
38	3.547					3.5 Mpa	22
39	3.537					3.5 Mpa	22

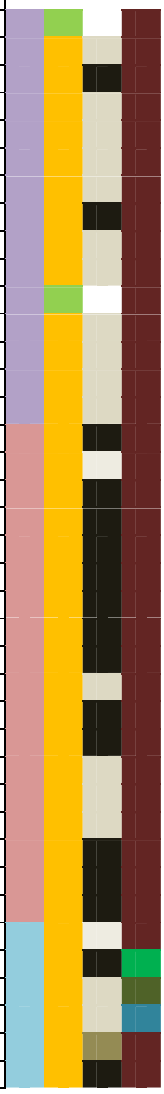

40	NA					2.0 Mpa	22	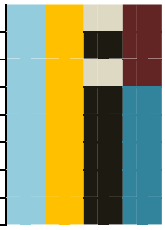
41	NA					2.0 Mpa	22	
42	NA					2.0 Mpa	22	
43	NA					2.0 Mpa	22	
44	NA					2.0 Mpa	22	
45	NA					2.0 Mpa	22	
46	NA					2.0 Mpa	22	
47	NA					2.0 Mpa	22	

A series of monolithic NaCl samples were also studied to better understand the effect of sintering on the NaCl structure. The effect of sintering conditions on NaCl properties were examined by analysing the fracture surfaces, compression properties and grain structure. The bulk samples of NaCl were fabricated in the infiltration unit using the same method as for the porous NaCl, except that the RP polymer scaffold was omitted from the process. As no RP scaffold was used in the monolithic process, there was no need to close the valve in the cylinder while compressing the NaCl paste. Failures were experienced in the fabrication of bulk samples as the paste did not dry uniformly. It was found that the paste dried more uniformly by increasing the gelatin content. It was found that increasing the infiltration pressure to 7 MPa resulted in structure with higher density. But because of large deformation on the RP scaffolds when infiltrated using 7 MPa it was decided to go for lower infiltration pressure. A series of samples were prepared with a moulding pressure 3.5 MPa, but with different sintering conditions: non-sintered, sintering at 650, 690, 715, 750 or 780°C for 3 hrs, and sintering at 780°C for 24 hrs. The density of the samples did not change after sintering, except after sintering at 780°C for 24 hrs. However, this latter sample non-uniformly shrank in volume, making it difficult to accurately measure the density after sintering.

A list of the fabricated bulk samples along with the dimensions and sintering conditions are shown in Table 3.

Table 3: A summary of the experimental samples produced and conditions used during fabrication.

Sample Nr.	Paste			Sintering		Infiltration pressure (MPa)	Sample Measurements				Density (%)	
	NaCl (wt %)	NaCl water (wt %)	Gelatin (wt %)	Temp (°C)			Sample height (mm)		Sample weight (g)			
				Nr. 1	Nr. 2		Nr.1	Nr.2	Nr.1	Nr.2	Nr.1	Nr.2
1	73.2%	19.5%	7.3%	690	690	3.5	13.83	12.48	8.133	7.439	84.8%	86.0%
2	73.2%	19.5%	7.3%	NA	737	3.5	NA	NA	NA	NA	NA	NA
3	73.2%	19.5%	7.3%	747	747	3.5	11.63	10.65	6.857	6.383	85.0%	86.4%
4	73.2%	19.5%	7.3%	716	716	3.5	11.42	11.12	6.665	6.315	84.2%	81.9%
5	73.2%	19.5%	7.3%	692	692	3.5	10.98	8.10	6.417	4.572	84.3%	81.4%
6	73.2%	19.5%	7.3%	647	647	3.5	10.37	10.43	6.104	6.030	84.9%	83.4%
7	73.2%	19.5%	7.3%	752	752	3.5	11.20	9.43	6.773	5.756	87.2%	88.0%
8	73.2%	19.5%	7.3%	705	705	7	11.52	12.41	6.976	7.425	87.3%	86.3%
9	73.2%	19.5%	7.3%	NA	NA	7	NA	NA	NA	NA	NA	NA
10	73.2%	19.5%	7.3%	715	715	7	10.87	10.57	6.383	6.234	84.7%	85.1%
11	73.2%	19.5%	7.3%	715	NA	2	13.15	NA	7.325	NA	80.3%	NA
12	73.2%	19.5%	7.3%	715	NA	2	9.15	6.95	4.662	3.938	73.5%	81.7%
13	71.8%	18.6%	9.6%	650	750	3.5	12.88	NA	7.744	NA	86.7%	NA
14	71.8%	18.6%	9.6%	NA	NA	3.5	NA	NA	NA	NA	NA	NA
15	73.0%	18.9%	8.1%	NA	NA	3.5	NA	NA	NA	NA	NA	NA
16	73.2%	19.5%	7.3%	690	NA	3.5	13.32	NA	7.492	NA	81.1%	NA
17	73.2%	19.5%	7.3%	NA	NA	3.5	NA	NA	NA	NA	NA	NA
18	73.0%	18.9%	8.1%	715	715	3.5	9.63	9.61	5.063	5.173	75.8%	77.6%
19	73.0%	18.9%	8.1%	780	780	3.5	10.91	12.05	6.162	6.634	81.5%	79.4%
20	73.0%	18.9%	8.1%	780	750	3.5	11.69	10.69	6.530	5.971	80.6%	80.6%
21	73.0%	18.9%	8.1%	715	NA	2	11.41	NA	6.299	NA	79.6%	NA
22	73.0%	18.9%	8.1%	715	NA	1	10.86	NA	5.400	NA	71.7%	NA
23	73.0%	18.9%	8.1%	NA	NA	1	NA	NA	NA	NA	NA	NA
24	73.0%	18.9%	8.1%	650	NA	3.5	9.50	NA	4.974	NA	75.5%	NA
25	73.0%	18.9%	8.1%	0	0	3.5	11.12	9.40	6.500	5.517	84.3%	84.6%
26	73.0%	18.9%	8.1%	0	0	3.5	10.97	10.90	6.480	6.460	85.2%	85.5%
27	73.0%	18.9%	8.1%	650	650	3.5	10.54	10.59	5.760	5.733	78.8%	78.1%
28	73.0%	18.9%	8.1%	715	715	≈ 2.3		NA		NA		NA
29	73.0%	18.9%	8.1%	780	780	3.5	10.20	7.96	5.408	4.322	76.5%	78.3%
30	73.0%	18.9%	8.1%	780	690	3.5	8.60	8.20	4.966	5.075	83.3%	89.3%
31	73.0%	18.9%	8.1%	715	715	3.5	13.13	13.67	7.179	7.308	78.9%	77.1%
32	73.0%	18.9%	8.1%	650	0	3.5	10.43	11.56	NA	NA	NA	NA
33	73.0%	18.9%	8.1%	NA	NA	3.5	NA	NA	NA	NA	NA	NA
34	73.0%	18.9%	8.1%	715	NA	1	7.99	NA	4.587	NA	82.8%	NA
35	73.0%	18.9%	8.1%	780	NA	3.5	11.78	NA	6.723	NA	82.3%	NA
36	73.0%	18.9%	8.1%	780	NA	3.5	9.54	NA	5.323	NA	80.5%	NA
37	73.0%	18.9%	8.1%	780	NA	3.5	9.12	NA	5.360	NA	84.8%	NA
38	73.0%	18.9%	8.1%	650	0	3.5	9.75	10.20	5.638	5.926	83.4%	83.8%
39	73.0%	18.9%	8.1%	NA	NA	1	NA	NA	NA	NA	NA	NA
40	73.0%	18.9%	8.1%	715	715	1	11.98	11.88	7.036	7.061	84.7%	85.7%
41	73.0%	18.9%	8.1%	715	715	7	11.05	10.31	6.626	6.245	86.5%	87.4%

4.3. Microstructural analysis of sintered and non-sintered polycrystalline NaCl

Over the last decade, orientation imaging microscopy (OIM), through automated electron backscatter diffraction (EBSD), has become a useful quantitative tool for grain size and microtexture determination, as well as studying phase transformations and grain boundary (GB) misorientation of metallic, and to a lesser extent, ceramic materials [78, 79]. During EBSD, Kikuchi diffraction bands are observed when the Bragg diffraction condition is satisfied, and their location and spatial orientation is then used to determine the crystal structure and crystal orientation [80]. EBSD is capable of spatial resolutions of ~10 nm and detecting grain misorientations as small as 0.5°, making it a fast and accurate method of grain size determination compared with traditional methods [81].

The characterisation and measurement of grain and subgrain structures is important since the grain size strongly affects, for example, thermomechanical properties, phase transformations and sintering behaviour of polycrystalline materials. The grain size is commonly determined with optical or scanning electron microscopy, although these techniques rely on having clearly discernable GBs, usually delineated by chemical etching. In contrast, EBSD is well suited to the analysis of polycrystalline materials in which it is difficult to distinguish GBs since EBSD is able to locate GBs from the misorientation between adjacent grains.

NaCl has long been useful as a model material for studying the sintering and creep behaviour of ceramics [82-87]. More recently, pure NaCl has been used by geologists, again as a model material, to study the phenomenon of creep in rock salt (and other minerals in the earth's crust) that operates *via* the dislocation creep and/or pressure solution mechanisms [88]. Pressure solution involves GB sliding and dissolution-precipitation of material that will in turn be dependent on grain size. In the latter mechanism, NaCl is dissolved in the presence of a thin layer of liquid at the GBs and under an applied pressure diffuses along GBs, precipitating again in regions of lower

stress [89]. The rheological constitutive laws of creep driven by pressure solution are still poorly understood.

OIM has been used to measure the grain size and crystallographic texture of fully-dense polycrystalline NaCl [88, 90, 91]. Before EBSD analysis, NaCl polished surfaces are typically etched using a slightly unsaturated salt solution containing ferric chloride ($FeCl_3$) to remove scratches and reveal grain and subgrain boundaries [92]. $FeCl_3$ is removed with a solvent that removes only a thin layer of NaCl from the polished surface (*e.g.* ethanol). However, the complete removal of $FeCl_3$ is difficult if the surface of polycrystalline NaCl contains pores. It has been observed by the authors that $FeCl_3$ deposits on the inside of micropores and is virtually impossible to remove with solvents without excessive removal of NaCl, inadvertently changing the original microstructure. Thus, the use of EBSD for measuring the grain size of sintered NaCl remains problematic in samples that contain micropores after sintering. Moreover, it is recognised in the wider literature that further development of preparation techniques is necessary for the improved characterization of GB misorientation in polycrystalline NaCl with EBSD [91].

4.3.1. Orientation imaging microscopy of polycrystalline NaCl

Polished surface of the samples showed a good observation of Kikuchi patterns in the EBSD with a mean angular deviation (MAD) ranging between 0.51±0.18° and 0.59±0.17°. MAD is a goodness fit of the solution. The smaller the number is the better the match between the detected Kikuchi bands and the simulation. An example of selected area electron diffraction Kikuchi pattern, presented in Figure 31, shows a good pattern observation.

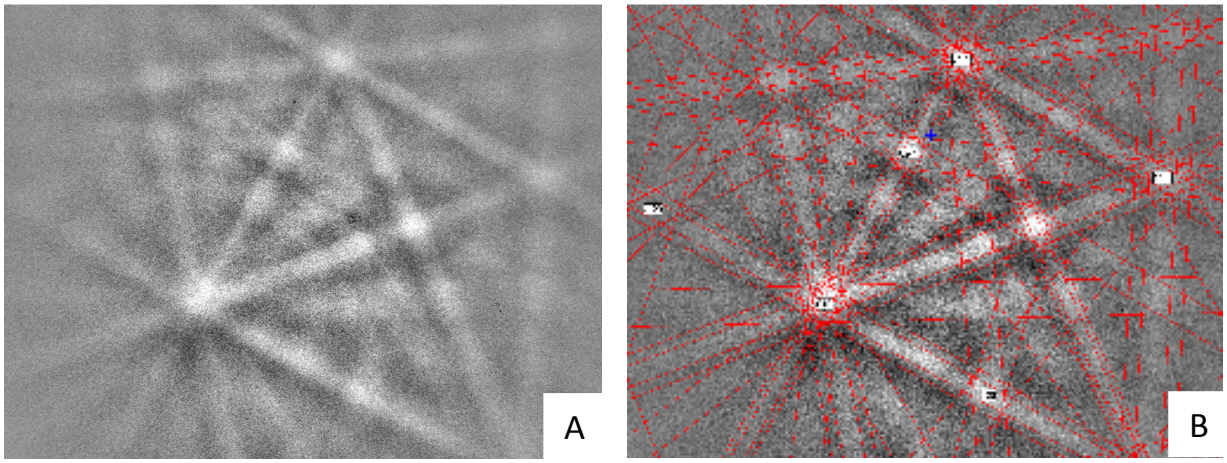

Figure 31: (A) A typical EBSD pattern for NaCl and (B) the corresponding indexing of the same pattern.

4.4. Influence of sintering on the density and microstructure of NaCl

Only small changes in the average grain size were evident with the sintering of the NaCl compacts for all of the temperatures with a sintering time of 3 hrs. For the sake of brevity, only selected orientation maps of polycrystalline NaCl showing representative microstructures are presented for comparison in Figure 32. Significant grain growth took place when sintered for 24 hours at 780°C as shown in Figure 32D (note different magnification). All of the samples were scanned at 300x magnification, except the 24 hour sintered sample where a lower magnification (150x) was used to capture more grains for better average results. It was also found that going to higher magnification than utilised resulted in more charging on the sample surface, so picking up patterns did get more difficult and this would not generate maps with good quality. The average grain size of the NaCl compacts increased by around 14% after sintering at 715-780°C for 3 hrs (Figure 33). The average grain size of the NaCl compacts (~20 μm) increased dramatically by ~450% (99.5 ± 53.8 μm) after sintering at 780°C for 24 hrs (Figure 33).

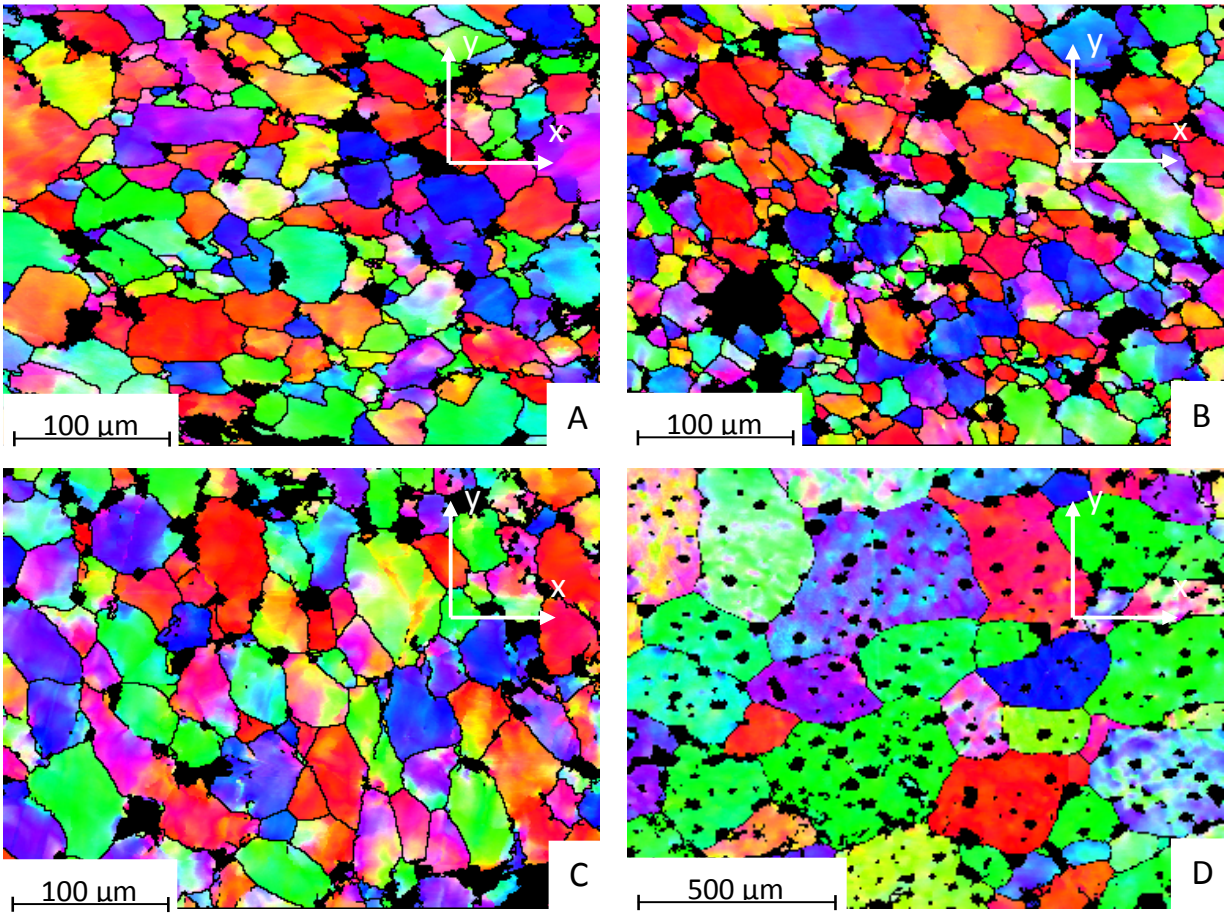

Figure 32: Orientation maps showing only the high angle grain boundaries (>15°) and grains with Euler contrast of grain growth in the NaCl for (A) non-sintered NaCl and different sintering conditions, two sintered for three hours at different temperatures, (B) 650, (C) 780 and (D) sintered for 24 hours at 780°C.

Sintering of polycrystalline NaCl at 650°C for 3 hrs (Figure 34B) resulted in an unexpected increased appearance of fine grains ≤20 µm, when compared to the non-sintered NaCl (Figure 34A) – which is also reflected by a slight decrease in average grain size (Figure 33).

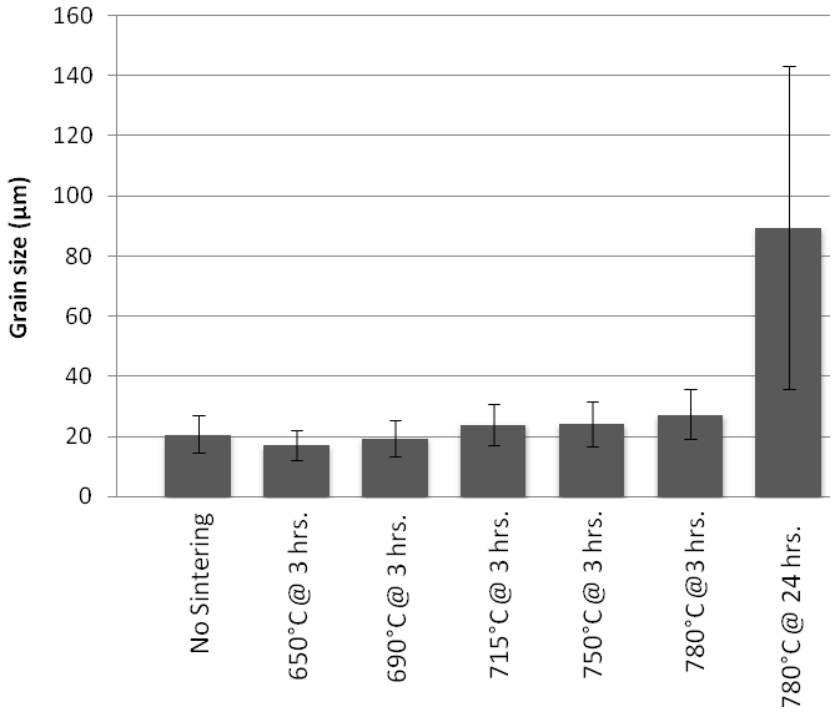

Figure 33: Graph showing the average grain size with standard deviation.

In general, the grain size distribution shifted toward larger grain sizes as the sintering temperature was increased from 650°C (Figure 34B) to 780°C (Figure 34C). A bimodal population of small grains (<20 μm) and large grains (>200 μm) develops with an increase in sintering time from 3 hrs (Figure 34C) to 24 hrs (Figure 34D) at 780°C. Extensive grain growth at 780°C for 24 hrs also leads to trapping of pores within the NaCl grains, which makes further densification difficult with extended sintering times.

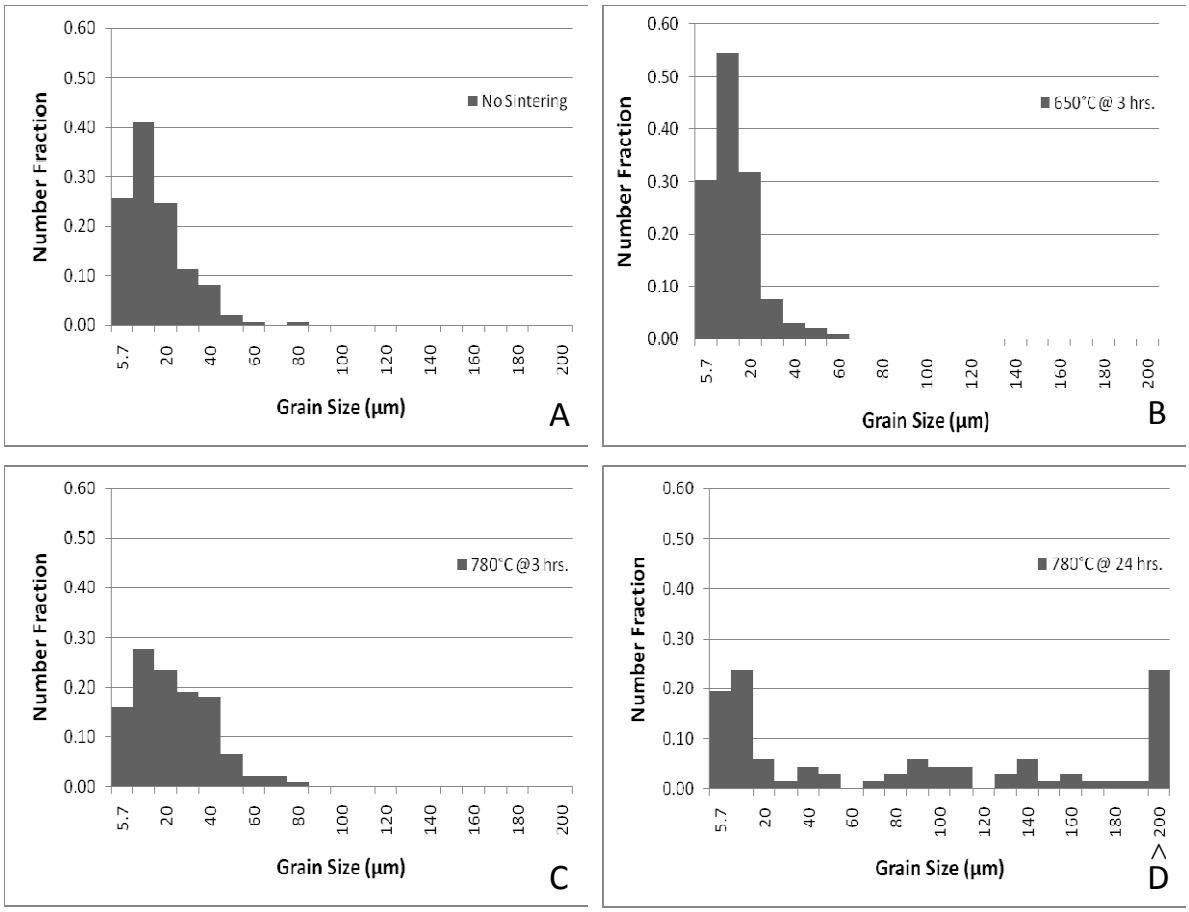

Figure 34: Grain size distributions for (A) non-sintered and three samples sintered at, (B) 650, (C) 780°C for three hours and (D) 780°C for 24 hours.

Misorientation angle distribution plots for polycrystalline NaCl were generated over the range of 0 to 60° (Figure 35). It was found that in general low-angle subgrain misorientations dominated the misorientation angle distribution. Thus, the low angle misorientations (<10°) were excluded from the correlated distribution so that comparison of the high angle misorientations could be made. The misorientation angle distribution of samples sintered for 3 hrs showed decreasing goodness of fit with a random (Mackenzie) distribution as the sintering temperature was increased. In contrast, samples sintered for 24 hrs showed an increased goodness of fit to the random distribution (Figure 35C). Grains that have no bulk lattice preferred orientation (texture) or theoretically random juxtaposition would have a random (Mackenzie)

distribution of misorientation. Correlated misorientation measures misorientation of neighbouring pixels, whereas uncorrelated misorientation measures pixel misorientation of randomly chosen points on the EBSD map.

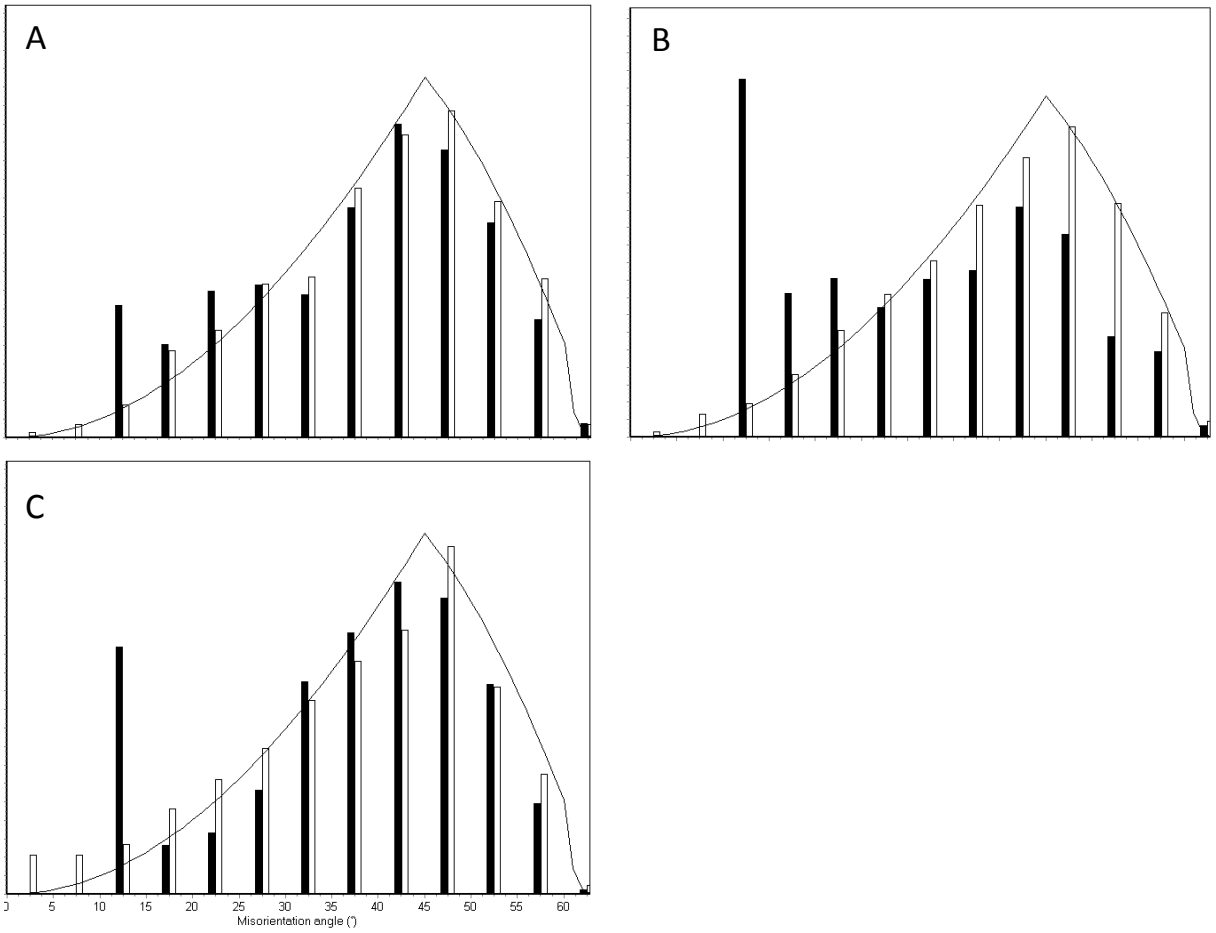

Figure 35: High angle misorientation distributions in (A) not sintered, sintered for three hours at (B) 780°C and (C) sintered for 24 hours at 780°C. Misorientations are grouped into 5° bins and low angle disorientations <10° are excluded. Neighbouring pixels (correlated) are shown as black bars, arbitrary selected pixels (uncorrelated) as white bars and theoretical random (Mackenzie) distribution is shown as line.

An analysis of the crystallographic texture using EBSD analysis was in agreement with the misorientation angle distributions showing no indication of preferred texture in polycrystalline NaCl for the conditions examined (Figure 36). The higher orientation

intensities measured for the sample sintered at 780 for 24 hrs was likely due to a relatively low number of large NaCl grains dominating the texture (Figure 36G).

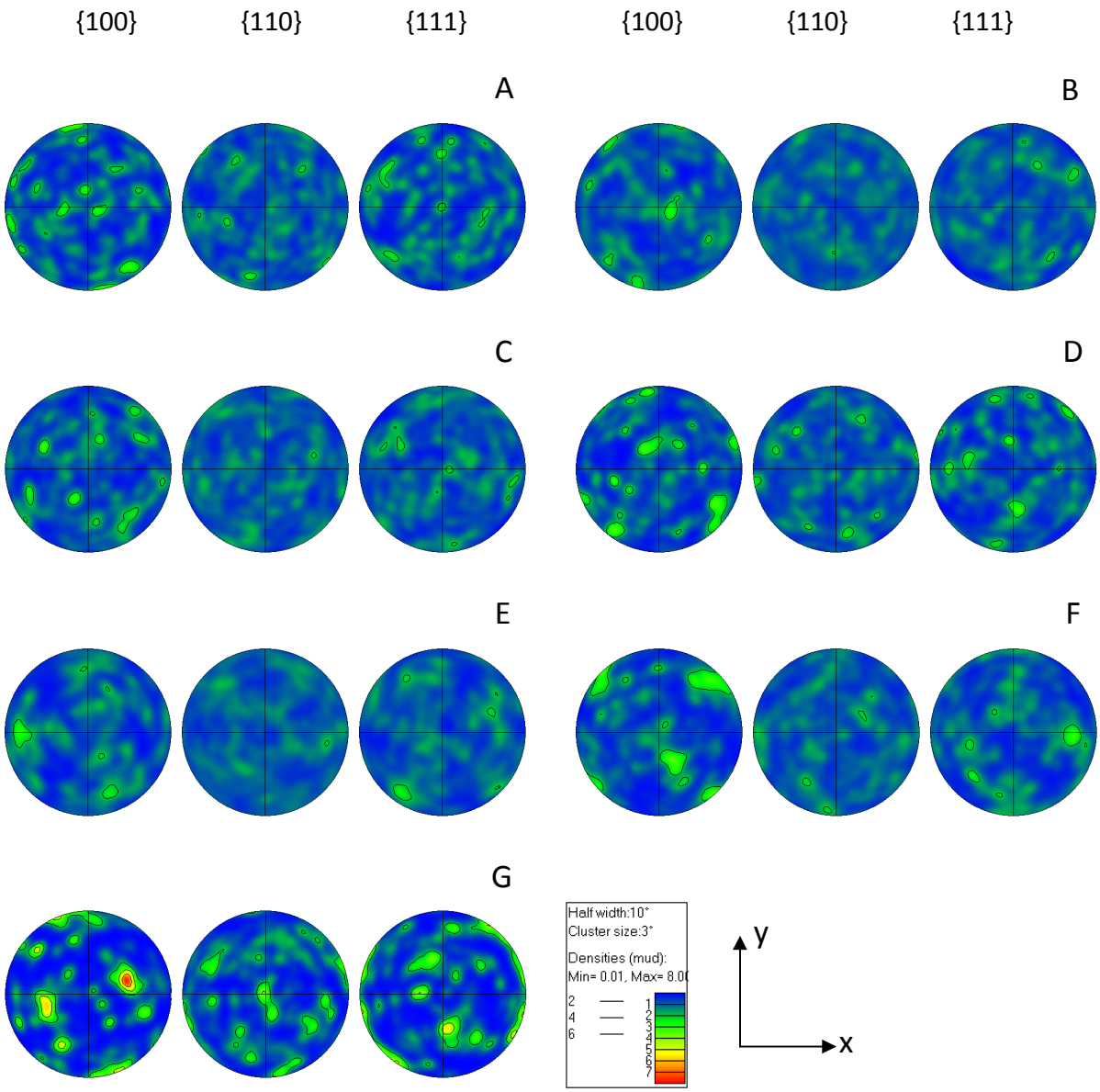

Figure 36: Pole figures {100}, {110} and {111} of (A) not sintered, five sintered for three hours, (B) 650, (C) 690, (D) 715, (E) 750, (F) 780 and (G) sintered for 24 hours at 780°C samples.

4.5. Compressive properties of NaCl

The NaCl compressive properties were measured as described in Chapter 3.2.1. The influence of sintering time and temperature on the strength and stiffness of bulk NaCl is illustrated in Figure 37 and Figure 38. The highest compressive strength of σ_y = 44.4 MPa was achieved by sintering at 690°C for 3 hrs. Sintering at 780°C for 24 hrs resulted in the second highest strength in this series. Interestingly, the non-sintered sample yielded higher strengths than some of the sintered samples. Sintering of NaCl at 650°C for 3 hrs resulted in the lowest compressive strength ~25 MPa. The samples tested had an average initial density of 82.4 ± 1.93% after sintering.

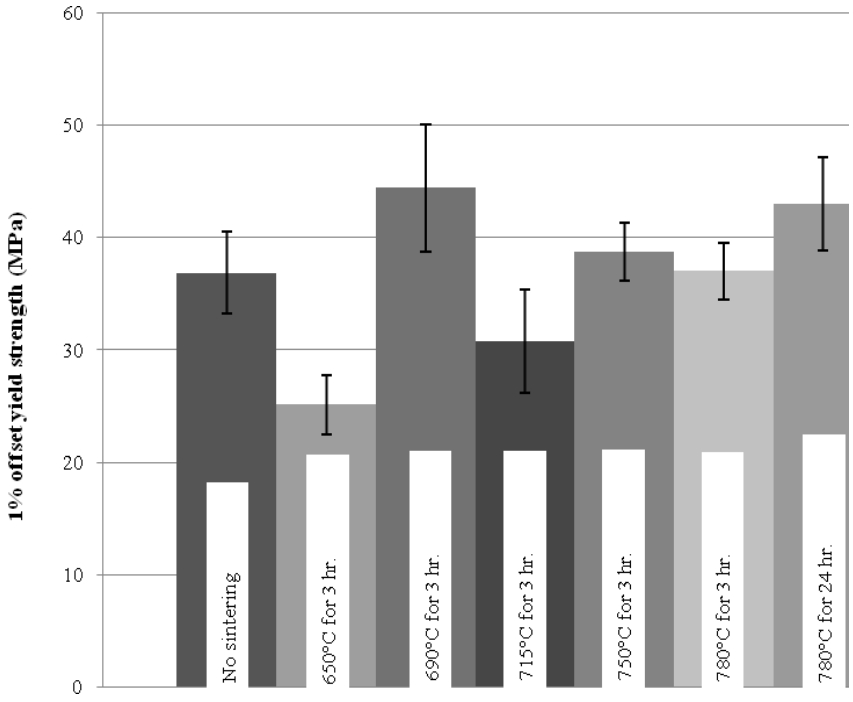

Figure 37: The compressive yield strength of polycrystalline NaCl as a function of the sintering conditions.

Sintering at 715°C for 3 hrs produced the lowest modulus while non-sintered had the highest modulus value. In contrast, the non-sintered samples generally resulted in

structures of higher modulus (1.2 GPa) when compared to the sintered samples (Figure 38).

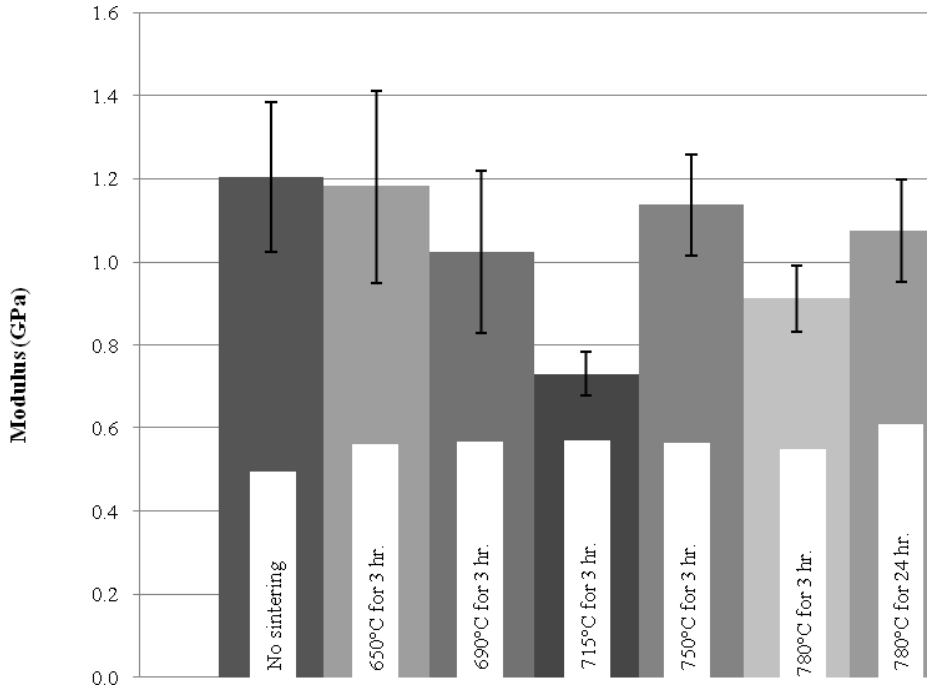

Figure 38: The compressive Young's modulus of polycrystalline NaCl as a function of the sintering conditions.

4.6. Fracture behaviour of bulk polycrystalline NaCl

The fracture behaviour of NaCl samples were analysed using SEM. Non-sintered samples (Figure 39A) and sintering at 650°C for 3 hrs (Figure 39B) exhibited mostly transgranular fracture. Samples that were sintered at 690°C (Figure 39C) and 715°C (Figure 39D) for 3 hrs exhibited mostly intergranular fracture. Samples sintered at 750°C (Figure 39E) and 780°C (Figure 39F) for 3 hrs appeared to exhibit approximately 90% and 50% intergranular fracture, respectively. Samples sintered at 780°C for 24 hrs tended to exhibit transgranular fracture (Figure 39G).

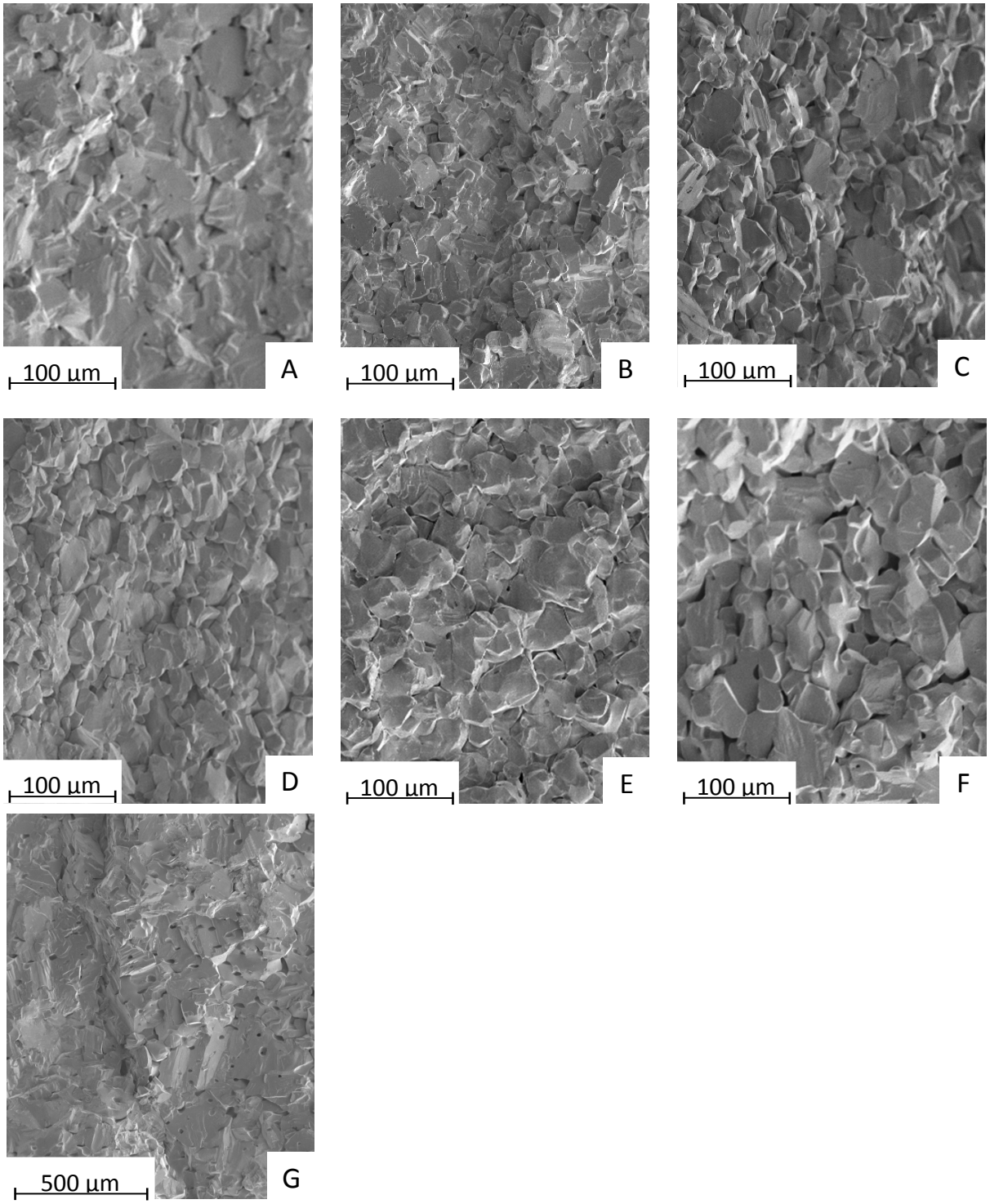

Figure 39: Scanning electron micrographs of the fracture surfaces of bulk polycrystalline NaCl samples: (a) non-sintered, (b) 650°C for 3 hrs, (c) 690°C for 3 hrs, (d) 715°C for 3 hrs, (e) 750°C for 3 hrs, (f) 780°C for 3 hrs and (g) 780°C for 24 hrs.

4.7. Discussion

The NaCl paste designed to infiltrate an RP polymer scaffold was made from a mixture of NaCl powder and binder (gelatin and supersaturated NaCl). While other binders were trialled along with gelatin, early in the development of the paste the gelatin addition was found to be the most suitable due to its solubility in water, non-toxicity, ease of use and excellent flow ability when mixed with NaCl powder

Sintering is used to increase strength and density as well as to improve the particles interconnectivity [93]. Sintering of NaCl powder has been investigated and put into sintering diagrams, including all previous work at that time [94], where particle-particle neck growth and densification has been the main focus of study. More recently the data has been updated with experimental covering wider area, but as well to confirm older results [95, 96]. Because of the random shape of the particles utilized it was not found possible to measure the sintering neck growth. Another mechanism that is very similar to sintering is a creep mechanism that takes place when grains are pressed together in the presence of small amount of solvent, they compact and stick together. Stress concentration at the grain contacts cause dissolution and diffusion of material from high stressed surfaces to less stress concentrated areas when in solvent [97]. This mechanism is in geology called pressure solution creep and plays the main role in earth sediments increased density. Sodium chloride has been the material of choice for geologists to investigate the pressure solution creep mechanism [84-86, 98].

Before any sintering, the NaCl compacts had an average and maximum grain size of 22 and 60 μm, respectively, and a porosity of ~11%. Pore sizes were measured up to ~25 μm. After sintering there was no significant change in the porosity for any of the conditions used. Even samples sintered at the highest temperatures and longest times (*i.e.* 780°C for 24 hrs) had a porosity of ~13%, demonstrating a lack of any further densification during sintering. In contrast, it is reported that significant densification of compacted NaCl powder occurs within the first few minutes of sintering within a similar temperature range [95, 96]. However, the compacted samples in the present work were

prepared under conditions of pressure solution. During pressure solution, the assembly of NaCl particles are forced to contact each other in the presence of liquid solvent that facilitates the redistribution of NaCl through dissolution-precipitation. It is presumed here that the redistribution of NaCl results in a higher initial density in the compact compared with dry compaction such that changes in densification are observed at longer sintering times than investigated here [97].

The large bandwidth of the grain size measured in the EBSD maps indicates an observation consistent with discontinuous or abnormal grain growth [99]. It is speculated that the increase in fine grains with sintering at 650°C is due to the growth of even finer crystals in the non-sintered NaCl that cannot be resolved by the EBSD analysis (*i.e.* grains less than Ø 4.5 μm). The presence of fine, undetectable grains in the non-sintered NaCl is probably due to precipitation of fine crystals from the supersaturated NaCl solution during pressure solution.

Occasionally some difficulties with indexing of EBSD patterns occurred at the edges of pores. This appears to be due to the formation of charging “halos” that appear around the edges of pores where charge must build up on the NaCl surface. The appearance of these halos is related to the orientation of the sample with respect to the axis of the electron beam since the halos appear to have preferred directionality. Examples of charging “halos” are shown for a sample (750°C/3 hrs) in

Figure 40.

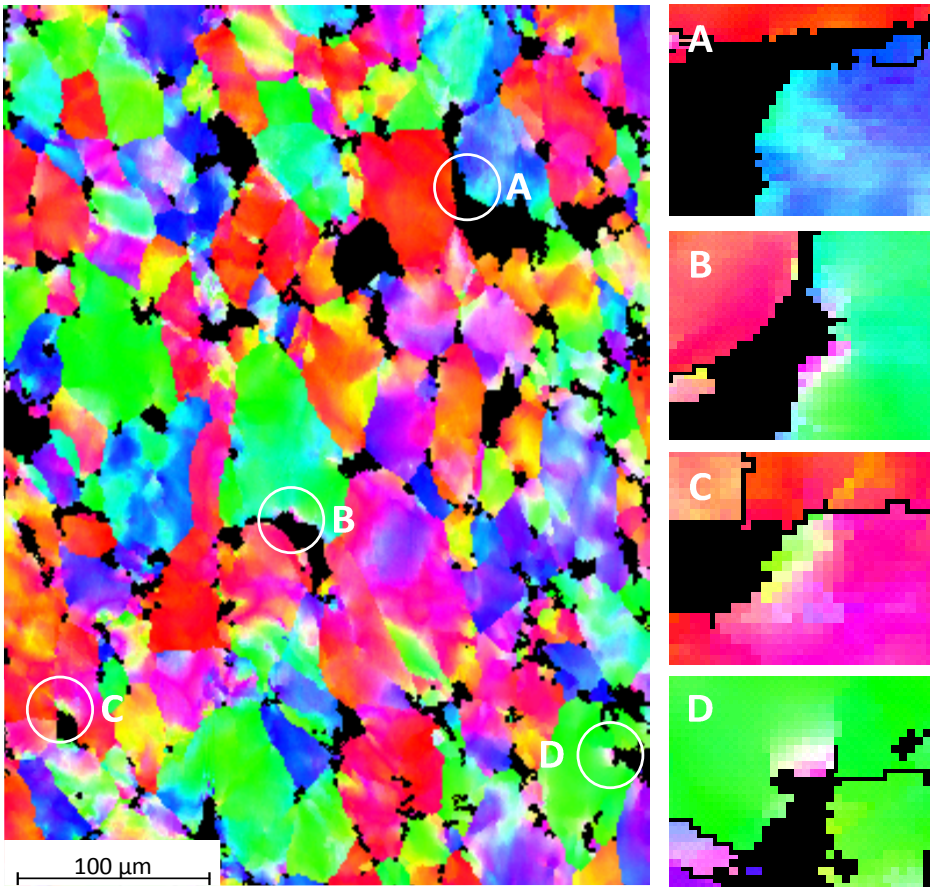

Figure 40: Example of charging “halos” effects around pores that were experienced on EBSD maps.

Non-sintered bulk NaCl failed by transgranular fracture. Transgranular type fracture was also experienced for samples sintered at 650°C for three hours and 780°C for 24 hours, while samples that experienced sintering in-between these temperatures experienced complete (690 and 715°C) or partial (750 and 780°C) failure by intergranular fracture. By comparing the fractography to the compression test results, a trend can be seen were transgranular NaCl fracture leads to a higher modulus and strength.

Concluding, the sintering of the NaCl does not improve its properties. The burn-out of the RP polymer and the gelatin requires a high temperature cycle that does sinter the NaCl as well, as explained in next chapter. The next chapter will guide us through the processing of the cellular Mg as well as its properties.

5. Fabrication and properties of ordered cellular Mg

5.1. Introduction

In chapter five the processing of the cellular Mg as well as its properties will be covered. First surface topology of the RP scaffold is analysed with the FESEM. Then the thermal properties of the scaffold material as well as the gelatine used in the NaCl paste are evaluated. Also the thermal properties of the NaCl powder and its particle size distribution are analysed. Thirdly X-ray microtomography (μ-CT) is used to evaluate the infiltration of the NaCl into two different RP scaffold designs, where errors in the NaCl templates are plotted as a function of the scaffold height. 3D reconstructions of the templates are also generated for visual evaluations. After that the surface topology of the NaCl template is analysed with the FESEM after the RP polymer had been burned out. Also the properties of resulted ordered cellular Mg are analysed in the chapter as well as the surface morphology. Finally the results of the previous are discussed in the last part of chapter 5.

5.2. Surface topology of the RP polymer

The surface topology of the RP scaffolds made with VisiJet HR200 were analysed with FESEM. The surfaces of the struts of the RP scaffold were observed to possess a “micro-valley” topology on surfaces that were parallel to the RP modeller printing plane (Figure 41). These micro-valleys were found to be formed by the layering technique that the modeller utilizes. The valleys were found to have approximately the same spacing as the layer thickness of the RP modeller (*i.e.* ~32 μm or 800 dpi).

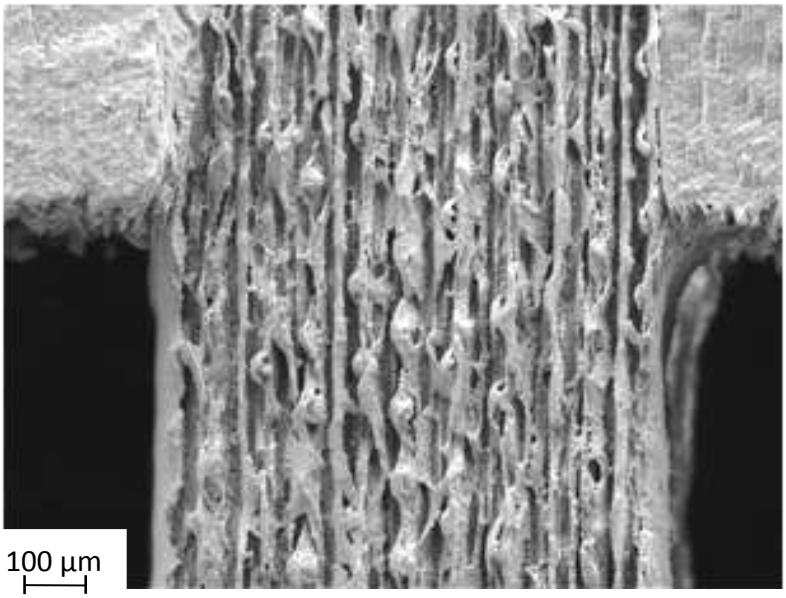

Figure 41: Scanning electron micrograph of the surface of a 1 mm wide strut showing micro-valleys running vertically in the image. The direction of RP modelling is parallel to the micro-valleys.

5.3. Thermal properties of VisiJet HR200 and gelatin

The thermal properties of VisiJet HR200, and gelatin were analysed using thermogravimetric analysis (TGA) to assist with the optimising the burn-out cycle after infiltration with the NaCl paste. VisiJet HR200 exhibited a glass transition (T_g) at 296°C and completely decomposed at temperatures below 466°C (Figure 42). High T_g means the polymer has high thermal stability, therefore it will also retain good dimensional stability during burn out. The largest proportion of the polymer was observed to decompose between ~280-460°C. The burn-out cycle for VisiJet HR 200 as recommended by the manufacturer yielded a successful burn-out without damage to the NaCl template. Gelatin fully decomposed at temperatures below 674°C (

Figure 43). The non-sintered bulk NaCl was also analysed with TGA and found to lose ~2% of its mass when heated to 780°C (Figure 44).

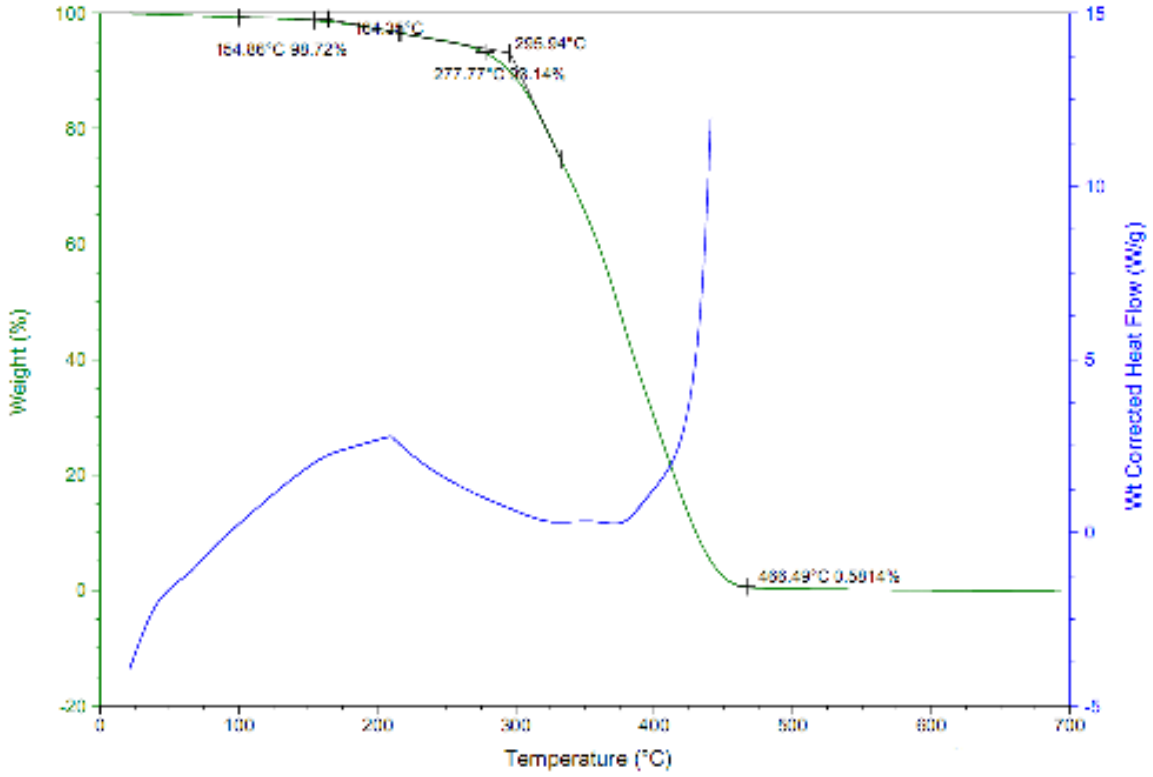

Figure 42: Weight and heat flow of VisiJet HR 200 as a function of temperature.

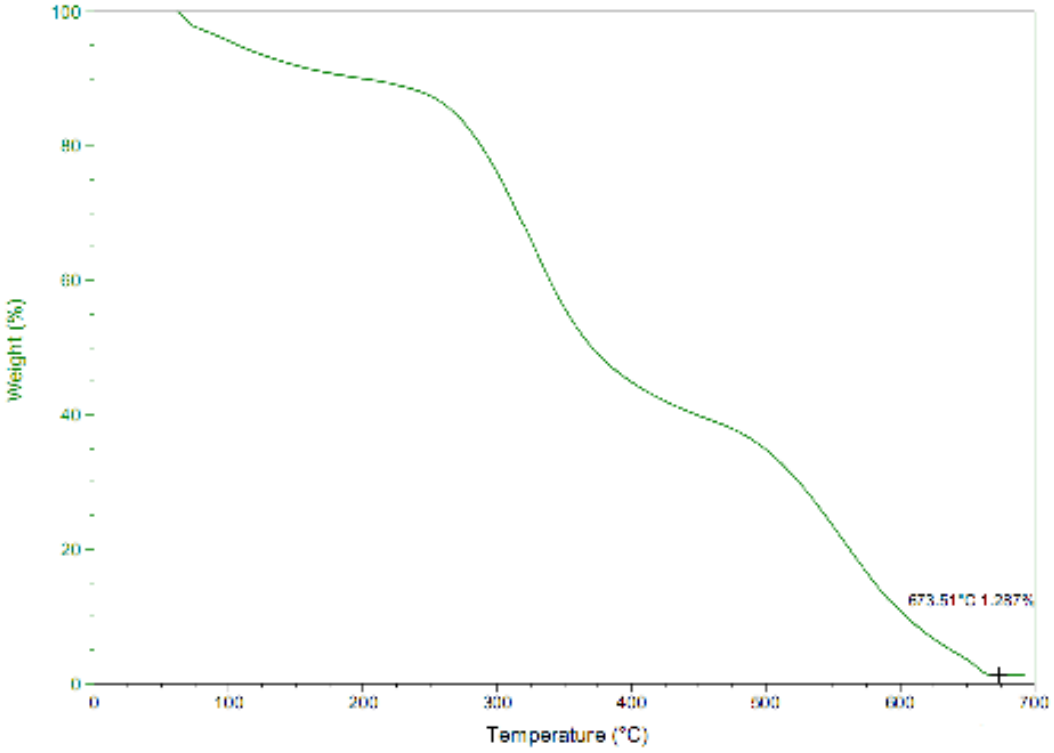

Figure 43: Weight loss of gelatin as a function of temperature.

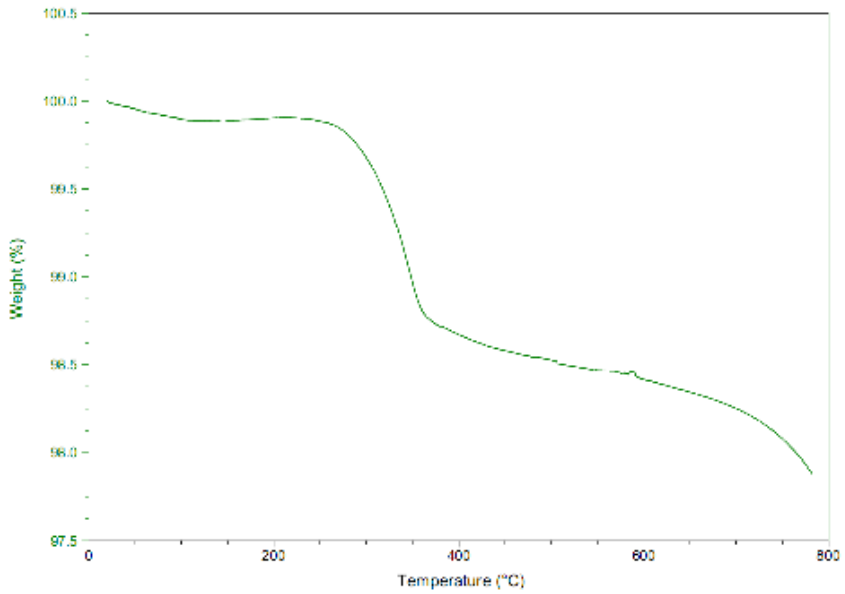

Figure 44: Weight loss of non-sintered NaCl as a function of temperature.

The distribution of particle sizes for the milled and sieved NaCl powder used in the NaCl paste was measured using a laser particle analyser (Figure 45). It was found that approximately 4% of the particles had a larger diameter than the size of the sieve used (*i.e.* 63 µm), presumably due to particle agglomeration after sieving. The particles were carried through the machine in high purity ethanol. NaCl is only slightly soluble in ethanol (1.4 g NaCl / 100 g ethanol) [100] so immersion in ethanol should have minimal effect on the particle sizes measured. This also appears to correspond well with the observation that particle sizes of 60-65 µm were detected, correlating well with the mesh size used (63 µm).

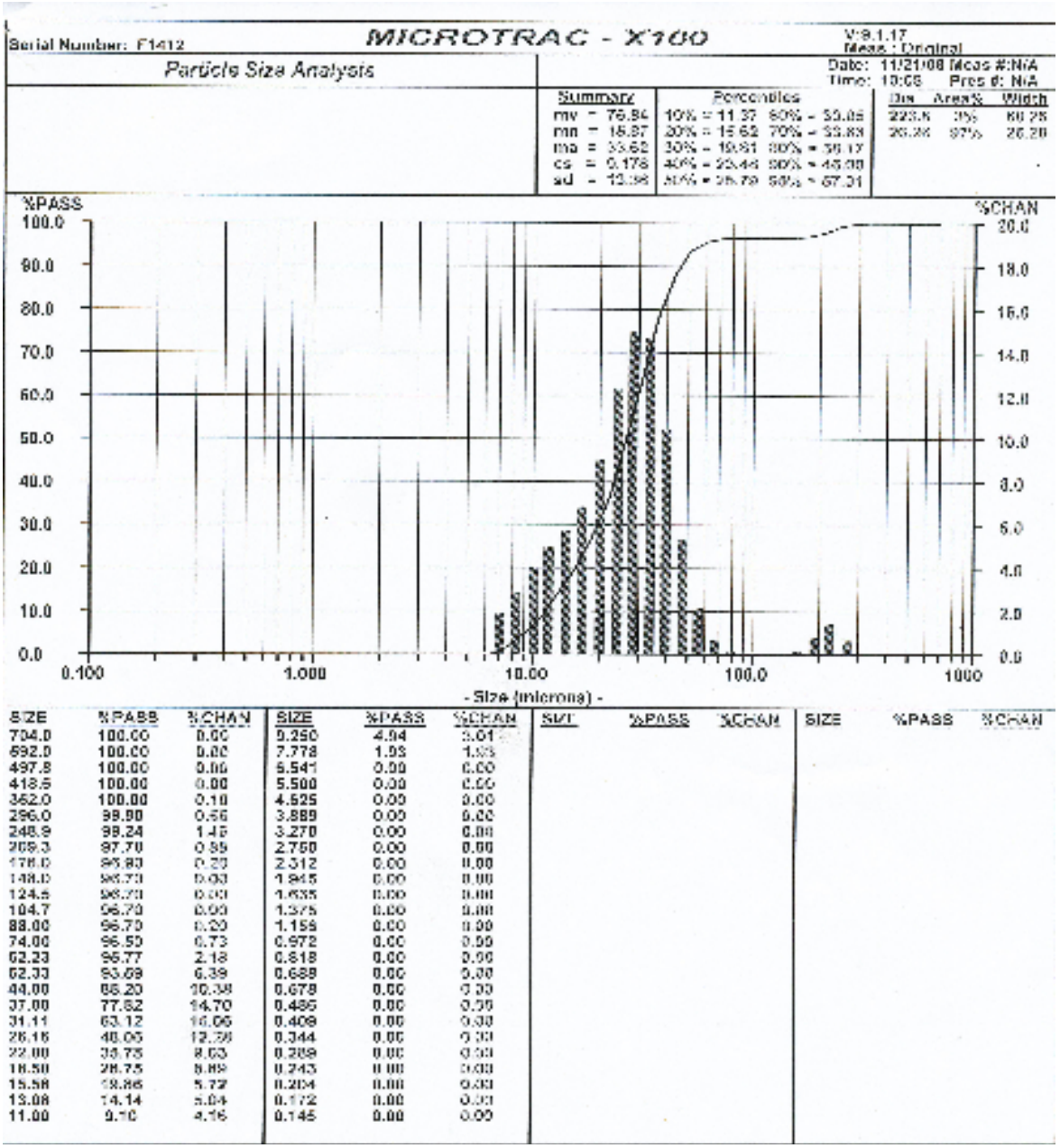

Figure 45: NaCl particle size distribution as measured by laser particle analysis. The solid line corresponds to the left-hand Y-axis (total pass of particles) while the bars correspond to the right-hand Y-axis.

5.4. The infiltration behaviour of NaCl paste in RP scaffolds

X-ray microtomography (μ-CT) was utilised for the purpose of analysing the extent of NaCl paste infiltration in two different types of scaffolds: (i) gradient RP structure (*Figure 46*A) and (ii) uniform 1 × 1 mm RP lattice structure (*Figure 46*B). The density of 3-D computer-reconstructed NaCl templates was compared with that of the initial CAD models used to print the RP models. The gradient structure was used to evaluate infiltration limitations in the process by studying (i) the effect of pore size and (ii) extent of infiltration as a function of the height through the scaffold. The gradient scaffold was designed containing 30 pores for each pore size. Dimensions of the rectangular pores in the scaffold were 0.1, 0.15, 0.2, 0.25, 0.3, 0.4, 0.5, 0.65, 0.8 and 1.0 mm for each side on the rectangle. The 1 × 1 mm scaffolds were used to evaluate the "completeness" of infiltration and how this varies within regions of differing porosity. Both scaffolds had outside dimensions of 20mm height and 20mm in diameter.

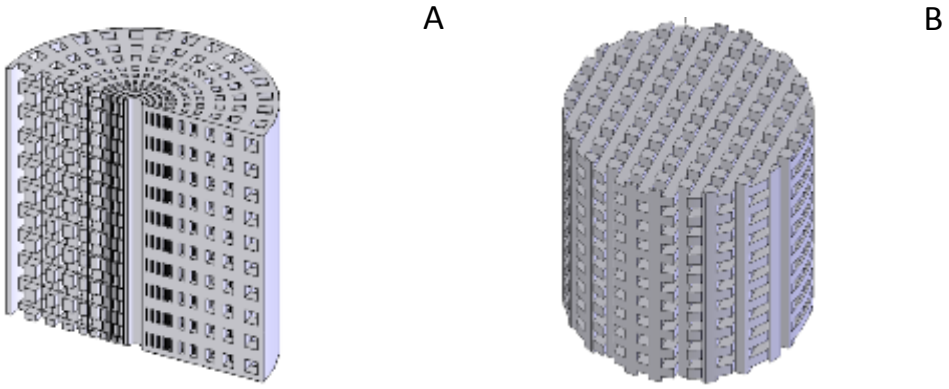

Figure 46: Schematics of the two CAD models used in this work: (a) cross-sectional view of the gradient structure and (b) uniform lattice structure with 1 × 1 mm struts and channels.

A series of cross-sectional BMP images were obtained with isotropic pixel size (step size between slices) of 37 μm as slices through the height of the samples. For the gradient structure images were cropped to give a group of 30 same sized pores (channels in the structure) for the analysis of dimensional errors. The individual pore

groups were measured at nine points throughout the sample height and each measurement consisted of seven images in the middle of each lattice (Figure 47A & B). For the 1 x 1 mm lattice structure, the entire image area was measured from top to the bottom. The porosity and error measurements were made by converting images to black and white pixels and masking a set area for the measurements using image analysis software (ImageJ, NIH Image). A 3-D reconstruction of the µ-CT images was performed with Mimics software (Materialise, Belgium).

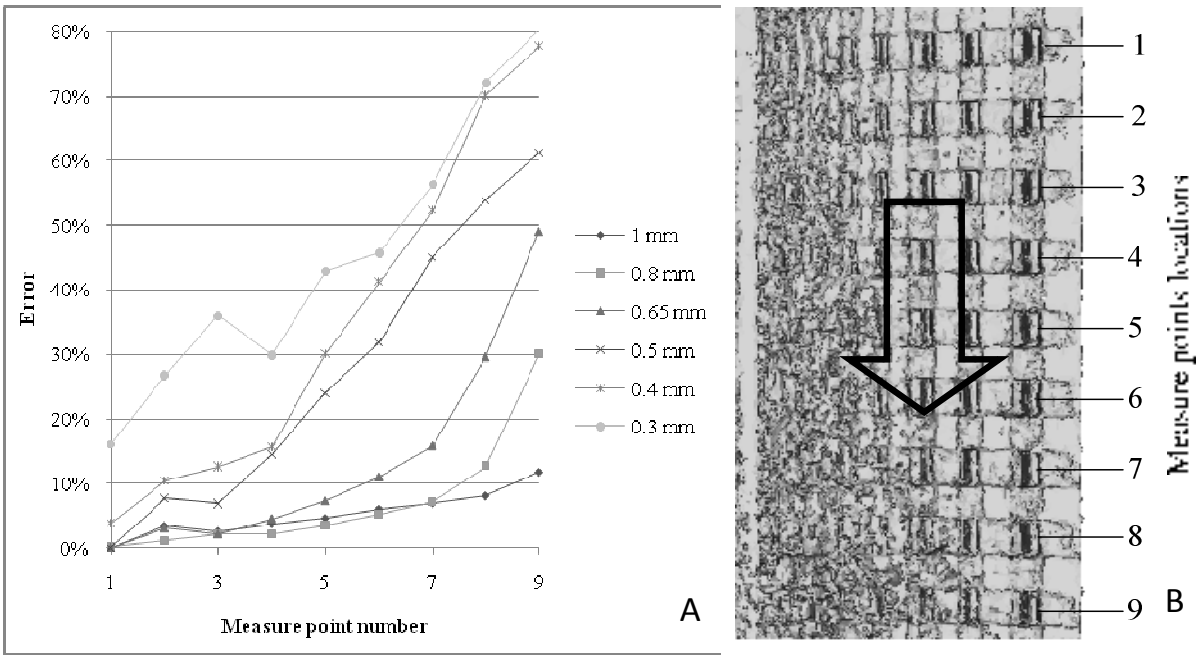

Figure 47: (a) Dimensional error between CAD model and NaCl template for the gradient RP structure as a function of channel size and depth through the scaffold as taken from the locations in (b), where the back arrow indicates the direction of infiltration.

For the gradient structure it was found that smaller pores resulted in greater discrepancies with the original CAD design. For example, the maximum error for the 1 mm channels was ~10%, while for the 0.3 mm channels it was >80% (Figure 47). Pores in the size range 0.65 to 1 mm had very similar infiltration properties in the top half

(14mm) of the scaffold. Pore sizes of 0.1, 0.15, 0.2 and 0.25 mm were not infiltrated with NaCl. The templates were reconstructed (Figure 48B - D) and then compared to the original CAD model (Figure 48A).

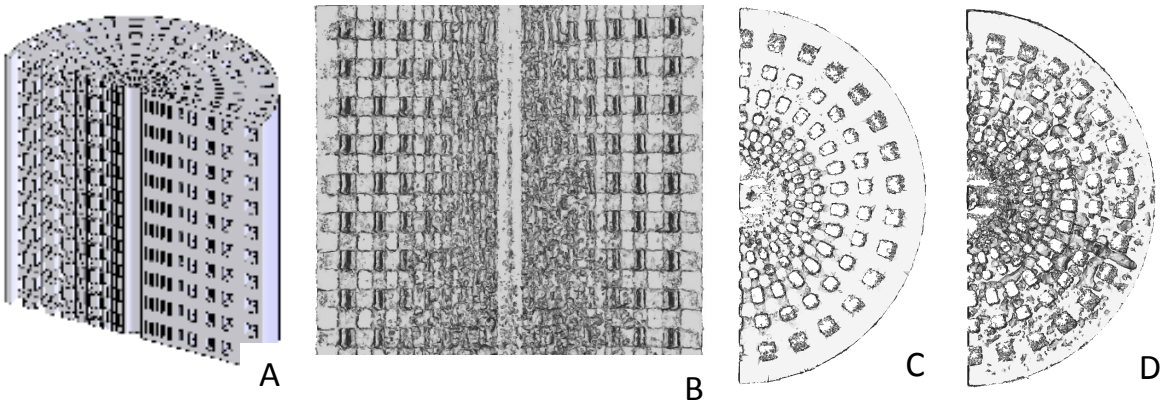

Figure 48: (a) Cross-section of gradient CAD model and (b) cross-section, (c) top surface and (d) bottom surface of actual gradient NaCl template.

The porosity of the sintered (690°C) lattice structure was compared to the CAD model by plotting over the sample height (Figure 49 and Figure 50). The porosity was found to be mostly constant for regions that intersect open channels. The porosity was observed to increase with increasing scaffold depth for the measurements in regions where struts should be present (Figure 49A). For the low porosity regions, the uniform 1 × 1 mm lattice NaCl template had a porosity ranging from ~43 to 47%. Therefore, on average the uniform 1 × 1 mm lattice NaCl template had 20% greater porosity than the corresponding CAD model. For the high porosity regions, the porosity of the idealized CAD model was 75%, while the NaCl template porosity was 83%. It was typical for a 20 mm long template to shorten by 0.5 mm before burn-out of the polymer scaffold.

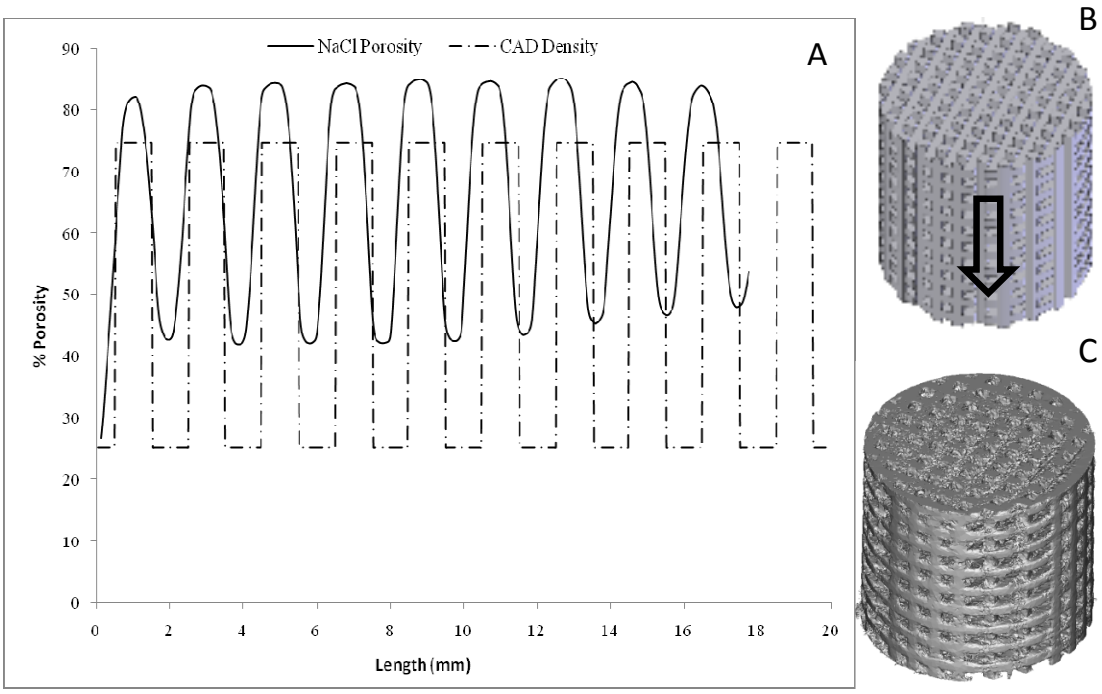

Figure 49: (a) Porosity differences between the idealized template porosity as a function of depth through a 1 x 1 mm lattice structure, (b) CAD model of the RP scaffold and (c) 3-D μCT reconstruction of the NaCl template, where the back arrow indicates the direction of infiltration and μCT scan.

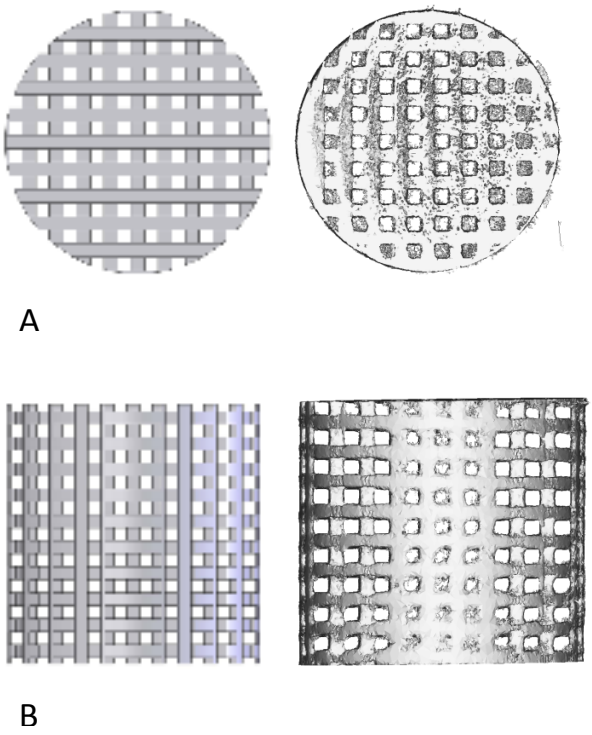

Figure 50: Comparison of CAD models (left) with actual NaCl templates (right). (a) top view and (b) side view.

5.5. Characterisation of NaCl templates after polymer burn-out

RP 1 x 1 mm lattice structure was successfully burned-out and the resulting NaCl was sintered at 690°C. The NaCl template was found to be strong and easy to handle. Photographs of the resulting Ø20 x 20 mm porous NaCl template before (Figure 51A) and after (Figure 51B) burn-out/sintering process are shown in Figure 51 .

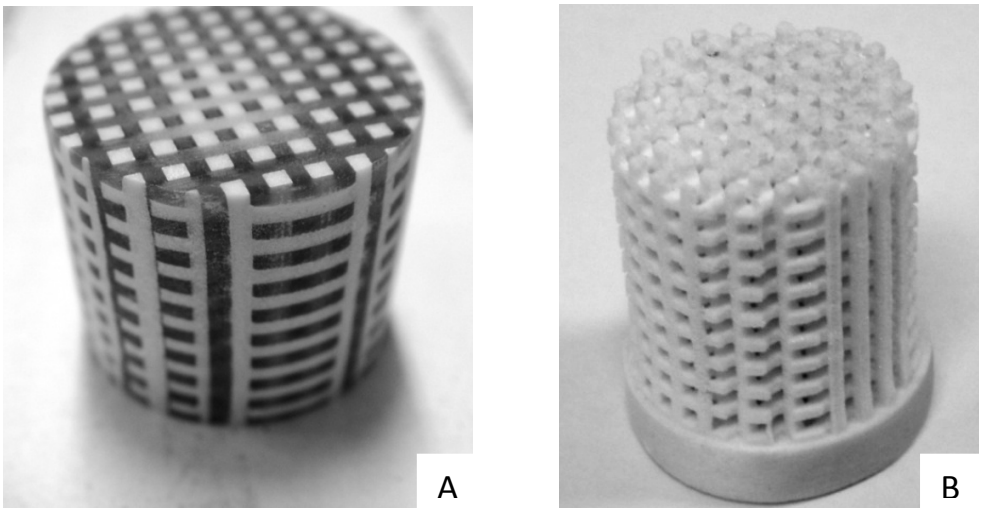

Figure 51: Photographs of the 1 x 1 mm lattice structure NaCl template (a) before and (b) after burn-out of the RP scaffold.

The surface topology of the 1 x 1 mm lattice NaCl was analysed using FESEM (Figure 52). Micro-valleys found on the RP scaffold (Figure 41) appear to be partially transferred to the inverse salt mould, although the size of the NaCl particles (< 63 μm) probably resulted in limited penetration of the micro-valleys in the RP structure. Penetration of micro-valleys by the NaCl is not obvious in the FESEM micrographs due to the large size and random orientation of the salt grains.

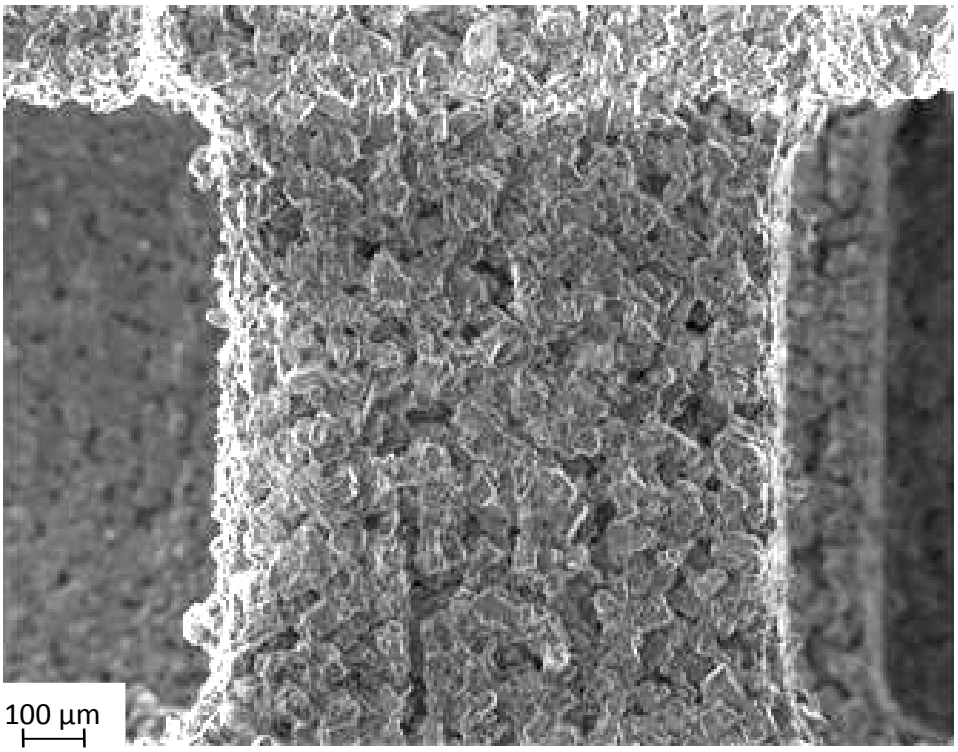

Figure 52: Scanning electron micrograph of the surface of the NaCl template after burn-out.

5.6. Processing and properties of ordered cellular magnesium

5.6.1. Effect of casting pressure on metal infiltration

Initial infiltration trials demonstrated that the NaCl structures could not be infiltrated by liquid Mg without an applied pressure, suggesting a lack of wetting between liquid Mg and NaCl. Infiltration pressures of 1.4 and 1.5 bar only gave partial infiltration of the NaCl lattice structure (Figure 53A and B). Moreover, the Mg flow front exhibited smooth curved surfaces, which was further evidence of the poor wetting between Mg and NaCl (Figure 53G).

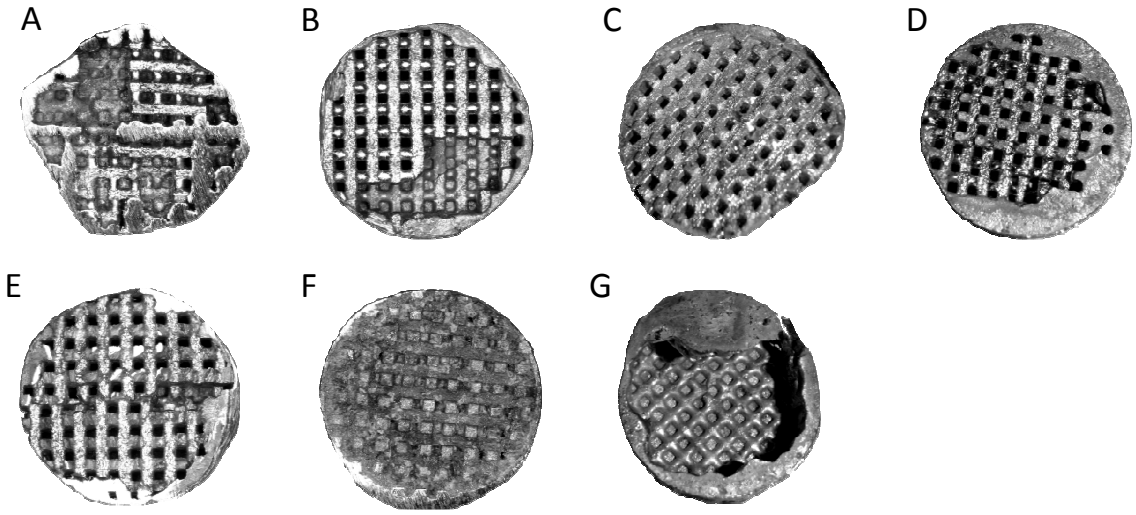

Figure 53: Mg foam structures produced with infiltration pressures of (a) 1.4 bar, (b) 1.5 bar, (c) 1.6 bar, (d) 1.7 bar, (e) 1.8 bar and (f) 1.85 bar. (g) illustrates the poor wetting between the Mg and the template at very low pressures.

Pressures of 1.8 bar yielded almost complete infiltration (Figure 53E), while at higher pressures of 1.85 bar the Mg permeated into the micro-pores between the salt grains within the struts of the NaCl structure (Figure 53F and Figure 54).

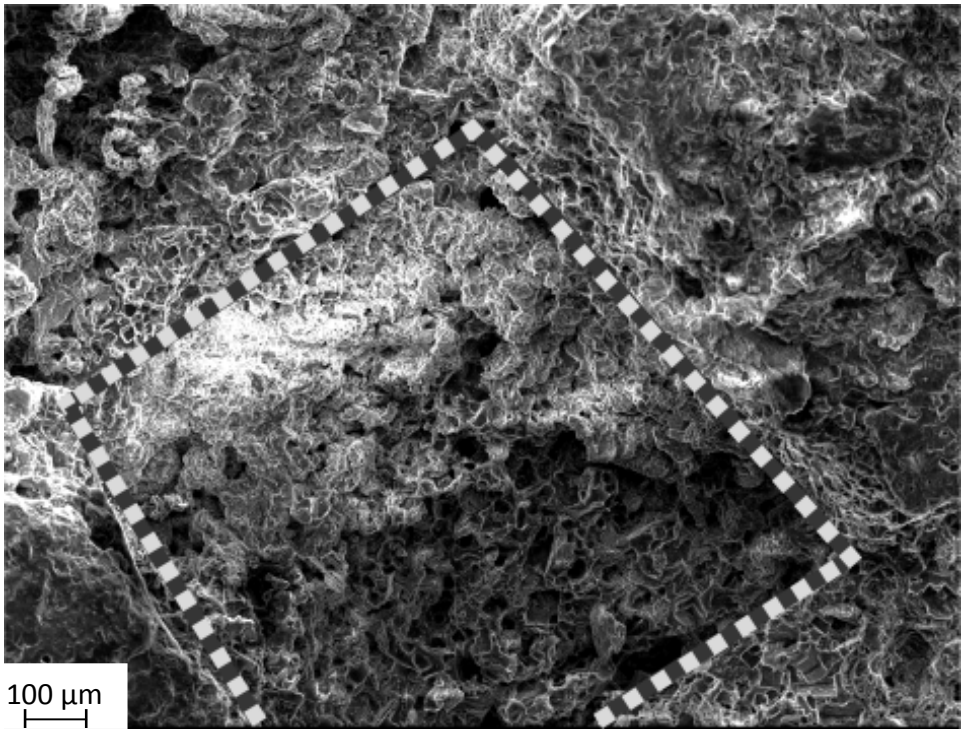

Figure 54: SEM of the Mg infiltration between salt grains within struts at 1.85 bar (Figure 53F), where the dotted lines indicate the boundary of the original pore.

5.6.2. Surface morphology of cellular Mg

The surface topologies corresponding to different infiltration pressures are shown in Figure 55. It can be seen that the roughness of the surface is increased significantly as the infiltration pressure increases. The Mg wets the salt surface, leaving reverse imprints of the salt grains on the surfaces of the struts.

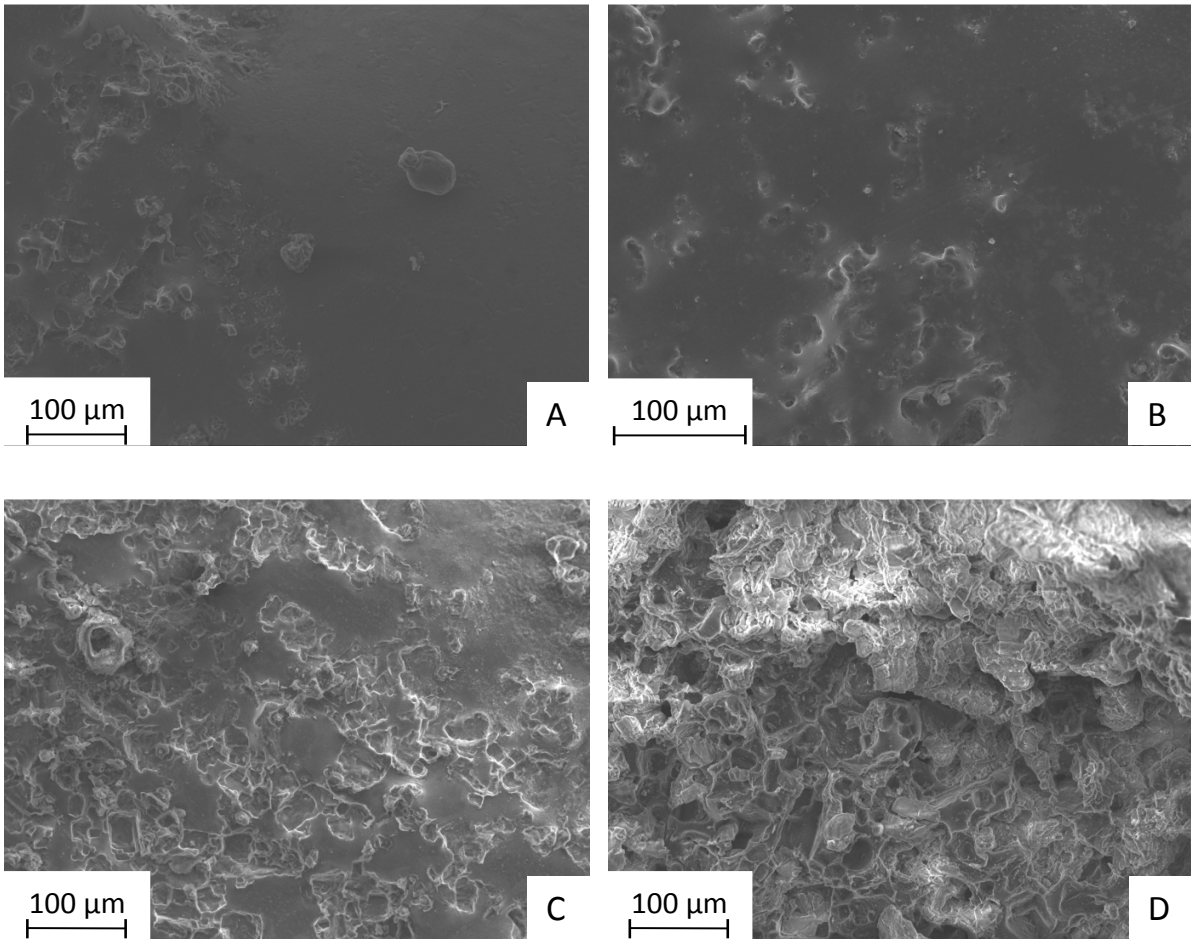

Figure 55: SEM pictures of the surface of cellular Mg casted under different pressure conditions; (a) 1.4 bar, (b) 1.6 bar, (c) 1.8 bar and (d) 1.85 bar.

Confocal microscopy (Leica® TCS SP5) was used to characterize the surface topology of the final as-cast porous Mg. The confocal micrographs were analyzed with specially-developed software to obtain surface roughness (R_a) values. The surface roughness of the P_i = 1.8 bar infiltration is more than twice that of P_i = 1.4 bar (Figure 55C), which Table 4 appears to confirm.

Table 4: Surface roughness values of cast cellular Mg.

P_i (bar)	R_a (μm)
1.4	11.07
1.5	11.49
1.6	17.54
1.8	23.36

The RP scaffolds used to create the inverse salt templates had a roughness with micro-valleys ~30 μm across (Figure 41). Those valleys did appear to be partially transferred to the inverse salt template (Figure 51). However, it was clear from the Mg sample at the higher pressures (1.8 bar) that some of the original features had been transferred to the Mg strut surfaces (Figure 56).

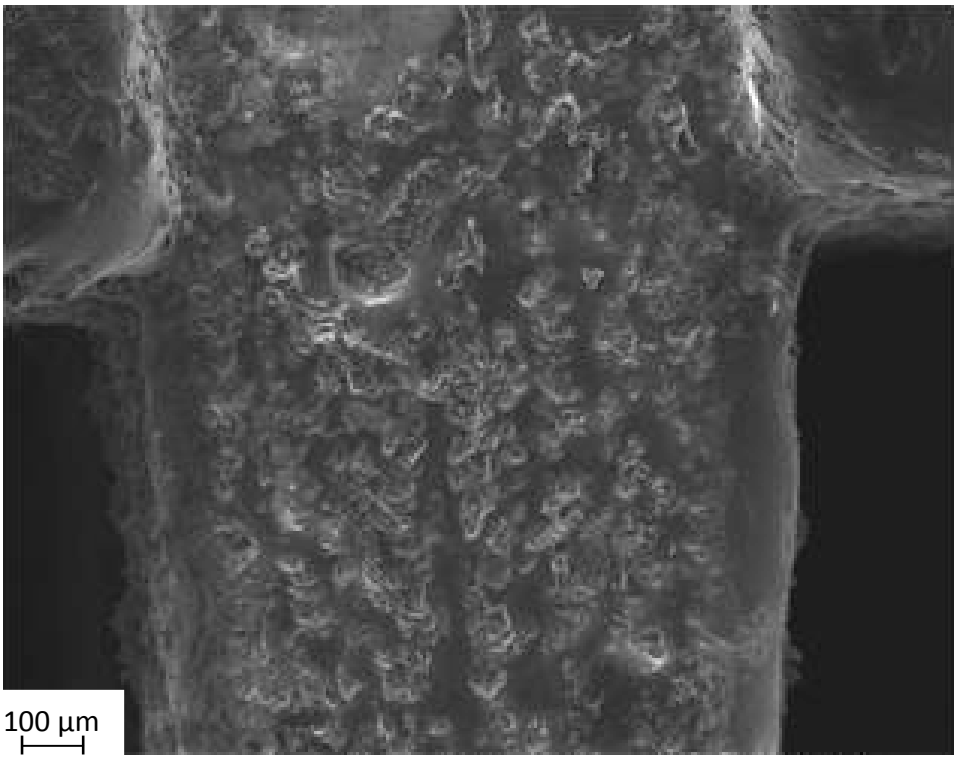

Figure 56: Scanning electron micrographs of the micro-valley architecture partially transferred from the rapid prototype to cast Mg surface.

5.6.3. Mechanical properties of controlled cellular Mg

The periodic (1 × 1 mm) Mg were found to exhibit equivalent or slightly higher ultimate compressive strengths (~13 MPa) compared to bulk Mg (~11 MPa) with an equivalent cross sectional area of the vertical struts.

5.7. Discussion

Burn-out properties of the VisiJet HR 200 material were analysed using TGA analyser. The polymer was found to be fully decomposed at a lower temperature than the recommended burn-out temperature by manufacturer. It was fully decomposed at 466°C, making it possible to explore NaCl sintering temperatures above that temperature. The burn-out cycle recommended by 3D systems was utilized as it did not

cause fracture or cracks in the NaCl template. It was decided to use that cycle, even though it did not go slowly through delicate zones in the burn-out cycle. The heating rate used for the TGA was higher than the heating rate utilised in the burn-out cycle and therefore those values are lower for the burn-out cycle. As the glass transition temperature (T_g) is a kinetic parameter, and thus parametrically depends on the heating rate. The quicker the heating rate, the lower the T_g.

Interesting micro-valleys were found on the RP scaffold surfaces caused by the layering process the RP process utilises. The ability to control the surface topology on the metal is important for mechanical properties since it will affect crack propagation and load transmission through the introduction of “defects” and stress raisers at the surface. Those micro-valleys on the RP scaffold can not be controlled, because the layer thickness is a constant parameter. But furthermore the surfaces that are parallel to the printing plane have a flat texture. The resolution on the 3D modeller is slightly less in the x and y directions (656 DPI) than for the z-direction, a.k.a. layer thickness (800 DPI). Since the resolution is quite similar it might be possible to implement micro-valleys into the CAD design for the “flat surfaces” through the fabrication process. By doing this the surfaces of the cellular Mg would be more uniform throughout the structure.

After the aqueous NaCl paste is infiltrated into the RP scaffold it was kept at constant pressure for one hour, normally 2.0 MPa, before the drying process starts. At this stage a dissolution process, described in last chapter called pressure solution creep moves material from high stressed grain contacts areas through thin solvent layer [97]. The nonsintered bulk NaCl sample analysed in the TGA was found to decompose ~ 2wt% by heating it up to the highest sintering temperature utilised in the experiments. This decomposition from the NaCl might be caused mainly by evaporation of thin water films entrapped between the NaCl particles. The great drop in weight at 200-400°C could be caused by this while the rest can be caused by NaCl evaporation. Those questions can though not be fully answered and this is more predictions rather than facts. Geologists have been studying this since the 1960´s and still there are many unanswered questions regarding this mechanism today [84-86, 98].

The gelatine was found to be fully decomposed at 674°C. That is quite higher temperature than the RP polymer did decompose at making the gelatine the benchmark for the lowest sintering temperature used for the NaCl template. This would prevent any gelatine left over that might have been left in the NaCl template after drying to burn when Mg melt is introduced and possibly upset the casting process. The thermal expansion of the gelatine is not able put any load on the NaCl structure since it lies in-between the small NaCl particles and it does free up large spaces by shrinkage when dried.

Infiltration behaviour of the NaCl paste were investigated to map the errors in the process.. Two different RP scaffold designs were used utilised and infiltrated with NaCl paste. The resulting NaCl templates were analysed for dimensional and volume errors using X-ray microtomography (μ-CT). The porosity of the NaCl struts did not affect the volume analysis because the resolution of the μ-CT was not high enough to capture fine pores contained between the individual NaCl grains. So the positive CAD model could accurately be compared to the negative NaCl template for accuracy of the template production. Accurate μ-CT models of the RP scaffolds were not possible make because of how large contrast difference between the centre and edges of the scaffold. Because of this it is not known how much of the defects in the template structure is caused by the infiltration process it self or defects in the RP scaffold. It was found visually that some of the smaller diameter pores were already blocked in the RP scaffold due to reaching the lower resolution limit of the RP process. Also a dimensional error in the height of the 1 x 1 mm lattice template was experienced. It is believed that it is mainly caused by the pressure applied to the RP scaffold while infiltrating it with the NaCl paste, deforming the RP scaffolds non reversely.

The ability to control the surface topology is important for mechanical properties since it will affect crack propagation and load transmission through the introduction of “defects” and stress raisers at the surface. Moreover, the surface micro-architecture or topology of orthopaedic implant devices is recognized as an important parameter for encouraging new bone formation [101-104]. For example, Schwartz *et al.* [104] found

that implants with surface roughness values (R_a) of 3 to 6 μm increase cell proliferation by up to 9 times compared with a smooth surface (R_a = 0.2 μm).

This suggested that the process developed here may give a range of different surface topologies by careful control of the infiltration conditions. The NaCl particle size could be selected to tailor the desired surface roughness using this approach. For example did Wilson *et al.* [105] found that “valleys” 40 μm wide and 20 μm deep had a positive effect on proliferation of bone cells when compared to smooth surfaces. For example the NaCl could be processed over narrower size range than now utilised (0-63 μm) for more uniform texture. Also larger or smaller particles could be used to receive different roughness on the Mg surface. It should be kept in mind that two other parameters also affect the surface texture. The surface “micro-valleys” on the RP scaffold gets copied partly over to the NaCl template as well as the casting infiltration pressure of the Mg also can be used.

For the compression tests of the Mg it was thought that the introduction of sharp corners into the lattice structure may have led to lower strengths. However, the contribution from the cross struts in supporting the vertical columns are a significant mechanism for strengthening these structures. Interestingly, the periodic structure, which has a theoretical porosity of 41%, exhibited compressive strengths just below that for other random porous Mg foams reported in the literature. In particular, Wen *et al.*[106] reported compressive strengths of 15 MPa for 41% porosity. It was also noted that the pore size of the foams influenced the strength, with larger pores resulting in reduced properties. On this basis, if the ordered porous foam structure could be considered to have an effective pore size of 1 mm, this would yield values less than 9 MPa for a random porous structure.

6. Conclusion

In this work a new technique to fabricate porous magnesium (Mg), with controlled cellular structure utilizing a rapid prototyping (RP) was introduced. Where the Mg of desired architecture was designed in a 3D CAD software and the replica of the part was fabricated using 3D RP polymeric printer. RP polymer scaffolds were infiltrated using specially designed slurry of NaCl powder. NaCl was successfully infiltrated into the RP scaffold pores with dimensions 0.3 x 0.3 mm and larger. The RP scaffolds were found to condense irreversibly under certain conditions, primarily due to the pressure applied when infiltrating NaCl paste into them. Removal of the polymer resulted in an accurate negative NaCl template that could be infiltrated with magnesium (Mg). The NaCl template was infiltrated with liquid Mg in induction furnace using low pressure die casting method. Subsequently when solidified the NaCl was dissolved in sodium hydroxyl solution.

The properties of the magnesium cast into the NaCl structure were studied. It was found that the casting pressure used had a large effect on not only the infiltration success and mechanical integrity, but also the surface texture and wetting of the NaCl. Although higher pressures improved some of these characteristics, they also could lead to uncontrollable effects such as infiltration between the NaCl grains. Correct control of these parameters, however, can result in an Mg structure with properties (surface roughness, “valley” architecture) that are heavily desired by the biomedical industry.

Sintering conditions of the NaCl structure was studied in detail by producing bulk structures analyzed using compression testing, scanning electron microscopy (SEM) and electron backscattered diffraction (EBSD). It was found that under conditions where shrinkage was not observed or showed little densification, there was no real benefit to the added strength of the template. Both compression testing and SEM fractography did indicate that the particles have already been fused together via pressure solution creep mechanism in the infiltration process. The grain structure and grain growth of the sintered and non sintered samples was also studied in details using the EBSD mapping.

For this work a new sample polishing technique had to be developed for the macro porous NaCl structure. No grain growth took place at lower sintering temperatures utilized but at higher temperatures a small grain growth was found, when small grains did consolidate into larger. A great grain growth was noticed in the sample sintered for the longest time. This sample also experienced shrinkage caused by densification.

Thus, the main findings in this thesis are:

- a novel 3D RP fabrication method to cast Mg with controlled cellular structure using NaCl as an inverse casting template was developed.

- a new sample preparation technique was introduced to polish the delicate micro porous NaCl to use in the SEM for EBSD analysis.

7. Suggestion for future work

In this thesis a novel sodium chloride (NaCl) templates with controlled cellular structure were fabricated to cast magnesium into. Many variables can be adjusted to improve the fabrication process; most of them are fairly unknown while limited data is available for others, such as sintering. One of the key factors to further improve the NaCl template would be to research the infiltration of the NaCl paste into the rapid prototyping (RP) scaffold. In this thesis the paste mixture ratio were investigated and optimised. A further investigation showing how the NaCl particle size and the powder size distribution influence the paste flow can be implemented. It should be noted that the particle size of the NaCl powder can influence the magnesium (Mg) surface roughness, the paste drying process and too large grains may cause the Mg to infiltrate in-between the grains.

After the paste is infiltrated into the RP mould the paste is kept under pressure in the infiltration device for one hour inside a furnace. Over this period of time a pressure solution creep mechanism is acting, it fuses the grains together by dissolution of stressed surfaces and therefore the structure density increases. In this process three main variables can be adjusted; time, pressure and temperature, that will all affect the creep rate. Increased density of the template will increase its strength and it will also reduce the template shrinkage if sintered to that high level. Ideally a fully densified template would be the way to go, but the gelatine/brine mixture has to be able to escape and also it has to be possible to dry the structure using the vacuum pump.

The relationship between the original CAD model and the final NaCl pore morphology was investigated using micro-computed tomography (μ-CT) to get a better understanding of the errors and limits in the process. To fully evaluate those parameters for the overall process a similar analysis needs to be carried out for the final cellular Mg structure as was done for the NaCl template. With this the total errors and limits of the process would be mapped and could be implemented into the CAD design for more accurate production.

NaCl has also been used to fabricate porous biodegradable composite and polymer scaffolds. The scaffolds are fabricated by solvent casting, where composite or polymer solution is poured over the NaCl scaffold. The solvent is then removed by evaporation and then the NaCl particles are dissolved with water [107, 108]. Those new NaCl templates with ordered cellular structure have a good potential to work for those materials as well as Mg. This would need to be tested to confirm that those different materials can be infiltrated into the new NaCl templates.

8. References

[1] F. von Zeppelin, M. Hirscher, H. Stanzick, and J. Banhart, "Desorption of hydrogen from blowing agents used for foaming metals," *Composites Science and Technology,* vol. 63, pp. 2293-2300, Dec 2003.

[2] A. Irretier and J. Banhart, "Lead and lead alloy foams," *Acta Materialia,* vol. 53, pp. 4903-4917, Oct 2005.

[3] B. Matijasevic and J. Banhart, "Improvement of aluminium foam technology by tailoring of blowing agent," *Scripta Materialia,* vol. 54, pp. 503-508, Feb 2006.

[4] S. Esmaeelzadeh and A. Simchi, "Foamability and compressive properties of AlSi7-3 vol.% SiC-0.5 wt.% TiH2 powder compact," *Materials Letters,* vol. 62, pp. 1561-1564, Apr 15 2008.

[5] M. Haesche, J. Weise, F. Garcia-Moreno, and J. Banhart, "Influence of particle additions on the foaming behaviour of AlSi11/TiH2 composites made by semi-solid processing," *Materials Science and Engineering: A,* vol. 480, pp. 283-288, 2008.

[6] B. Matijasevic-Lux, J. Banhart, S. Fiechter, O. Görke, and N. Wanderka, "Modification of titanium hydride for improved aluminium foam manufacture," *Acta Materialia,* vol. 54, pp. 1887-1900, 2006.

[7] C. Wen, M. R. Barnett, J. Vella, and Y. Yamada, "Solid-state Foaming of Magnesium Alloys," in *Metfoam*, 2005.

[8] M. W. Kearns, P. A. Blenkinsop, A. C. Barber, and T. W. Farthing, "Manufacture of a Novel Porous Metal," *International Journal of Powder Metallurgy,* vol. 24, pp. 59-64, Jan 1988.

[9] F. Garcia-Moreno and J. Banhart, "Foaming of blowing agent-free aluminium powder compacts," *Colloids and Surfaces a-Physicochemical and Engineering Aspects,* vol. 309, pp. 264-269, Nov 1 2007.

[10] K. Renger and H. Kaufmann, "Vacuum foaming of magnesium slurries," *Advanced Engineering Materials,* vol. 7, pp. 117-123, Mar 2005.

[11] R. L. S. P. Martin, MO), "Integral porous-core metal bodies and in situ method of manufacture thereof," United States: McDonnell Douglas Corporation (St. Louis, MO), 1996.

[12] J. Banhart, "Manufacture, characterisation and application of cellular metals and metal foams," *Progress in Materials Science,* vol. 46, pp. 559-U3, 2001.

[13] N. Kanetake and M. Kobashi, "Innovative processing of porous and cellular materials by chemical reaction," *Scripta Materialia,* vol. 54, pp. 521-525, Feb 2006.

[14] I. Barin, F. Sauert, E. Schultze-Rhonhof, and W. S. Sheng, *Thermochemical data of pure substances*: VCH, 1989.

[15] M. F. Ashby, *Metal foams : a design guide*. Oxford: Butterworth-Heinemann, 1999.

[16] M. L. Jaeckel, DE), Smigilski, Hartmuth (Hamburg, DE), "Process for producing metallic or ceramic hollow-sphere bodies." vol. 4917857 United States: Norddeutsche Affinerie Aktiengesellschaft (Hamburg, DE), 1990.

[17] O. Andersen, U. Waag, L. Schneider, G. Stephani, and B. Kieback, "Novel metallic hollow sphere structures," *Advanced Engineering Materials,* vol. 2, pp. 192-195, Apr 2000.

[18] C. E. Wen, M. Mabuchi, Y. Yamada, K. Shimojima, Y. Chino, and T. Asahina, "Processing of biocompatible porous Ti and Mg," *Scripta Materialia,* vol. 45, pp. 1147-1153, Nov 19 2001.

[19] X. Q. Liu, Z. L. Liu, X. H. Zhang, J. D. Feng, and T. X. Yu, "Preparation and characterization of porous magnesium materials," *Transactions of Nonferrous Metals Society of China,* vol. 16, pp. S1859-S1863, Dec 2006.

[20] Z. Esen and S. Bor, "Processing of titanium foams using magnesium spacer particles," *Scripta Materialia,* vol. 56, pp. 341-344, Mar 2007.

[21] B. P. Neville and A. Rabiei, "Composite metal foams processed through powder metallurgy," *Materials & Design,* vol. 29, pp. 388-396, 2008.

[22] J. R. Groza and A. Zavaliangos, "Sintering activation by external electrical field," *Materials Science and Engineering a-Structural Materials Properties Microstructure and Processing,* vol. 287, pp. 171-177, Aug 15 2000.

[23] W. H. Lee and C. Y. Hyun, "Fabrication of fully porous and porous-surfaced Ti-6Al-4V implants by electro-discharge-sintering of spherical Ti-6Al-4V powders in an one-step process," *Journal of Materials Processing Technology,* vol. 189, pp. 219-223, Jul 6 2007.

[24] J. Qiu, J. T. Dominici, M. I. Lifland, and K. Okazaki, "Composite titanium dental implant fabricated by electro-discharge compaction," *Biomaterials,* vol. 18, pp. 153-160, Jan 1997.

[25] F. Watari, A. Yokoyama, M. Omori, T. Hirai, H. Kondo, M. Uo, and T. Kawasaki, "Biocompatibility of materials and development to functionally graded implant for

bio-medical application," *Composites Science and Technology,* vol. 64, pp. 893-908, May 2004.

[26] Z. A. Munir, U. Anselmi-Tamburini, and M. Ohyanagi, "The effect of electric field and pressure on the synthesis and consolidation of materials: A review of the spark plasma sintering method," *Journal of Materials Science,* vol. 41, pp. 763-777, Feb 2006.

[27] K. Okazaki, W. H. Lee, D. K. Kim, and R. A. Kopczyk, "Physical Characteristics of Ti-6al-4v Implants Fabricated by Electrodischarge Compaction," *Journal of Biomedical Materials Research,* vol. 25, pp. 1417-1429, Dec 1991.

[28] H. Okumura, K. Watanabe, S. Kamado, and Y. Kojima, "Fabrication of porous magnesium alloys by pulse electric current sintering process using machined chips," *Materials Transactions,* vol. 44, pp. 595-600, Apr 2003.

[29] K. Kitazono, E. Sato, and K. Kuribayashi, "Novel manufacturing process of closed-cell aluminum foam by accumulative roll-bonding," *Scripta Materialia,* vol. 50, pp. 495-498, Feb 2004.

[30] K. Kitazono and E. Sato, "Closed-cell metal foams manufactured from bulk metal and alloy sheets through ARB process," *Pricm 5: The Fifth Pacific Rim International Conference on Advanced Materials and Processing, Pts 1-5,* vol. 475-479, pp. 433-436, 2005.

[31] Y. Kikuchi, K. Kakehi, K. Kitazono, E. Sato, and K. Kuribayashi, "Magnesium foam produced from bulk AZ31 magnesium alloy sheets," *Pricm 5: The Fifth Pacific Rim International Conference on Advanced Materials and Processing, Pts 1-5,* vol. 475-479, pp. 501-504, 2005.

[32] A. E. Simone and L. J. Gibson, "Aluminum foams produced by liquid-state processes," *Acta Materialia,* vol. 46, pp. 3109-3123, May 22 1998.

[33] I. I. Jin, CA), Kenny, Lorne D. (Inverary, CA), Sang, Harry (Kingston, CA), "Stabilized metal foam body," United States: Alcan International Limited (Montreal, CA), 1992.

[34] N. Babcsan, F. G. Moreno, and J. Banhart, "Metal foams - High temperature colloids - Part II: In situ analysis of metal foams," *Colloids and Surfaces a-Physicochemical and Engineering Aspects,* vol. 309, pp. 254-263, Nov 1 2007.

[35] C. C. Yang and H. Nakae, "The effects of viscosity and cooling conditions on the foamability of aluminum alloy," *Journal of Materials Processing Technology,* vol. 141, pp. 202-206, Oct 20 2003.

[36] K. Kitazono, A. Kitajima, E. Sato, J. Matsushita, and K. Kuribayashi, "Solid-state diffusion bonding of closed-cell aluminum foams," *Materials Science and Engineering A,* vol. 327, pp. 128-132, 2002.

[37] W. S. Fiedler, "Method of making metal foam bodies," United States: LOR CORP, 1965.

[38] J. C. Elliott, "Metal foam and method for making," United States: LOR CORP, 1961.

[39] J. M. Babjak, CA), Ettel, Victor A. (Mississauga, CA), Paserin, Vladimir (Mississauga, CA), "Method of forming nickel foam," United States: Inco Limited (Toronto, CA), 1990.

[40] Y. Yamada, K. Shimojima, Y. Sakaguchi, M. Mabuchi, M. Nakamura, T. Asahina, T. Mukai, H. Kanahashi, and K. Higashi, "Processing of an open-cellular AZ91 magnesium alloy with a low density of 0.05 g/cm(3)," *Journal of Materials Science Letters,* vol. 18, pp. 1477-1480, Sep 1999.

[41] Y. Yamada, C. Wen, K. Shimojima, H. Hosokawa, Y. Chino, and M. Mabuchi, "Compressive deformation characteristics of open-cell Mg alloys with controlled cell structure," *Materials Transactions,* vol. 43, pp. 1298-1305, Jun 2002.

[42] Y. Yamada, K. Shimojima, Y. Sakaguchi, M. Mabuchi, M. Nakamura, T. Asahina, T. Mukai, H. Kanahashi, and K. Higashi, "Processing of cellular magnesium materials," *Advanced Engineering Materials,* vol. 2, pp. 184-187, Apr 2000.

[43] L. Q. Ma, Z. L. Song, and D. P. He, "Cellular structure controllable aluminium foams produced by high pressure infiltration process," *Scripta Materialia,* vol. 41, pp. 785-789, Aug 30 1999.

[44] J. R. Kreigh, Keith, Gibson James, "Metal-aggregate product," United States: Kreigh, Jack R.,Keith, Gibson James, 1962.

[45] F.-W. Bach, D. Bormann, and P. Wilk, "Cellular magnesium," *Cellular Metals and Metal Foaming Technology,* pp. 215-218, 2003.

[46] A. Pollien, Y. Conde, L. Pambaguian, and A. Mortensen, "Graded open-cell aluminium foam core sandwich beams," *Materials Science and Engineering a-Structural Materials Properties Microstructure and Processing,* vol. 404, pp. 9-18, Sep 15 2005.

[47] B. D. Bach Fr.-W., Kucharski R., Wilk P., "Production and Properties of Foamed Magnesium," *Cellular Metals and Polymers,* pp. 77-80 2005.

[48] H. A. Kuchek, "Method of making porous metallic article," United States: DOW CHEMICAL CO, 1966.

[49] C. San Marchi, J. F. Despois, and A. Mortensen, "Uniaxial deformation of open-cell aluminum foam: the role of internal damage," *Acta Materialia,* vol. 52, pp. 2895-2902, Jun 7 2004.

[50] A. Curodeau, E. Sachs, and S. Caldarise, "Design and fabrication of cast orthopedic implants with freeform surface textures from 3-D printed ceramic shell," *Journal of Biomedical Materials Research,* vol. 53, pp. 525-535, Oct 2000.

[51] M. C. Melican, M. C. Zimmerman, M. S. Dhillon, A. R. Ponnambalam, A. Curodeau, and J. R. Parsons, "Three-dimensional printing and porous metallic surfaces: A new orthopedic application," *Journal of Biomedical Materials Research,* vol. 55, pp. 194-202, May 2001.

[52] M. A. Lopez-Heredia, J. Sohier, C. Gaillard, S. Quillard, M. Dorget, and P. Layrolle, "Rapid prototyped porous titanium coated with calcium phosphate as a scaffold for bone tissue engineering," *Biomaterials,* vol. 29, pp. 2608-2615, Jun 2008.

[53] Y. Marutani and T. Kamitani, "Manufacturing sacrificial patterns for casting by salt powder lamination," *Rapid Prototyping Journal,* vol. 10, pp. 281-287, 2004.

[54] M. A. Lopez-Heredia, E. Goyenvalle, E. Aguado, C. Leroux, M. Dorget, and P. Layrolle, "Bone growth in porous titanium implants made by rapid prototyping," *Bioceramics 18, Pts 1 and 2,* vol. 309-311, pp. 1099-1102, 2006.

[55] G. E. Ryan, A. S. Pandit, and D. P. Apatsidis, "Porous titanium scaffolds fabricated using a rapid prototyping and powder metallurgy technique," *Biomaterials,* vol. 29, pp. 3625-3635, Sep 2008.

[56] M. Wehmoller, P. H. Warnke, C. Zilian, and H. Eufinger, "Implant design and production - a new approach by selective laser melting," *CARS 2005: Computer Assisted Radiology and Surgery,* vol. 1281, pp. 690-695

1450, 2005.

[57] P. Heinl, A. Rottmair, C. Korner, and R. F. Singer, "Cellular titanium by selective electron beam melting," *Advanced Engineering Materials,* vol. 9, pp. 360-364, May 2007.

[58] H. Meier and C. Haberland, "Experimental studies on selective laser melting of metallic parts," *Materialwissenschaft Und Werkstofftechnik,* vol. 39, pp. 665-670, Sep 2008.

[59] G. Ryan, A. Pandit, and D. P. Apatsidis, "Fabrication methods of porous metals for use in orthopaedic applications," *Biomaterials,* vol. 27, pp. 2651-2670, May 2006.

[60] N. Kumar, M. R. Judith, A. Kumar, V. Mishra, and M. C. Robert, "Analysis of stress distribution in lumbar interbody fusion," *Spine,* vol. 30, pp. 1731-5, Aug 1 2005.

[61] M. P. Staiger, A. M. Pietak, J. Huadmai, and G. Dias, "Magnesium and its alloys as orthopedic biomaterials: A review," *Biomaterials,* vol. 27, pp. 1728-1734, 2006.

[62] M. F. Culpin, "The Viscosity of Liquid Magnesium and Liquid Calcium," *Proceedings of the Physical Society of London Section B,* vol. 70, pp. 1079-1086, 1957.

[63] M. M. Avedesian and H. Baker, *Magnesium and magnesium alloys*. Materials Park, Ohio: ASM International, 1999.

[64] F. Witte, H. Ulrich, M. Rudert, and E. Willbold, "Biodegradable magnesium scaffolds: Part I: Appropriate inflammatory response," *Journal of Biomedical Materials Research Part A,* vol. 81A, pp. 748-756, Jun 1 2007.

[65] F. Witte, H. Ulrich, C. Palm, and E. Willbold, "Biodegradable magnesium scaffolds: Part II: Peri-implant bone remodeling," *Journal of Biomedical Materials Research Part A,* vol. 81A, pp. 757-765, Jun 1 2007.

[66] A. H. Brothers and D. C. Dunand, "Mechanical properties of a density-graded replicated aluminum foam," *Materials Science and Engineering a-Structural Materials Properties Microstructure and Processing,* vol. 489, pp. 439-443, Aug 20 2008.

[67] V. G. Sonnen, "Hair and scalp treatment with a principally sodium chloride thick viscous aqueous slurry ", U. S. P. O, Ed. United States, 1971, p. 4.

[68] M.Kosek, "Jewelry, Suggested Investment & Burnout Procedures InVision HR 3-D printer - VisiJet HR-M100 patterns," 2004.

[69] R. F. Speyer, *Thermal analysis of materials*. New York: Dekker, 1994.

[70] T. Instruments, "Thermogravimetric Analysis - Q600", 2007.

[71] M. Pourpaix, *Atlas of electrochemical equilibria in aqueous solutions*, 2nd English ed. ed. Houston: National Association of Corrosion Engineers, 1974.

[72] S. Das, "Physical aspects of process control in selective laser sintering of metals," *Advanced Engineering Materials,* vol. 5, pp. 701-711, Oct 2003.

[73] M. F. Ashby, A. Evans, N. A. Fleck, L. J. Gibson, J. W. Hutchinson, and H. N. G. Wadley, "Metal Foams: A Design Guide," Woburn, MA: Butterworth Heinemann, 2000.

[74] A. L. Darling and W. Sun, "Free-form fabrication and micro-CT Characterization of poly-epsilon-caprolactone tissue scaffolds," *Ieee Engineering in Medicine and Biology Magazine,* vol. 24, pp. 78-83, Jan-Feb 2005.

[75] H.-P. Degischer and B. Kriszt, *Handbook of cellular metals : production, processing, applications*: Weinheim ; [Chichester?]bWiley-VCH, 2002.

[76] W. Zhou and Z. L. Wang, *Scanning microscopy for nanotechnology : techniques and applications*. New York ; London: Springer, 2007.

[77] V. Randle, *The measurement of grain boundary geometry*: Institute of Physics, 1993.

[78] F. J. Humphreys, "Review - Grain and subgrain characterisation by electron backscatter diffraction," *Journal of Materials Science,* vol. 36, pp. 3833-3854, Aug 2001.

[79] A. F. Gourgues-Lorenzon, "Application of electron backscatter diffraction to the study of phase transformations," *International Materials Reviews,* vol. 52, pp. 65-128, Mar 2007.

[80] D. J. Dingley and V. Randle, "Microtexture Determination by Electron Back-Scatter Diffraction," *Journal of Materials Science,* vol. 27, pp. 4545-4566, Sep 1 1992.

[81] D. Dingley, "Progressive steps in the development of electron backscatter diffraction and orientation imaging microscopy," *Journal of Microscopy-Oxford,* vol. 213, pp. 214-224, Mar 2004.

[82] S. A. Long and T. D. Mcgee, "Effect of Grain Boundaries on Plastic Deformation of Sodium Chloride," *Journal of the American Ceramic Society,* vol. 46, pp. 583-587, 1963.

[83] W. D. Kingery and M. Berg, "Study of the Initial Stages of Sintering Solids by Viscous Flow, Evaporation-Condensation, and Self-Diffusion," *Journal of Applied Physics,* vol. 26, pp. 1205-1212, 1955.

[84] D. K. Dysthe, Y. Podladchikov, F. Renard, J. Feder, and B. Jamtveit, "Universal scaling in transient creep," *Physical Review Letters,* vol. 89, pp. -, Dec 9 2002.

[85] Z. Karcz, E. Aharonov, D. Ertas, R. Polizzotti, and C. H. Scholz, "Deformation by dissolution and plastic flow of a single crystal sodium chloride indenter: An experimental study under the confocal microscope," *Journal of Geophysical Research-Solid Earth,* vol. 113, pp. -, Apr 11 2008.

[86] D. K. Dysthe, F. Renard, J. Feder, B. Jamtveit, P. Meakin, and T. Jossang, "High-resolution measurements of pressure solution creep," *Physical Review E,* vol. 68, pp. -, Jul 2003.

[87] C. S. Morgan, L. L. Hall, and C. S. Yust, "Sintering of Sodium Chloride," *Journal of the American Ceramic Society,* vol. 46, pp. 559-560, 1963.

[88] G. M. Pennock, M. R. Drury, C. J. Peach, and C. J. Spiers, "The influence of water on deformation microstructures and textures in synthetic NaCl measured using EBSD," *Journal of Structural Geology,* vol. 28, pp. 588-601, 2006.

[89] P. W. Trimby, M. R. Drury, and C. J. Spiers, "Recognising the crystallographic signature of recrystallisation processes in deformed rocks: a study of experimentally deformed rocksalt," *Journal of Structural Geology,* vol. 22, pp. 1609-1620, Nov-Dec 2000.

[90] G. M. Pennock, M. R. Drury, and C. J. Spiers, "Grain boundary populations in wet and dry NaCl," *Materials Science and Technology,* vol. 22, pp. 1307-1315, Nov 2006.

[91] G. M. Pennock, M. R. Drury, and C. J. Spiers, "The development of subgrain misorientations with strain in dry synthetic NaCl measured using EBSD," *Journal of Structural Geology,* vol. 27, pp. 2159-2170, 2005.

[92] J. L. Urai, C. J. Spiers, C. J. Peach, R. C. M. W. Franssen, and J. L. Liezenberg, "Deformation Mechanisms Operating in Naturally Deformed Halite Rocks as Deduced from Microstructural Investigations," *Geologie En Mijnbouw,* vol. 66, pp. 165-176, 1987.

[93] R. Goodall, J. F. Despois, A. Marmottant, L. Salvo, and A. Mortensen, "The effect of preform processing on replicated aluminium foam structure and mechanical properties," *Scripta Materialia,* vol. 54, pp. 2069-2073, Jun 2006.

[94] F. B. Swinkels and M. F. Ashby, "Second report on sintering diagrams," United States PB-82-170739, 1980.

[95] R. J. Thompson and Z. A. Munir, "Influence of Particle-Size on the Sintering Kinetics of Ultrapure Sodium-Chloride," *Journal of the American Ceramic Society,* vol. 65, pp. 312-316, 1982.

[96] R. Goodall, J. F. Despois, and A. Mortensen, "Sintering of NaCl powder: Mechanisms and first stage kinetics," *Journal of the European Ceramic Society,* vol. 26, pp. 3487-3497, 2006.

[97] P. K. Weyl, "Pressure Solution and the Force of Crystallization - a Phenomenological Theory," *Journal of Geophysical Research,* vol. 64, pp. 2001-2025, 1959.

[98] Z. Karcz, E. Aharonov, D. Ertas, R. Polizzotti, and C. H. Scholz, "Stability of a sodium chloride indenter contact undergoing pressure solution," *Geology,* vol. 34, pp. 61-63, Jan 2006.

[99] M. W. Barsoum, *Fundamentals of ceramics*. Bristol: McIOP, 2003.

[100] J. Burgess, *Metal ions in solution*. Chichester: Ellis Horwood ; New York ; London : [Distributed by] Wiley, 1978.

[101] S. Gogolewski, "Bioresorbable polymers in trauma and bone surgery," *Injury,* vol. 31, pp. D28-D32, 2000.

[102] B. Kasemo and J. Gold, "Implant surfaces and interface processes," *Adv Dent Res,* vol. 13, pp. 8-20, June 1, 1999 1999.

[103] P. Pebe, R. Bardot, J. Trinidad, A. Pesquara, J. Lucente, R. Nishimura, and H. Nasr, "Countertorque testing and histomorphometric analysis of various implant surfaces in canines: a pilot study," *Implant Dentistry,* vol. 6, pp. 256-265, 1997.

[104] Z. Schwartz, C. H. Lohmann, J. Oefinger, L. F. Bonewald, D. D. Dean, and B. D. Boyan, "Implant surface characteristics modulate differentiation behavior of cells in the osteoblastic lineage," *Adv Dent Res,* vol. 13, pp. 38-48, June 1, 1999 1999.

[105] C. E. Wilson, J. D. De Bruijn, C. A. Van Blitterswijk, A. J. Verbout, and W. J. A. Dhert, "Design and fabrication of standardized hydroxyapatite scaffolds with a defined macro-architecture by rapid prototyping for bone-tissue-engineering research," *Journal of Biomedical Materials Research - Part A,* vol. 68, pp. 123-132, 2004.

[106] C. E. Wen, Y. Yamada, K. Shimojima, Y. Chino, H. Hosokawa, and M. Mabuchi, "Compressibiltity of porous magnesium foam: dependency on porosity and pore size," *Materials Letters,* vol. 58, pp. 357-60, 2004.

[107] K. A. Gross and L. M. Rodriguez-Lorenzo, "Biodegradable composite scaffolds with an interconnected spherical network for bone tissue engineering," *Biomaterials,* vol. 25, pp. 4955-4962, Sep 2004.

[108] P. Hariraksapitak, O. Suwantong, P. Pavasant, and P. Supaphol, "Effectual drug-releasing porous scaffolds from 1,6-diisocyanatohexane-extended poly(1,4-butylene succinate) for bone tissue regeneration," *Polymer,* vol. 49, pp. 2678-2685, May 27 2008.

9. Appendix

9.1. InVision modeller data sheet

3D SYSTEMS

INVISION HR 3-D Modeler

Fast, cost-effective manufacturing of precision micro-casting patterns for small metal components for jewelry, electronics and other applications.

www.3dsystems.com

From CAD to InVision® HR printer pattern to production casting tree.

APPLICATIONS

- Production quality patterns for direct casting of jewelry and other small components
- Models for design communication, presentation, marketing or pre-selling
  - Jewelry
  - Electronic components
  - Consumer Products
  - Medical instruments/devices

InVision® HR 3-D Modeler

FEATURES

- Fast, multi-jet build process
  - Exceptional fine feature detail and surface finish
  - Blue pattern material
  - "Melt away" supports
  - "Plug and play" operation
  - Network-ready
  - Intelligent job queuing

BENEFITS

- Quickly and automatically produce precision patterns and models from 3-D CAD data
- Outstanding repeatability for short-run pattern production
- Compatible with direct investment casting
- Labor-free post processing
- No special training required
- Reduce product development time and costs

3D SYSTEMS CORPORATION

TRANSFORM YOUR PRODUCTS

INVISION® HR 3-D Modeler

TECHNICAL DATA

Technology

Product	[illegible] HR 3-D Modeler system (InVision® HR 3-D Modeler, [illegible] material cartridges)
Modeler	[illegible] HR 3-D Modeler
Model Build	Model material: [illegible] HR 900 Support material: [illegible] S100
Software	[illegible] part client software
Accessories (not included)	[illegible] Refills

Modeler

Technology	[illegible] Modeling (ink-jet thermal material application, [illegible] curing)
Maximum Build Volume	[illegible] x 127 x 152 mm ([illegible] x 5 x 6 in)
Maximum Single Part Size	64.5 cm³ (3.9 in³)
Resolution	600 x 540 x 900 DPI (z-y-x)
Certifications	[illegible] marked, CE certified
Electrical	100-127 VAC, 50/60 Hz, single-phase; 150 W; 200-240 VAC, 50/60 Hz, single-phase; 150 W; Power system specifications compliant (world countries)
Operating Temperature Range	15-28 °C (64-82 °F)
Noise	<60 dBA measured at medium fan setting
Printer Dimensions (W x H x D)	241 kg (531 lb); 1056 x [illegible] x 762 mm (38 x 66 x 66 in)
Printer Dimensions (W x H x D)	294 kg (653 lb); 877 x [illegible] x 965 mm (35 x 45 x 38 in)

Interface

Network connectivity	Network ready with 10/100 Ethernet interface
Client hardware recommendations	2.0 GHz Pentium IV with 1 GB RAM or higher. Graphics support and minimum 32 MB video RAM or higher
Client Software OS Support	Windows XP Professional/2000/NT 4.0/Me/98
Input Data File Format	STL

Materials

	Model	Support
Material	[illegible] 900	[illegible] S100
Composition	Acrylic plastic	Wax
Color	Blue	White
Case Quantity	4 cartridges	5 cartridges
Net Weight (approximate)	1.00 kg (2.2 lb)	0.85 kg (1.9 lb)
Density (ASTM D792)	1.14 g/cm³	N/A
Tensile Modulus (ASTM D638)	2,200 MPa (320,000 psi)	N/A
Tensile Strength (ASTM D638)	37 MPa (5,400 psi)	N/A
Tensile Elongation at Break (ASTM D638)	10.0%	N/A
Flexural Modulus (ASTM D790)	2,000 MPa (290,000 psi)	N/A
Flexural Strength (ASTM D790)	61 MPa (9,000 psi)	N/A

[illegible] product release for [illegible] conditions. [illegible] are available by [illegible].

[illegible] material [illegible] ASTM [illegible] available [illegible].

For more information about 3D Systems' products on the web at:
www.3dsystems.com
or e-mail us at
moreinfo@3dsystems.com

3D SYSTEMS
TRANSFORM YOUR PRODUCTS

9.2. Drawings

Infiltration device

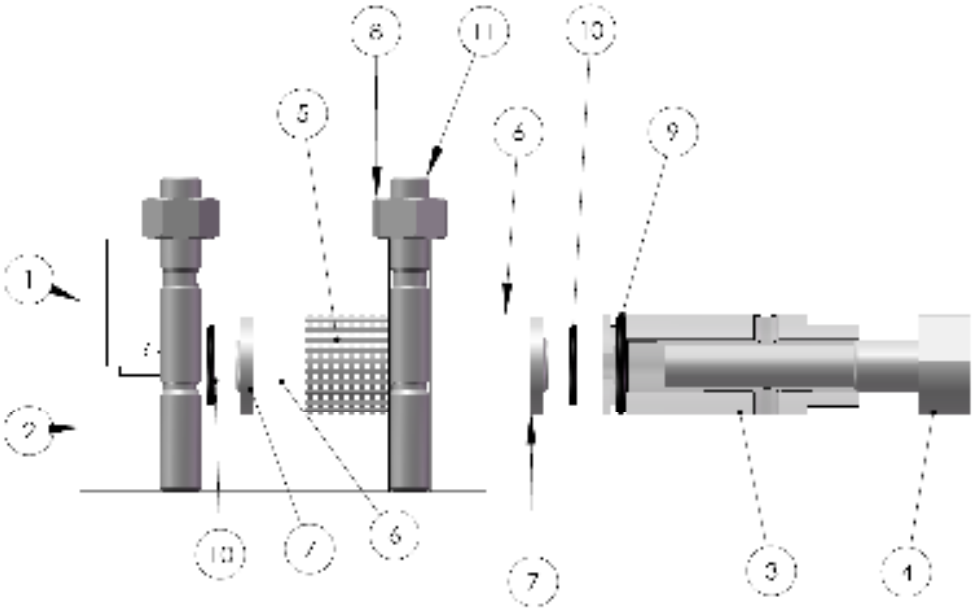

ITEM NO.	PART NUMBER	DESCRIPTION	QTY.
1	Holder with air passage		1
2	Holder		1
3	Piston		1
4	Piston nipple		1
5	Cyl 20x20x1_0		1
6	Filter	ø19.5 mm No 40 filter paper	2
7	Filter mesh	MILLEX 0.22 µm inline filter unit	2
8	Hexagon Nut ISO - 4034 - M8 - N	Stailess steel nut	4
9	J515220x0153H	O ring	1
10	J515178x0124H	O ring	2
11	DIN 938 - M8 x 40 --- 22N	Stainless steel stud	4

UNLESS OTHERWISE SPECIFIED:
DIMENSIONS ARE IN MILLIMETERS

TOLERANCES:
LINEAR: +/- 0.1
ANGULAR: +/-0.5°

DEBUR AND BREAK SHARP EDGES

DO NOT SCALE DRAWING | REVISION

UNIVERSITY OF CANTERBURY
MECHANICAL ENGINEERING DEPARTMENT

	NAME	SIGNATURE	DATE
DRAWN	INGOLFUR		20.10.07
CHK'D	INGOLFUR		20.10.07
APPV'D			
MFG			
Q.A			

MATERIAL:

WEIGHT:

Assembly

PROJECT - INFILTRATION DEVICE

DWG NO. 001

A4

SCALE:1:1 | SHEET 1 OF 6

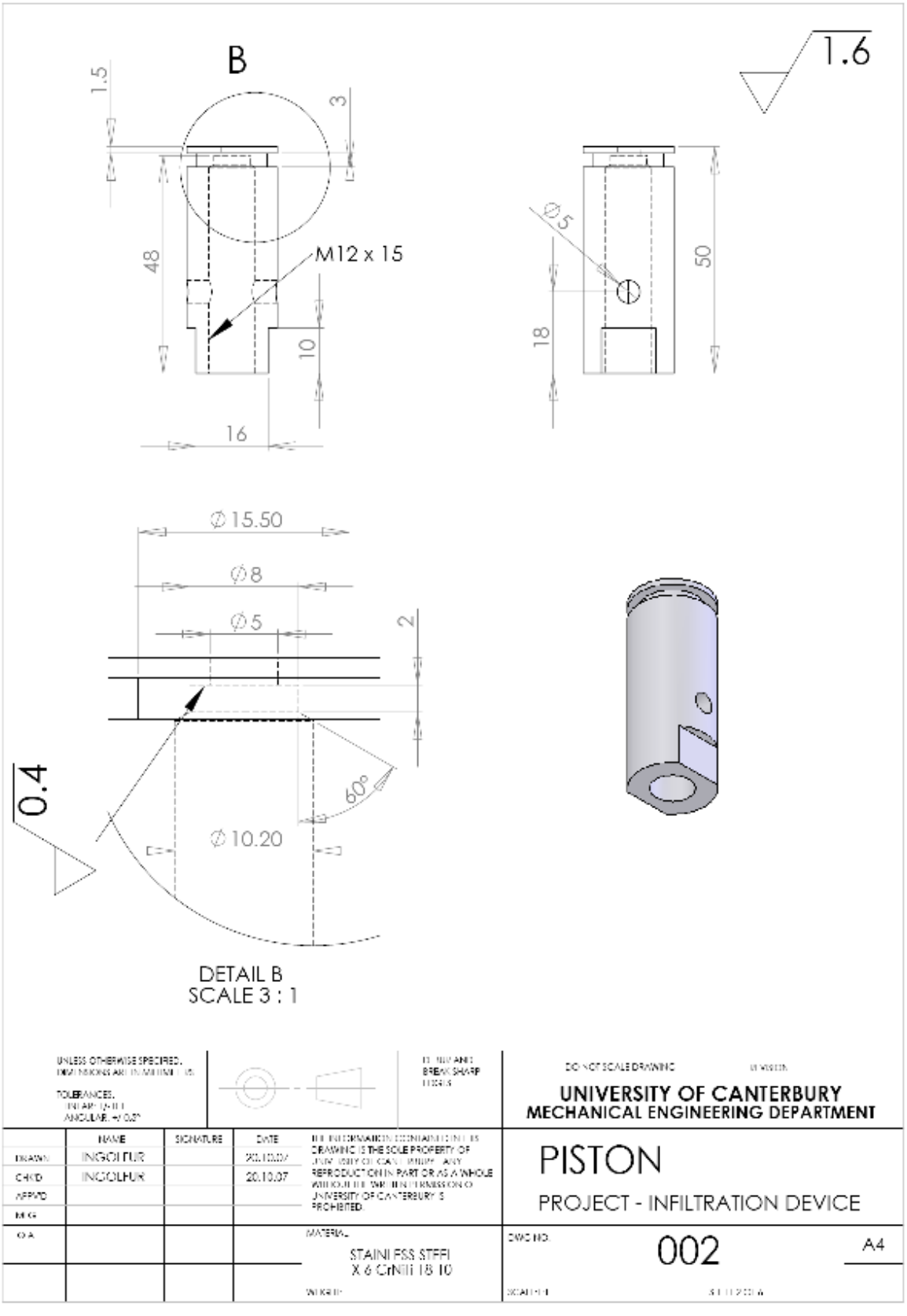
B
1.6
1.5
3
48
M12 x 15
10
16
Ø5
18
50
Ø15.50
Ø8
Ø5
2
0.4
60°
Ø10.20
DETAIL B
SCALE 3 : 1
UNLESS OTHERWISE SPECIFIED,
TOLERANCES,
ANGULAR: +/- 0.5°
BREAK SHARP
EDGES
DO NOT SCALE DRAWING
UNIVERSITY OF CANTERBURY
MECHANICAL ENGINEERING DEPARTMENT
NAME
SIGNATURE
DATE
DRAWN
INGOLFUR
20.10.07
CHKD
INGOLFUR
20.10.07
APPVD
MFG
Q.A
DRAWING IS THE SOLE PROPERTY OF
REPRODUCTION IN PART OR AS A WHOLE
WITHOUT THE WRITTEN PERMISSION OF
UNIVERSITY OF CANTERBURY IS
PROHIBITED.
PISTON
PROJECT - INFILTRATION DEVICE
MATERIAL:
STAINLESS STEEL
X 6 CrNiTi 18 10
DWG NO.
002
A4
WEIGHT:
SCALE: 1:1
SHEET 1 OF 1

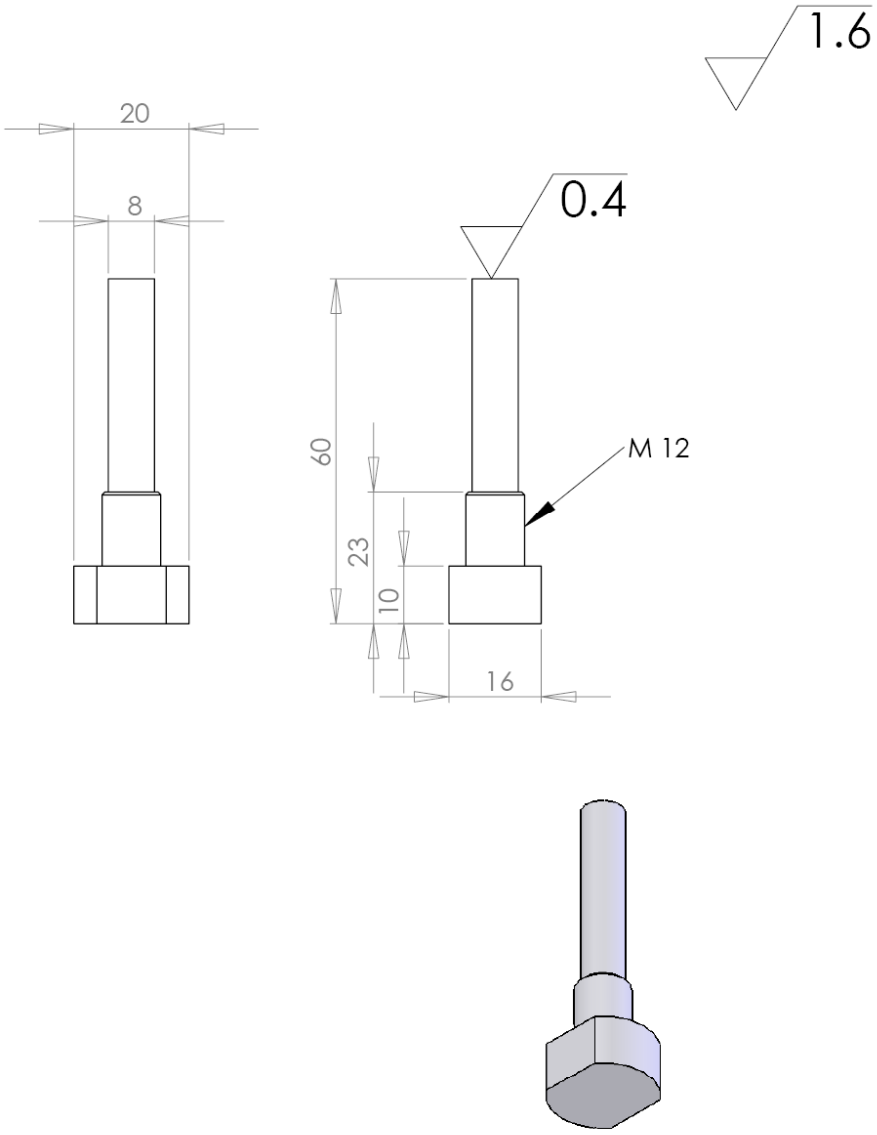

UNLESS OTHERWISE SPECIFIED: DIMENSIONS ARE IN MILLIMETERS TOLERANCES: LINEAR: +/- 0.1 ANGULAR: +/-0.5°				DEBUR AND BREAK SHARP EDGES	DO NOT SCALE DRAWING / REVISION
					UNIVERSITY OF CANTERBURY **MECHANICAL ENGINEERING DEPARTMENT**
	NAME	SIGNATURE	DATE	THE INFORMATION CONTAINED IN THIS DRAWING IS THE SOLE PROPERTY OF UNIVERSITY OF CANTERBURY. ANY REPRODUCTION IN PART OR AS A WHOLE WITHOUT THE WRITTEN PERMISSION OF UNIVERSITY OF CANTERBURY IS PROHIBITED.	# Valve Niple PROJECT - INFILTRATION DEVICE
DRAWN	INGOLFUR		20.10.07		
CHK'D	INGOLFUR		20.10.07		
APPV'D					
MFG					
Q.A				MATERIAL: STAINLESS STEEL X 6 CrNiTi 18 10	DWG NO. 003 / A4
				WEIGHT:	SCALE:1:1 / SHEET 3 OF 6

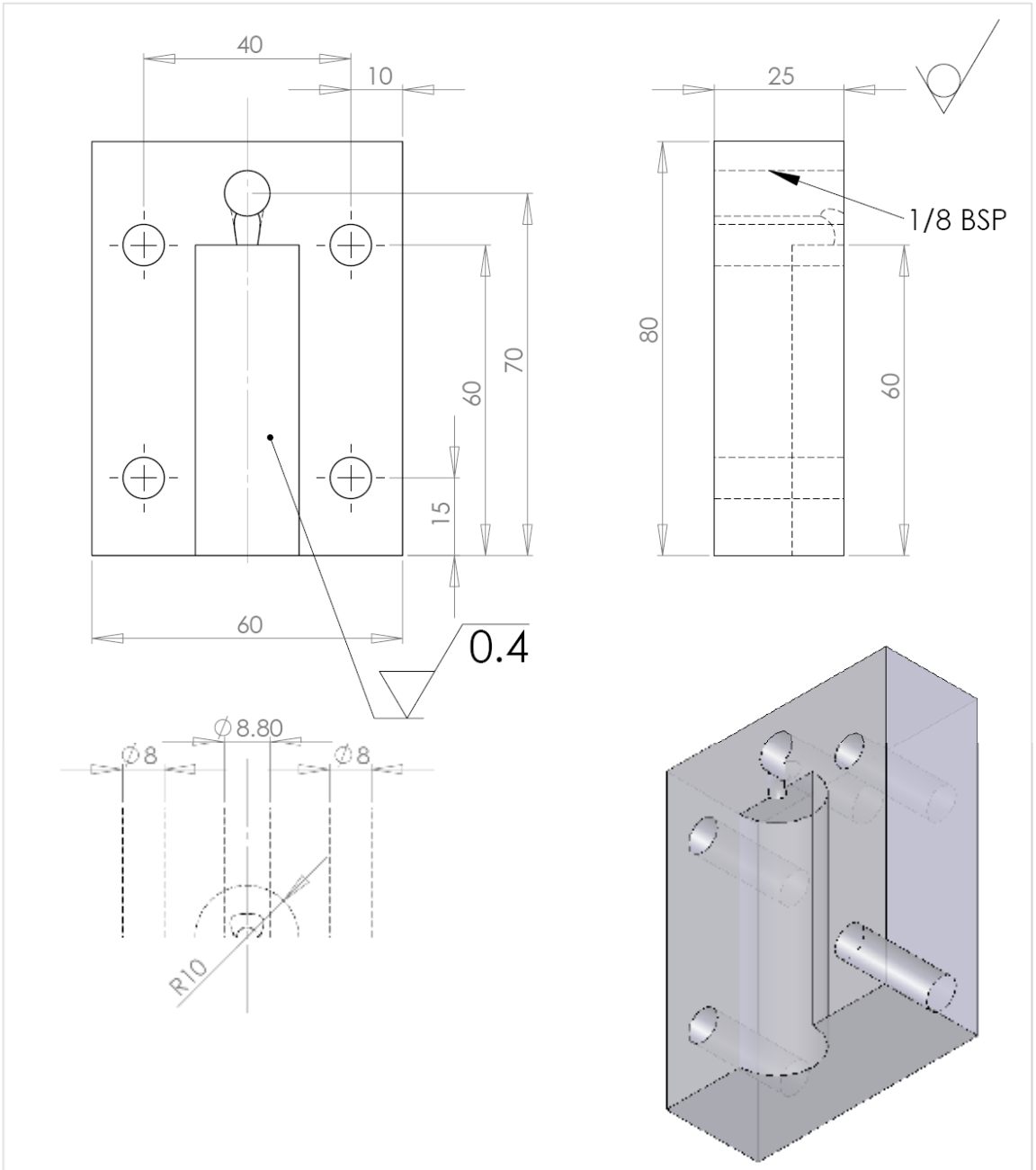

DEBUR AND BREAK SHARP EDGES

	NAME	SIGNATURE	DATE
DRAWN	INGOLFUR		20.10.07
CHKD	INGOLFUR		20.10.07
APPVD			
MFG			
QA			

THE INFORMATION CONTAINED IN THIS DRAWING IS THE SOLE PROPERTY OF THE UNIVERSITY OF CANTERBURY. ANY REPRODUCTION IN PART OR AS A WHOLE WITHOUT THE WRITTEN PERMISSION OF THE UNIVERSITY OF CANTERBURY IS PROHIBITED.

MATERIAL

PorsPox

WEIGHT:

UNIVERSITY OF CANTERBURY
MECHANICAL ENGINEERING DEPARTMENT

Mould with tunnel

PROJECT - INFILTRATION DEVICE

DWG NO 004

A4

SCALE: 1:1

SHEET 4 OF 6

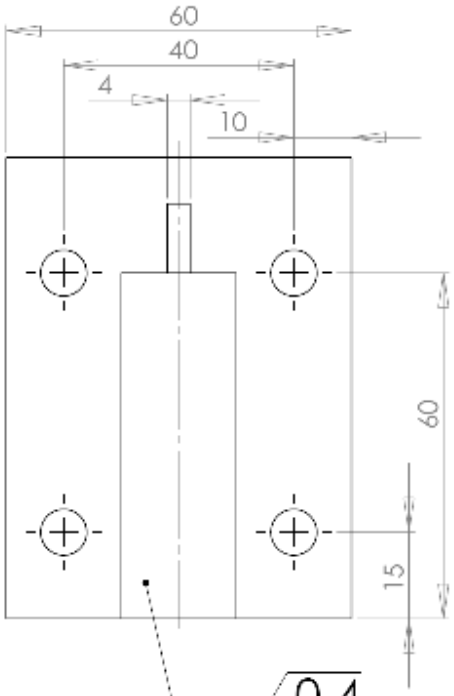

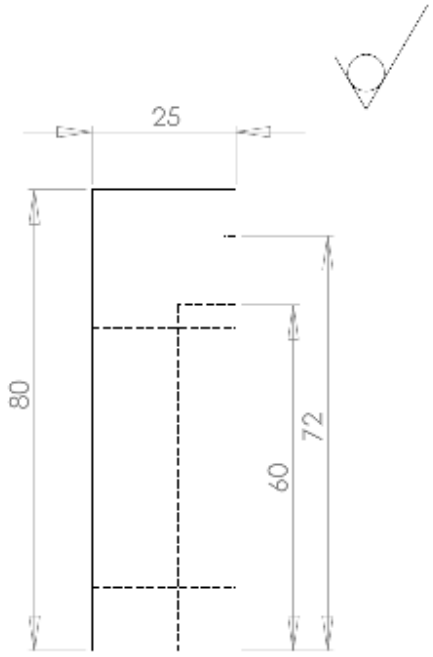

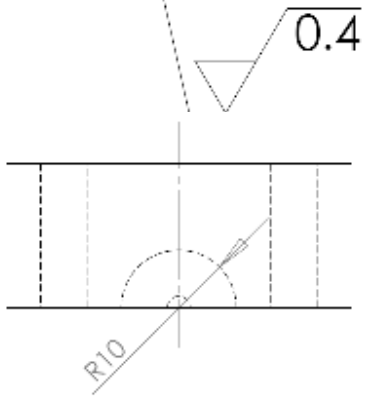

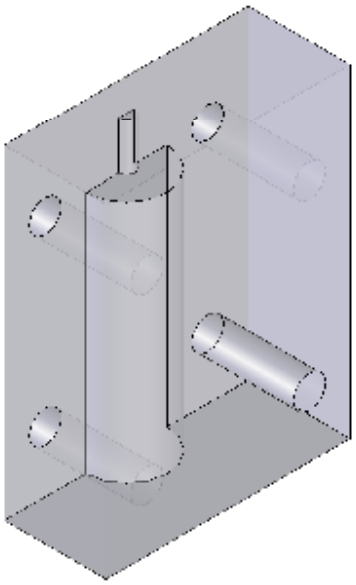

UNLESS OTHERWISE SPECIFIED:
DIMENSIONS ARE IN MILLIMETRES

TOLERANCES:
LINEAR: +/- 0.1
ANGULAR: +/- 0.5°

DO NOT SCALE DRAWING

REVISION

UNIVERSITY OF CANTERBURY
MECHANICAL ENGINEERING DEPARTMENT

	NAME	SIGNATURE	DATE
DRAWN	INGOLFUR		20.10.07
CHK'D	INGOLFUR		20.10.07
APPV'D			
MFG			
Q.A			

Mould

PROJECT - INFILTRATION DEVICE

MATERIAL:
PerspEx

DWG NO.
005

A4

WEIGHT:

SCALE:

SHEET 1 OF 1

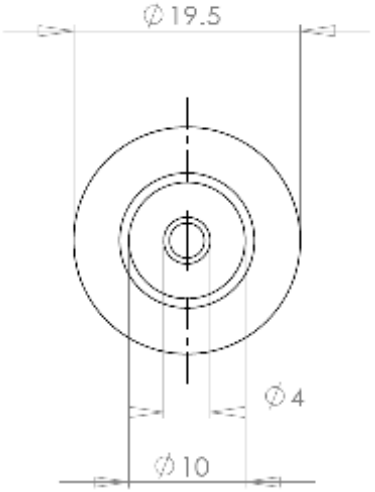

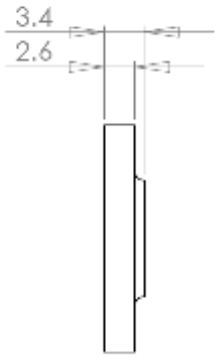

UNLESS OTHERWISE SPECIFIED:
DIMENSIONS ARE IN MILLIMETERS

TOLERANCES:
LINEAR: +/- 0.1
ANGULAR: +/- 0.5°

BREAK AND
BREAK SHARP
EDGES

DO NOT SCALE DRAWING

REVISION

UNIVERSITY OF CANTERBURY
MECHANICAL ENGINEERING DEPARTMENT

	NAME	SIGNATURE	DATE
DRAWN	INGOLFUR		20.10.07
CHKD	INGOLFUR		20.10.07
APPV'D			
MFG			
Q.A			

Filter Mesh

PROJECT - INFILTRATION DEVICE

MATERIAL:
MILLEX 0.22 µm
inline filter unit

DWG NO.
006

A4

WEIGHT:

SCALE:2:1

SHEET 6 OF 6

Press bracket

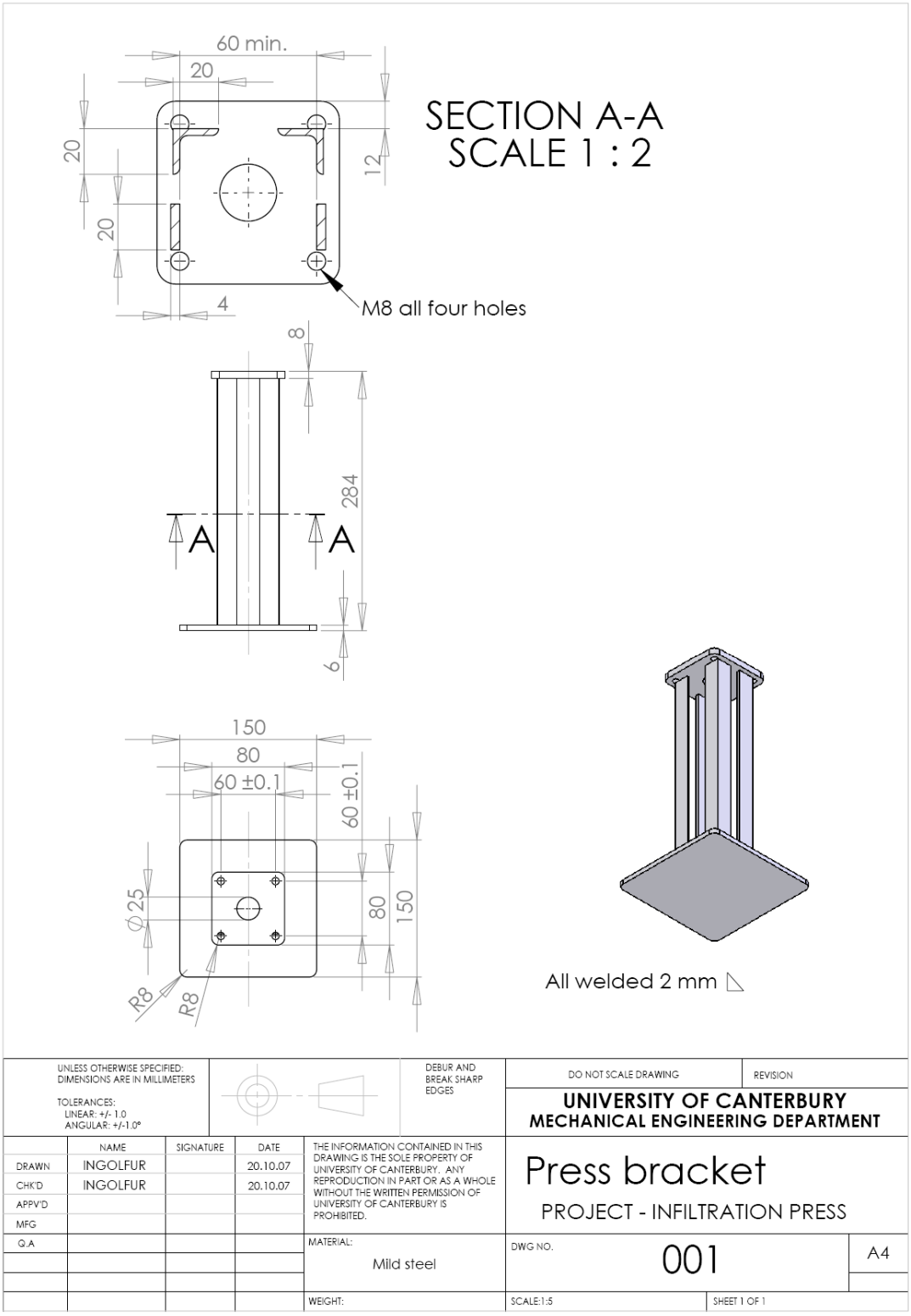

Crucible

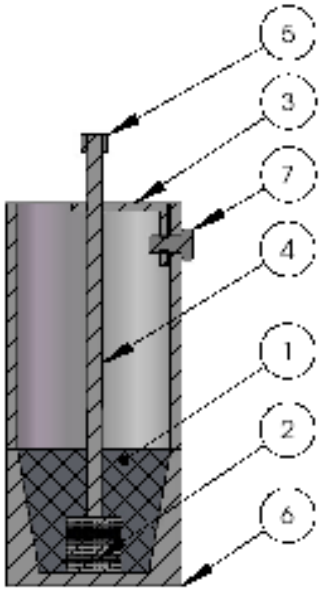

SECTION A-A

ITEM NO.	PART NUMBER	DESCRIPTION	QTY.
1	Magnesium		1
2	Cyl 20x20x1_0		1
3	Stud holder		1
4	M6 stud		1
5	Hexagon Nut ISO - 4034 - M6 - N		1
6	Crucible		1
7	ISO 4018 - M6 x 12-WN		1

UNLESS OTHERWISE SPECIFIED: DIMENSIONS ARE IN MILLIMETERS

DEBUR AND BREAK SHARP EDGES

DO NOT SCALE DRAWING | REVISION

UNIVERSITY OF CANTERBURY
MECHANICAL ENGINEERING DEPARTMENT

	NAME	SIGNATURE	DATE
DRAWN	INGOLFUR		20.10.07
CHK'D	INGOLFUR		20.10.07
APPV'D			
MFG			
Q.A			

MATERIAL:

WEIGHT:

ASSEMBLY

PROJECT - DIE CASTING CRUCIBLE

DWG NO. 001

A4

SCALE:1:2

SHEET 1 OF 4

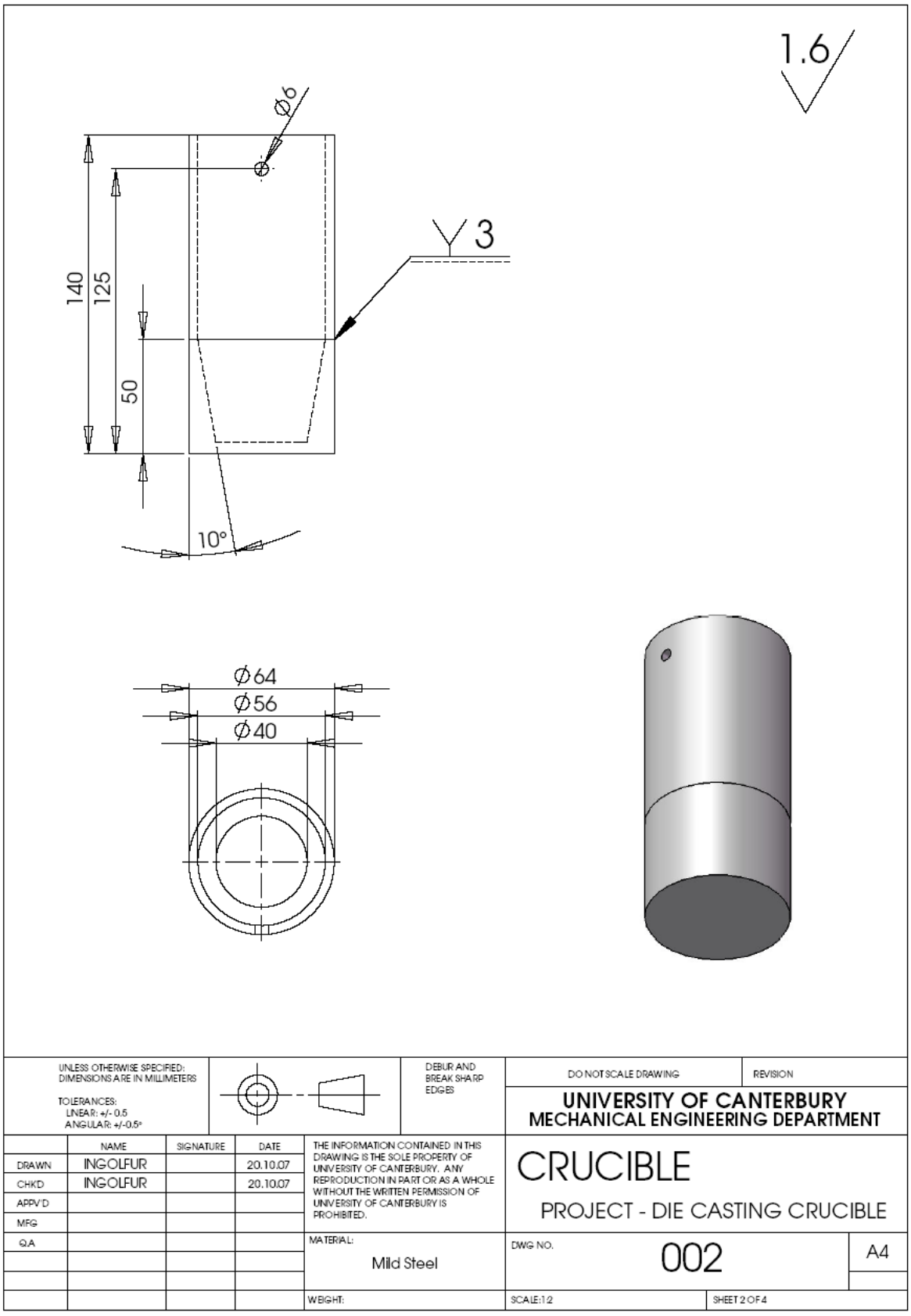

UNLESS OTHERWISE SPECIFIED: DIMENSIONS ARE IN MILLIMETERS TOLERANCES: LINEAR: +/- 0.5 ANGULAR: +/-0.5°		DEBUR AND BREAK SHARP EDGES	DO NOT SCALE DRAWING / REVISION

UNIVERSITY OF CANTERBURY
MECHANICAL ENGINEERING DEPARTMENT

	NAME	SIGNATURE	DATE
DRAWN	INGOLFUR		20.10.07
CHK'D	INGOLFUR		20.10.07
APPV'D			
MFG			
Q.A			

CRUCIBLE

PROJECT - DIE CASTING CRUCIBLE

MATERIAL: Mild Steel

DWG NO. 002

A4

WEIGHT:

SCALE:1:2

SHEET 2 OF 4

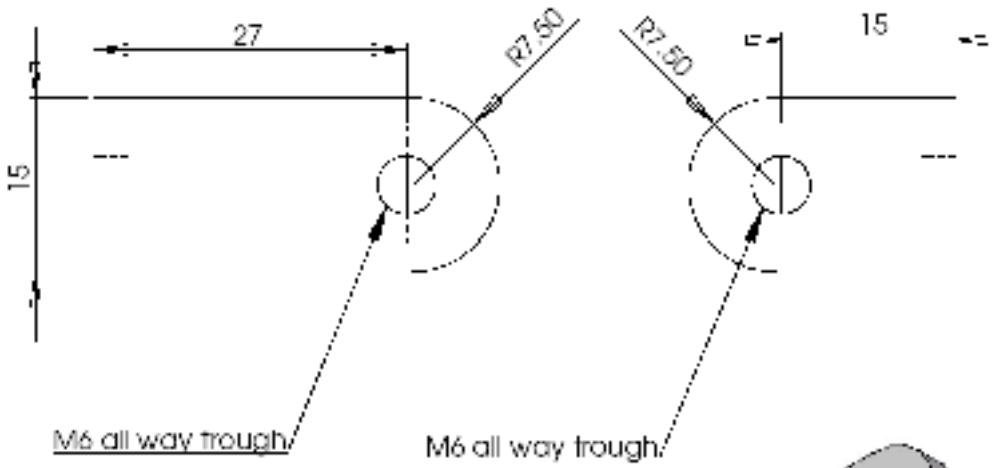

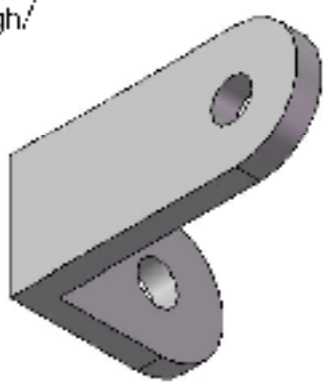

UNIVERSITY OF CANTERBURY
MECHANICAL ENGINEERING DEPARTMENT

	NAME	SIGNATURE	DATE
DRAWN	INGOJUR		28/10/07
CHKD	INGOJUR		28/10/07
APP'D			
MFG			
Q.A			

DRAWING IS THE COPYRIGHT OF THE UNIVERSITY OF CANTERBURY. ANY REPRODUCTION IN PART OR AS A WHOLE WITHOUT THE WRITTEN PERMISSION OF THE UNIVERSITY OF CANTERBURY IS PROHIBITED.

MATERIAL: Mild Steel

ROD HOLDER

PROJECT - DIE CASTING CRUCIBLE

DWG NO. 003

A4

WEIGHT:

SCALE:1:1

SHEET 1 OF 1

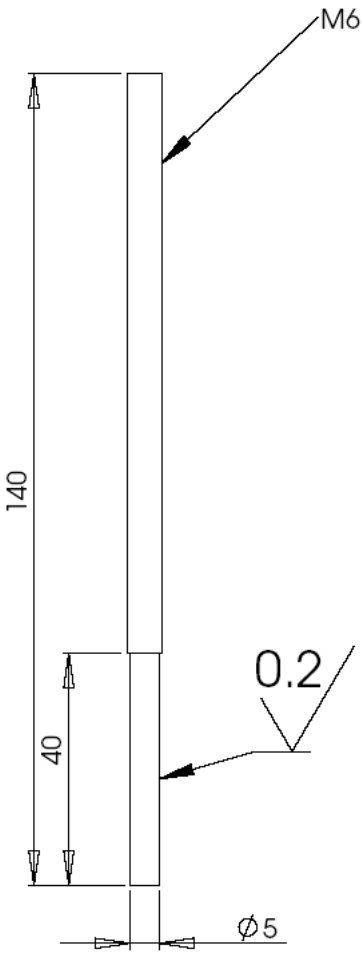

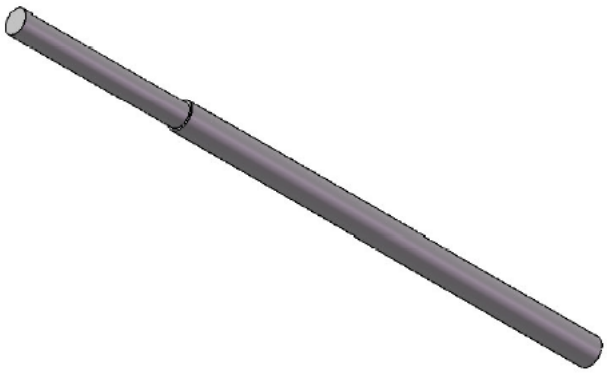

UNLESS OTHERWISE SPECIFIED: DIMENSIONS ARE IN MILLIMETERS TOLERANCES: LINEAR: +/- 0.1 ANGULAR: +/-0.5°		DEBUR AND BREAK SHARP EDGES	DO NOT SCALE DRAWING / REVISION
			UNIVERSITY OF CANTERBURY MECHANICAL ENGINEERING DEPARTMENT

	NAME	SIGNATURE	DATE
DRAWN	INGOLFUR		20.10.07
CHK'D	INGOLFUR		20.10.07
APPV'D			
MFG			
Q.A			

ROD

PROJECT - DIE CASTING CRUCIBLE

MATERIAL: M6 Steel Rod

DWG NO. 004

A4

WEIGHT:

SCALE:5:1

SHEET 4 OF 4